Measuring Quantum Correlations of Polarization, Spatial Mode, and Energy-Time Entangled Photon Pairs.

by

Andrew Cameron

A thesis
presented to the University of Waterloo
in fulfillment of the
thesis requirement for the degree of
Doctor of Philosophy
in
Physics (Quantum Information)

Waterloo, Ontario, Canada, 2023

Examining Committee Membership

The following served on the Examining Committee for this thesis. The decision of the Examining Committee is by majority vote.

External Examiner:	Jennifer Ogilvie Professor, Dept. of Physics and Dept. of Biophysics, University of Michigan
Supervisor(s):	Kevin Resch Professor, Dept. of Physics & Astronomy, University of Waterloo
Internal Member:	Thomas Jennewein Professor, Dept. of Physics & Astronomy, University of Waterloo
Internal-External Member:	Jon Yard Professor, Dept. of Combinatorics and Optimization, University of Waterloo
Other Member(s):	Dmitry Pushin Professor, Dept. of Physics & Astronomy, University of Waterloo

Author's Declaration

I hereby declare that I am the sole author of this thesis. This is a true copy of the thesis, including any required final revisions, as accepted by my examiners.

I understand that my thesis may be made electronically available to the public.

Abstract

Optical quantum technologies have found applications in all facets of quantum information. Single photons are actively being researched for quantum computation, communication, and sensing, due to their robustness against decoherence stemming from their minimal interaction with the environment. For communication and networking applications, specifically, photons are lauded for their speed and coherence over long distances. While clear benefits arise from the lack of photon-environment interaction, measurement and control of all photonic degrees of freedom is made challenging. Each degree of freedom, be it polarization, space, time, or frequency, comes with its own advantages and drawbacks. The potential that single photons bring to future quantum technologies may only be realized by full control over each of these properties of light.

The polarization degree of freedom can be used for high fidelity preparations and measurements and is experimentally controlled with high precision. The spatial degree of freedom, on the other hand, while comparatively trickier to work with, provides access to a large Hilbert space for encoding information that polarization falls short of. Together, these properties of light are combined in structured waves to use the advantages of both degrees of freedom simultaneously. One particularly popular spatial encoding, orbital angular momentum, has received a lot of attention for its high-dimensionality and experimental realizations. However, these states are not preserved by fiber and decohere in turbulence. Correlations between polarization and orbital angular momentum have shown robustness in scattering and turbulent media, demonstrating the advantage of their partnership.

The energy-time degree of freedom of light also provides a large Hilbert space for encoding, along with preservation of quantum information through fiber transmission. The accessible state space is determined by the resolution of controls and measurements in both frequency and time. Specifically, single photon manipulation on ultrafast timescales has become more practical in recent years, enabling measurement on timescales faster than state-of-the-art single photon detectors.

In the first experiments presented in this thesis, novel single-photon structured waves are experimentally demonstrated and imaged with a single photon emICCD camera. First, these states are propagated in free space and used to demonstrate a Talbot effect with single photons. Imaging at different fractional Talbot distances shows the near-field interference patterns of a two-dimensional Talbot carpet. Next, the correlations between the polarization of one photon and the spatial mode of its partner entangled photon are utilized to remotely prepare complex spatial arrays by means of heralded polarization measurements.

The final chapter of this thesis moves focus to the energy-time degree of freedom. The optical Kerr effect, a third order nonlinear optical effect, is used to gate energy-time entan-

gled photons with sub-picosecond resolution, therefore surpassing the timing limitations of single photon detectors. With this fast optical gating technique, the temporal correlations of two energy-time entangled photons are measured. In addition to spectral correlation measurements, these are used to verify energy-time entanglement. This demonstration adds the optical Kerr effect to the short list of available methods in ultrafast quantum optics, further advancing experimental control of the energy-time degree of freedom of single photons.

Acknowledgements

Five and a half years is a lot of time. Throughout graduate school, I have experienced enormous personal growth, and living outside of the Maritimes has given me a much wider perspective which I hope to convince others to push for. The friends and colleagues I've made at my time at the Institute for Quantum Computing and the University of Waterloo as a whole are to credit for my persistence through the challenging and competitive environment of academia. Two years into my studies, COVID-19 transformed the world and took over all conversations, focuses, and worries. In addition to the many names I want to thank below, I thank the tireless efforts of the first responders, front-line workers, vaccine researchers, and science communicators that minimized the far-reaching effects of the pandemic and helped us move on to a social and optimistic world.

First of all, I'd like to thank my supervisor, Kevin Resch. The pandemic was a particularly difficult time to lead a group of people and run an experimental physics lab, yet your unwavering support of our well being, along with all your hard work to get our lab back-up and running, was paramount to our mental health and success. Thank you to my committee members, Thomas Jennewein, Dmitry Pushin, and Jon Yard for your advice, collaboration, and guidance throughout my time in Waterloo, and thank you to Jennifer Ogilvie for committing the time to join my committee as an external examiner.

In our quantum optics and quantum information group, there are three past members that have mentored and taught me so much they must be singled out. Thank you to Jean-Philippe MacLean for introducing me to quantum optics and setting an unbelievably high bar for balancing strong work-ethic with personal life and fitness without losing the passion to learn and discover. Thank you to John Donohue for your experiment troubleshooting, contagious positivity - I can hear your first floor laugh all the way in my third floor office, and puzzled-pints teamwork over the years. Thanks to you I aim to keep science outreach and communication as a core facet of my life. Many thanks to Sacha Schwarz for introducing me to the lab, teaching me how to align optics with Swiss precision, and showing up to work and meetings with military punctuality. I'd also like to thank Matthew Brown, Mike Mazurek, Patrick Daley, and Morgan Mastrovich for helping me fit in to the city and research group when I arrived. It's a steep learning curve from undergrad to grad school and you each helped make the transition seamless and enjoyable.

Many other group members have made the lab a great place to work. Special thanks to Sandra Cheng and Mike Grabowecky for staying positive and working hard as a team throughout the social distancing restrictions and lab equipment supply chain issues. Thank you to group members Chris Pollack, Ruoxuan Xu, Jack Bishop, Ben Wong, Satchel Ar-

mena, Ben MacLellan, Bharat Kuchhal, and Tristan Lismer. Tristan, if you read my thesis a small fraction of the times I read JP and John's theses, I've done my job.

My work at IQC has been particularly collaborative, and you can tell by the author lists on my papers that I'm far from an Isaac Newton do-it-yourself type. I wouldn't have gotten to this point without all of the collaborators along the way. Thank you to Dusan Sarenac, Connor Kapahi, and Katanya Kuntz in the OAM collaboration across from RAC to QNC. Thank you to the NRC collaborators in Ottawa, Kate Fenwick, Duncan England, Philip Bustard, and Ben Sussman for your guidance and expertise. Even though I worked in a small group, it was as if I had an army of senior researchers in a slack channel helping me through the final two years.

Balance is a core tenant of my work-ethic, and I must take the time to thank my Waterloo friends outside of the lab who were there for every happy-hour and Friday night I needed them. Thank you to my first year grad school turned lifelong friends Bryce Hosking, Matt Angus, Matt Slavin, and Andrew Grace for putting up with me, Jon Horrocks, and Bradley Noonan from PEI. Thank you to Keegan Kirk, Ena Ristic, Ramy Tannous, Carl Tutton, Shayan Majidy, Corina Vandongen, Mathieu Yip, Jennifer Gilmour, Rhyse Maryniuk, Peter Wen, Connor Sykora, and Bidushi Dhungana for being my family away from home.

IQC's staff have supported me and gone above and beyond in many ways from room booking and program support, to writing articles about my accomplishments and rooting for me along the way. Thank you to Andrew Dale, Erica Boland, Emma Bartlett, Maren Butcher, Mary Lyn Payerl, Kayleigh Platz, Kimberly Kuntz, Siobhan Stables, and Matt Schumacher for making IQC a wonderful place to work.

Lastly, I want to thank my family for cheering me on from a far. Thank you to my parents, Derrick and Sharon, for their unmatched support and confidence in me. They have always been my biggest fans, and all the phone calls have convinced me that moving away to the mainland for school hasn't changed a thing. Thank you to my brother, Ryan, for giving me the inspiration to always be smiling, joking, and travelling. Finally, thank you to Medea, for your support from both near and far. We have gone through a lot to get to this point and I will forever remember the love and encouragement you have shown me in this chapter, one of many more to come, in our life together.

Dedication

For Medea.

Table of Contents

List of Figures

List of Tables

List of IQC Publications

Andrew R. Cameron, Kate L. Fenwick, Sandra W. L. Cheng, Sacha Schwarz, Benjamin MacLellan, Philip J. Bustard, Duncan England, Benjamin Sussman, and Kevin J. Resch, arXiv:2305.14498 [quant-ph] (2023).

Michael J. Grabowecky, Christopher A. J. Pollack, **Andrew R. Cameron**, Robert W. Spekkens, and Kevin J. Resch, Phys Rev A **105**, 032204 (2022).

Andrew R. Cameron, Sandra W. L. Cheng, Sacha Schwarz, Connor Kapahi, Dusan Sarenac, Michael Grabowecky, David G. Cory, Thomas Jennewein, Dmitry A. Pushin, and Kevin J. Resch, Phys. Rev. A **104**, L051701 (2021).

Sacha Schwarz, Connor Kapahi, Ruoxuan Xu, **Andrew. R. Cameron**, Dusan Sarenac, Jean-Philippe W. MacLean, Katanya B. Kuntz, David G. Cory, Thomas Jennewein, Kevin J. Resch, and Dmitry A. Pushin, Phys. Rev. A **101**, 043815 (2020).

“ When you change the way you look at things, the things you look at change”

Max Planck

“ There is a crack in everything, that’s how the light gets in”

Leonard Cohen

Chapter 1

Quantum optics

1.1 Chapter Overview

There are many strategies for encoding quantum information in the electromagnetic field, and throughout this thesis, experiments that focus on multiple encodings which exploit different degrees of freedom of light will be presented. This chapter sets the stage for understanding the advantages and disadvantages of working with light's varying degrees of freedom by first discussing how we think of light as a quantized field in Sec. 1.2, how we formalize the polarization, spatial mode, and energy-time degrees of freedom in Sec. 1.3, how we can describe correlations between them in Sec. 1.4, and finally how we experimentally determine these correlations in Sec. 1.5.

1.2 Quantizing the Electromagnetic Field

We start, as many quantum optics texts do [6, 7, 8], by considering a simple electromagnetic field that is contained in a one-dimensional cavity of length L along the z-axis. The electric field makes a standing wave in the cavity with nodes at the walls $z = 0$ and $z = L$. Assuming there are no currents, charges, or dielectric materials in the cavity, and setting the polarization of the field to be along the x-direction, $\mathbf{E}(\mathbf{r}, t) = E_x(z, t)\hat{i}$, where $\hat{i}$ is the unit vector aligned with the x-axis, Maxwell's equations reduce to,

$$\nabla \times \mathbf{E} = -\frac{\partial \mathbf{B}}{\partial t} \tag{1.1}$$

$$\nabla \times \mathbf{B} = \mu_0 \epsilon_0 \frac{\partial \mathbf{E}}{\partial t} \tag{1.2}$$

$$\nabla \cdot \mathbf{E} = 0 \tag{1.3}$$

$$\nabla \cdot \mathbf{B} = 0. \tag{1.4}$$

These equations and boundary conditions are satisfied by an electric field of the form

$$E_x(z,t) = \left(\frac{2\omega^2}{V\epsilon_0}\right)^{1/2} q(t)\, \sin(kz) \tag{1.5}$$

where the field's angular frequency ω is related to the wave number k by $\omega = kc$. Angular frequencies that obey the boundary conditions $z = 0$ and $z = L$ are valid, and have the form $\omega_m = c(m\pi/L)$ for $m \in \mathbb{Z}$, $q(t)$ is a time dependent electric field amplitude, and $V = LA$ is the effective volume of the cavity with cross sectional area A. As the electric field is polarized in the x direction, the magnetic field which satisfies Eqs. 1.2 and 1.4 is orthogonal and aligned with the y axis, $\mathbf{B}(\mathbf{r},t) = B_y(z,t)\hat{j}$, where $\hat{j}$ is the unit vector aligned with the y-axis, and has the form

$$B_y(z,t) = \left(\frac{\mu_0\epsilon_0}{k}\right)\left(\frac{2\omega^2}{V\epsilon_0}\right)^{1/2} \dot{q}(t)\, \cos(kz) \tag{1.6}$$

The classical field energy, called the Hamiltonian H, is obtained with an integration over the cavity volume as

$$\begin{aligned} H &= \frac{1}{2}\int dV \left(\epsilon_0 \mathbf{E}^2(\mathbf{r},t) + \frac{1}{\mu_0}\mathbf{B}^2(\mathbf{r},t)\right) \\ &= \frac{1}{2}\int_0^L dz \int dA \left(\epsilon_0 E_x^2(z,t) + \frac{1}{\mu_0} B_y^2(z,t)\right) \\ &= \frac{1}{2}(p^2(t) + \omega^2 q^2(t)) \end{aligned} \tag{1.7}$$

where we have used the notation $\dot{q}(t) = p(t)$. To go from the second to the third line of Eq. 1.7, trig integrals $\int_0^L \sin^2(kz)$ and $\int_0^L \cos^2(kz)$ appear. These are straightforward to

evaluate by noting the boundary conditions limit $k = m\pi/L$ for $m \in \mathbb{Z}$. This Hamiltonian is in the same form as a classical one-dimensional harmonic oscillator, which is the key observation that will help quantize the electromagnetic field. For this analogy, the time dependent field amplitudes play the role of the canonical position, $q(t)$, and momentum, $p(t)$.

Using this Hamiltonian, we turn our attention to solving for the energy eigenvalues. Now that we have noted the similarities of our field amplitudes to the position and momentum of a particle in a harmonic oscillator, we use the Bohr correspondence principle to replace our classical q and p variables with the associated Hermitian operators $\hat{q}$ and $\hat{p}$ with commutator $[\hat{q}, \hat{p}] = i\hbar$. We define non-Hermitian operators $\hat{a} = (\omega\hat{q} + i\hat{p})/\sqrt{2\hbar\omega}$ and $\hat{a}^\dagger = (\omega\hat{q} - i\hat{p})/\sqrt{2\hbar\omega}$ referred to as the annihilation and creation operators, respectively, or collectively as the ladder operators. These operators have the commutation relation $[\hat{a}, \hat{a}^\dagger] = 1$, which can be used to rewrite the Hamiltonian as

$$\hat{H} = \hbar\omega \left(\hat{a}^\dagger \hat{a} + \frac{1}{2} \right). \tag{1.8}$$

We now set up the eigenvalue equation by introducing the energy eigenstate, $|\Psi_n\rangle$, with energy eigenvalue E_n as

$$\hat{H} \left| \Psi_n \right\rangle = E_n \left| \Psi_n \right\rangle. \tag{1.9}$$

Multiplying Eq. 1.9 by $\hat{a}^\dagger$ and rearranging the equation with the ladder operator commutation relation will reveal how the creation operator earned its name.

$$\begin{aligned}
\hbar\omega \left(\hat{a}^\dagger \hat{a}^\dagger \hat{a} + \frac{1}{2} \hat{a}^\dagger \right) \left| \Psi_n \right\rangle &= E_n \hat{a}^\dagger \left| \Psi_n \right\rangle \\
\hbar\omega \left[(\hat{a}^\dagger \hat{a} \hat{a}^\dagger - \hat{a}^\dagger) + \frac{1}{2} \hat{a}^\dagger \right] \left| \Psi_n \right\rangle &= E_n \hat{a}^\dagger \left| \Psi_n \right\rangle \\
\hbar\omega \left(\hat{a}^\dagger \hat{a} + \frac{1}{2} \right) \left(\hat{a}^\dagger \left| \Psi_n \right\rangle \right) &= (E_n + \hbar\omega)(\hat{a}^\dagger \left| \Psi_n \right\rangle)
\end{aligned} \tag{1.10}$$

We now see an eigenvalue equation with a new eigenstate, $\hat{a}^\dagger \left| \Psi_n \right\rangle$, and a new energy eigenvalue, $E_n + \hbar\omega$. The common language from which the creation operator adopted its name says that the action of $\hat{a}^\dagger$ created a quanta of energy $\hbar\omega$. This created energy is termed the photon when referring to the electromagnetic field. Similarly, the same

steps with the annihilation operator yields a new eigenstate $\hat{a}\,|\Psi_n\rangle$ with energy eigenvalue $E_n - \hbar\omega$, from which we say the operator annihilated a photon.

These operators create an energy spectrum with integer multiples of $\hbar\omega$ separating the rungs of the ladder. The bottom of this ladder is referred to as the ground state, $|0\rangle$, with energy $\frac{1}{2}\hbar\omega$, and any further use of the annihilation operator results in $\hat{a}\,|0\rangle = 0$. Throughout this thesis, a photon will be denoted as $\hat{a}^\dagger\,|0\rangle$ and experimentally it will be measured by a count in a single photon detector. Photons will be casually discussed a lot in this thesis but to be more verbose and formal, coming back to this chapter can remind you that a photon is the canonically quantized energy of the electromagnetic field which is a solution to Maxwell's equations.

Working back to the electric field of the cavity, we define the canonically quantized electric field operator for a single mode, k, in terms of the ladder operators and for arbitrary polarization direction, $\hat{\epsilon}_k$, as

$$\hat{\mathbf{E}}_k = i\sqrt{\frac{\hbar\omega_k}{2\epsilon_0 V}}\left(\hat{a}_k e^{-i\omega_k t + i\mathbf{k}\cdot\mathbf{r}} - \hat{a}_k^\dagger e^{i\omega_k t - i\mathbf{k}\cdot\mathbf{r}}\right)\hat{\epsilon}_k, \tag{1.11}$$

where the operator has a time dependence and is written in the Heisenberg framework of quantum mechanics. In this framework, states are time independent and time evolution is completely captured within the operator. To model a superposition of multiple modes occurring simultaneously within the cavity, we get the total electric field by adding up the different modes coherently with a discrete sum as

$$\hat{E}(\mathbf{r},t) = \sum_{k_x,k_y,k_z}\hat{\mathbf{E}}_k(\mathbf{r},t) = i\sum_{\mathbf{k}}\sqrt{\frac{\hbar\omega_k}{2\epsilon_0 V}}\left(\hat{a}_{\mathbf{k}} e^{-i\omega_k t + i\mathbf{k}\cdot\mathbf{r}} - \hat{a}_{\mathbf{k}}^\dagger e^{i\omega_k t - i\mathbf{k}\cdot\mathbf{r}}\right)\hat{\epsilon}_k, \tag{1.12}$$

where $\mathbf{r} = (x, y, z)$ is a vector of spatial positions, and $\mathbf{k} = (k_x, k_y, k_z)$ is a vector of wave numbers in different directions. Note, quantization in k_x, k_y, and k_z requires generalizing the 1D cavity to a 3D cubic cavity with length L and volume V [7]. Other than the canonical quantization that occurred by introducing ladder operators, the derivation is done purely with classical electrodynamics. Due to this closeness of the quantum and classical descriptions of light, there are many phenomena that occur in a laboratory with single photons that would also occur with classical light.

Many students have asked what the size of a photon is. Unfortunately, the answer is not well defined in general. In our derivation, we assumed the electromagnetic field was

contained to standing waves in a cavity. That gave us helpful artificial boundary conditions and answers the question of size because the photon is exactly the size of the cavity, V. Of course, this need not be the case. If you were to let your photons fly instead of bounding them, the energy of the photon, like the orbitals of an atomic wave function, technically expand to infinity and thus a photon has no definable size. In our experiments in the lab, the energy of each photon is created at the source and radiates to the detector. If the laser is pulsed, we can be sure that the heavy majority of the photon is contained within the coherence time of the pulse, but this serves to remind you that mathematically, the photon's size is as large as the space you give it to propagate.

There is a mathematical framework for avoiding the constraints of a cavity which instead considers a continuum [9]. This will be helpful when considering the experiments in this thesis which do not occur inside a cavity. Instead of being represented by quantum harmonic oscillators in a cavity, the quantized electromagnetic field modes are represented by continuous wave vectors. To illustrate this change, consider plane waves that traverse a cavity of length L. The allowed standing waves have a minimum frequency difference of $\Delta\omega = \frac{2\pi c}{L}$. Clearly, we move from a cavity to a continuum by taking the limit as $L \to \infty$ which implies there will be no minimum difference in frequency modes: $\Delta\omega \to 0$. Ladder operators are transformed to continuous mode operators by $\hat{a} \to \sqrt{\Delta\omega}\hat{a}(\omega)$ which provides a continuous version of the commutation relation $[\hat{a}(\omega), \hat{a}^\dagger(\omega')] = \delta(\omega - \omega')$ where $\delta(x - x')$ is the dirac delta function. The volume term is written as $V = LA$ where we can substitute $L = \frac{2\pi c}{\Delta\omega}$. Finally, discrete sums which can keep track of the superposition of electric fields with different frequencies inside a cavity are replaced with integrals by the transformation $\sum_k \to \frac{1}{\Delta\omega}\int d\omega$. Starting from Eq. 1.12, dropping the polarization label, and making the substitutions listed above, the continuous mode quantized electric field operator is thus

$$\begin{aligned}\hat{E}(z,t) &= i\frac{1}{\Delta\omega}\int d\omega \sqrt{\frac{\hbar\omega}{2\epsilon_0 A}\left(\frac{\Delta\omega}{2\pi c}\right)}\left(\sqrt{\Delta\omega}\hat{a}(\omega)e^{-i\omega t+ikz} - \sqrt{\Delta\omega}\hat{a}^\dagger(\omega)e^{i\omega t-ikz}\right) \\ &= i\int d\omega \sqrt{\frac{\hbar\omega}{4\pi\epsilon_0 cA}}\left(\hat{a}(\omega)e^{-i\omega t+ikz} - \hat{a}^\dagger(\omega)e^{i\omega t-ikz}\right) \\ &= \hat{E}^{(+)}(z,t) + \hat{E}^{(-)}(z,t),\end{aligned} \tag{1.13}$$

where we have compactly written the electric field operator as the sum of two components $\hat{E}^{(+)}(z,t)$ and $\hat{E}^{(-)}(z,t)$ referred to as the positive and negative frequency components named after the sign in the exponential [1].

[1] From my perspective they are named backwards, but there is old history from the theory of waves and oscillations at play behind the naming convention.

Light carries potential energy through space with its oscillating electric field, but we don't measure the field amplitude directly. Instead, power meters in the lab measure power, which if integrated over time gives the field intensity, $\hat{I}(z,t)$. This operator is the quantum mechanical analog of the classical Poynting vector. The electric field operators in Eq. 1.13 are related to the intensity operator by

$$\begin{aligned}\hat{I}(z,t) &= 2\epsilon_0 c\hat{E}^{(-)}(z,t)\hat{E}^{(+)}(z,t) \\ &= \frac{\hbar}{2\pi A}\int d\omega \int d\omega' \sqrt{\omega\omega'}\hat{a}^\dagger(\omega)\hat{a}(\omega')e^{i(\omega-\omega')(t-\frac{z}{c})},\end{aligned} \tag{1.14}$$

and integration of the intensity provides the total energy of the system. First, integrating with respect to position gives the total energy over the entire z-axis at a given time:

$$A\int_{-\infty}^{\infty} dz\hat{I}(z,t) = c\int d\omega\hbar\omega\hat{a}^\dagger(\omega)\hat{a}(\omega), \tag{1.15}$$

while integrating over all time gives the total energy that passes through a plane at a given z:

$$A\int_{-\infty}^{\infty} dt\hat{I}(z,t) = \int d\omega\hbar\omega\hat{a}^\dagger(\omega)\hat{a}(\omega). \tag{1.16}$$

Both of these expressions include an integral over a photon's energy, $\hbar\omega$, and both ladder operators, $\hat{a}^\dagger(\omega)\hat{a}(\omega)$. These integrals relate the total field energy to the summation of single photon energies at a particular frequency, weighted by the number of photons at that frequency. This counting procedure is formalized by the photon number operator, $\hat{n}$, given by

$$\hat{n} = \int d\omega\hat{a}^\dagger(\omega)\hat{a}(\omega). \tag{1.17}$$

The ladder operators are non-Hermitian operators which do not correspond to a physical observable, while the number operator, a simple multiplication of two ladder operators, is Hermitian and corresponds to the number of photons. We can define ladder operators which create and destroy a photon at a particular time by Fourier transforming their frequency representation as

$$\hat{a}(t) = \frac{1}{\sqrt{2\pi}} \int d\omega \hat{a}(\omega) e^{-i\omega t} \tag{1.18}$$

$$\hat{a}^\dagger(t) = \frac{1}{\sqrt{2\pi}} \int d\omega \hat{a}^\dagger(\omega) e^{i\omega t}, \tag{1.19}$$

and we can rewrite the number operator with respect to the Fourier transformed ladder operators as

$$\hat{n} = \int dt \hat{a}^\dagger(t) \hat{a}(t). \tag{1.20}$$

1.3 Degrees of Freedom of Light

Throughout this thesis, light is the carrier of quantum information. In a beam like geometry, there are four degrees of freedom (DoF) of a single photon - polarization, transverse spatial mode profile (containing two DoF), and spectrum [10], each of which can be used to encode, transfer, and read quantum information. Think of DoF as physical parameters that can be independently manipulated in an experiment. Polarization is the simplest to work with on an optics table as basic linear optics are capable of high fidelity polarization preparation, transformation, and measurement. This DoF is limited to a Hilbert space of two, meaning a single state carries binary information. Spatial modes and spectra, on the other hand, allow access to a theoretically infinite Hilbert space in which to encode information. Orbital Angular Momentum (OAM) modes describe a high dimensional state space in the transverse beam profile limited only by the resolution of current state-of-the-art spatial light modulators (SLM) and other controllable phase modulation optics. As engineering advances and provides a higher SLM spatial resolution, the ability to apply particular phase delays to different coordinates of the transverse mode profile of light will provide access to larger Hilbert spaces. When working with the spectrum of light, the Hilbert space is limited by the spectral resolution of single photon spectrometers, or, equivalently, the temporal resolution of time-of-arrival single photon detectors.

For completeness, one can also consider the number of photons as a degree of freedom [11], but working with this DoF requires expensive and early-stage photon number resolving cryogenic detectors and will not be discussed further. This thesis encompasses a set of experiments utilizing both the polarization and OAM DoF, and more recent work focusing on the spectral DoF. These are described in the following sections.

1.3.1 Polarization

Polarization qubits make for an excellent teaching example for photonic quantum information both in theory, and in the lab as they are straightforward to prepare, superimpose, and measure. The polarization of an electromagnetic field describes the direction of oscillation of the electric field. It is convention to focus on the electric field rather than the orthogonal magnetic field, but due to orthogonality one always knows the direction of oscillation of one when given the other. To begin, consider a photon in an arbitrary superposition of horizontal, $|H\rangle$, and vertical, $|V\rangle$ polarizations as

$$|\Psi\rangle = \cos\left(\frac{\theta}{2}\right)|H\rangle + e^{i\phi}\sin\left(\frac{\theta}{2}\right)|V\rangle \tag{1.21}$$

where $\theta, \phi \in [0, 2\pi)$ are angles that describe the relative combination of $|H\rangle$ and $|V\rangle$. In order to see the similarities between polarization qubits and other physical quantum information systems, it's useful to assign these polarization states to the two-dimensional computational basis,

$$|H\rangle = \begin{pmatrix}1\\0\end{pmatrix}, \; |V\rangle = \begin{pmatrix}0\\1\end{pmatrix}. \tag{1.22}$$

Taking $\theta = 90°$ and $\phi = 0°, 180°$ gives us the diagonal and anti-diagonal states,

$$|D\rangle = \frac{1}{\sqrt{2}}(|H\rangle + |V\rangle) = \frac{1}{\sqrt{2}}\begin{pmatrix}1\\1\end{pmatrix}, \qquad |A\rangle = \frac{1}{\sqrt{2}}(|H\rangle - |V\rangle) = \frac{1}{\sqrt{2}}\begin{pmatrix}1\\-1\end{pmatrix}. \tag{1.23}$$

$|H\rangle, |V\rangle, |D\rangle$, and $|A\rangle$, along with all other states described by Eq. 1.21 with real coefficients, are called linearly polarized states. Starting from one linearly polarized state, it is straightforward to rotate the polarization to any other linearly polarized state with just a half-wave plate (HWP). Taking $\theta = 90°$, and $\phi = 90°, 270°$ gives the right and left circular polarization states,

$$|R\rangle = \frac{1}{\sqrt{2}}(|H\rangle + i\,|V\rangle) = \frac{1}{\sqrt{2}}\begin{pmatrix}1\\i\end{pmatrix}, \qquad |L\rangle = \frac{1}{\sqrt{2}}(|H\rangle - i\,|V\rangle) = \frac{1}{\sqrt{2}}\begin{pmatrix}1\\-i\end{pmatrix}. \tag{1.24}$$

Starting from $|H\rangle$, a quarter-wave plate (QWP) is sufficient to rotate the polarization to either circular polarization state. Combining the action of a quarter-wave and half-wave

plate provides enough freedom to rotate $|H\rangle$ to all polarizations described by Eq. 1.21. Polarizing beam splitters are used for projective measurements and typically transmit horizontal polarization and reflect vertical polarization. Inserting a half and quarter-wave plate before a polarizing beam splitter enables projective measurements onto arbitrary qubit polarization bases.

Using the matrix formalism provided by the computational basis representation, the H/V states are eigenstates of the Pauli σ_z operator, while the D/A and R/L states are eigenstates of the Pauli σ_x and Pauli σ_y operators, respectively. These matrices have the following form,

$$\sigma_z = \begin{pmatrix} 1 & 0 \\ 0 & -1 \end{pmatrix}, \ \sigma_x = \begin{pmatrix} 0 & 1 \\ 1 & 0 \end{pmatrix}, \ \sigma_y = \begin{pmatrix} 0 & -i \\ i & 0 \end{pmatrix}. \tag{1.25}$$

Polarization qubits are easily visualized by plotting the angles that parameterized the state in Eq. 1.21 onto a sphere called the *Bloch sphere*. When referring to the polarization of light and not just an arbitrary qubit, it is called the Poincaré sphere, and both are illustrated in Fig. 1.1. Throughout the thesis, quantum information protocols and concepts will be described using the polarization bases and the Poincaré sphere. Note, when discussing these concepts with quantum information scientists studying other physical qubits, the Bloch sphere is more common and the bases are labeled $\{0, 1\}$, $\{+, -\}$, and $\{+i, -i\}$ instead of $\{H, V\}$, $\{D, A\}$, and $\{R, L\}$, respectively.

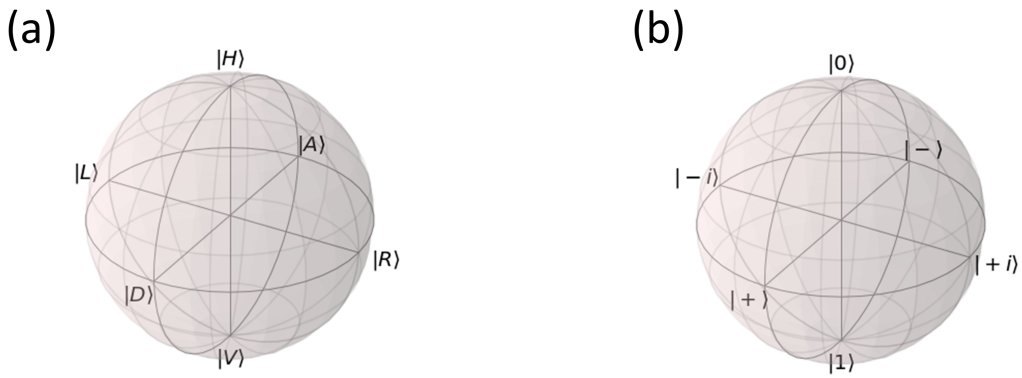

Figure 1.1: Graphical representation of qubit state space. a) Poincaré sphere labelled with polarization bases. b) Bloch sphere labelled with computational bases.

Wave plates are a simple optic consisting of a uniaxial birefringent material such as quartz. Birefringent materials have a polarization dependent index of refraction which manifests as a relative phase delay between polarizations aligned with one axis we call the fast axis, and a perpendicular axis called the slow axis. Wave plates can be represented by 2x2 matrices called the Jones matrices [12] which take the form,

$$HWP(\theta) = \begin{pmatrix} \cos(2\theta) & \sin(2\theta) \\ \sin(2\theta) & -\cos(2\theta) \end{pmatrix} \tag{1.26}$$

$$QWP(\theta) = \begin{pmatrix} \cos^2(\theta) - i\sin^2(\theta) & (1+i)\cos(\theta)\sin(\theta) \\ (1+i)\cos(\theta)\sin(\theta) & -i\cos^2(\theta) + \sin^2(\theta) \end{pmatrix}, \tag{1.27}$$

where θ is the rotation angle of each wave plate about the optic axis and $\theta = 0$ corresponds to the fast axis aligned to the horizontal. It can be helpful to remember what each waveplate takes the $|H\rangle$ state to. For example, a HWP rotated to $+(-)$ 22.5° rotates $|H\rangle$ to $|D\rangle$ ($|A\rangle$), and a QWP rotated to $+(-)$ 45° rotates $|H\rangle$ to $|R\rangle$ ($|L\rangle$).

Operations on a qubit, such as setting a HWP to 22.5° and sending a horizontally polarized photon through, can be visualized as a rotation of the $|H\rangle$ vector on the Poincaré sphere to the $|D\rangle$ vector as seen in Fig 1.2.

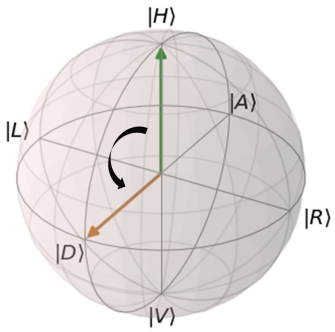

Figure 1.2: Poincaré sphere representation of the action of a HWP at 22.5° acting on a horizontally polarized photonic state. The resulting state is diagonally polarized.

1.3.2 Spatial Modes

Spatial modes of light generally refer to the amplitude and phase of the transverse component of the electromagnetic field. Imagine taking a cross sectional-slice of light perpendicular to the direction of travel. The patterns that emerge are superpositions of orthogonal fields which can be used to encode quantum information. The mathematical representations of the electromagnetic fields and their transverse components are usually derived by combining three of Maxwell's equations to build a wave equation and then solving to find transverse field solutions. In this section, the wave equation is derived, the paraxial approximation, which closely models laser beams in the lab, will be introduced, and the Hermite-Gaussian family of solutions will be presented. Although this thesis explores spatial modes related to the cross-section of light, it should be noted that quantum information can be encoded in the path that light travels [13, 14]. Path encoding can also be considered a spatial mode because it is labeled by a photon's position in space, but will not be discussed further here.

Consider an electromagnetic field in an isotropic, linear, source-free media. Take the curl of Maxwell's Eq. 1.1, and employ the vector identity $\nabla \times \nabla \times \mathbf{A} = \nabla(\nabla \cdot A) - \nabla^2 A$ to get

$$\begin{aligned} \nabla \times \nabla \times \mathbf{E} &= \nabla(\nabla \cdot \mathbf{E}) - \nabla^2 \mathbf{E} \\ \nabla \times \left(-\frac{\partial \mathbf{B}}{\partial t}\right) &= \nabla(\nabla \cdot \mathbf{E}) - \nabla^2 \mathbf{E}. \end{aligned} \tag{1.28}$$

The divergence of $\mathbf{E}$ is zero by Maxwell's Eq. 1.3. Note, the time derivative can be brought outside the curl which leaves the left hand side as $\frac{\partial}{\partial t}(\nabla \times \mathbf{B})$. We can now substitute Maxwell's Eq. 1.2 to bring in a second time derivative to obtain the wave equation

$$\nabla^2 \mathbf{E} = \mu\epsilon \frac{\partial^2 \mathbf{E}}{\partial t^2}. \tag{1.29}$$

The general solution of the wave equation for a wave travelling in a single direction, say, the z direction, is a plane-wave (meaning the field has no transverse dependence) which has the form

$$\mathbf{E}(z,t) = \mathbf{E}_0 \left(t - \frac{z}{v}\right) \tag{1.30}$$

where $\mathbf{E}_0$ is an $x-y$ plane vector and $v = 1/\sqrt{\mu\epsilon}$ is the speed of light in the medium. Plane waves extend their transverse amplitude to infinity and so do not model the collimated laser beams in the lab. That being said, to good approximation, lasers can be considered to be a superposition of plane waves that are travelling close to a single direction, z, and we call beams described by this approximation paraxial. Transverse field variations of paraxial beams are much smaller than variations in the z-direction.

A monochromatic, paraxial wave, ignoring polarization, may be written as

$$E(z,t) = u(x,y,z)e^{i(\omega t - kz)} \tag{1.31}$$

where $u(x,y,z)$ is a slowly-varying envelope relative to the wavelength-scale e^{-ikz} term. Substituting this electric field into the wave equation in Eq. 1.29 yields

$$\nabla^2 \left(ue^{i(\omega t-kz)}\right) = \mu\epsilon \frac{\partial^2}{\partial t^2}\left(ue^{i(\omega t-kz)}\right). \tag{1.32}$$

We will simplify each side of this equation one at a time. First, break the Laplace operator into transverse and z components as

$$\begin{aligned} \text{LHS} &= (\nabla_T^2 + \frac{\partial^2}{\partial z^2})\left(ue^{i(\omega t-kz)}\right) \\ &= e^{i(\omega t-kz)}\nabla_T^2 u + e^{i\omega t}\frac{\partial^2}{\partial z^2}\left(ue^{-ikz}\right) \\ &= e^{i(\omega t-kz)}\nabla_T^2 u + e^{i(\omega t-kz)}\left[\frac{\partial^2 u}{\partial z^2} - 2ik\frac{\partial u}{\partial z} - k^2 u\right] \end{aligned} \tag{1.33}$$

where the chain rule was implemented twice from the second to the last line. Moving to the right hand side and using the relationship $\mu\epsilon = k^2/\omega^2$, we simplify the following:

$$\begin{aligned} \text{RHS} &= \mu\epsilon\frac{\partial^2}{\partial t^2}\left(ue^{i(\omega t-kz)}\right) \\ &= \mu\epsilon u e^{-ikz}\frac{\partial^2}{\partial t^2}e^{i\omega t} \\ &= \mu\epsilon u e^{-ikz}(-\omega^2 e^{i\omega t}) \\ &= -k^2 u e^{i(\omega t-kz)}. \end{aligned} \tag{1.34}$$

Setting the LHS = RHS, we arrive at a differential equation of $u(x, y, z)$,

$$\nabla_T^2 u + \frac{\partial^2 u}{\partial z^2} - 2ik\frac{\partial u}{\partial z} = 0. \tag{1.35}$$

Due to the slowly-varying property of the envelope $u(x, y, z)$,

$$\left|\frac{\partial^2 u}{\partial z^2}\right| \ll 2k\left|\frac{\partial u}{\partial z}\right|, \tag{1.36}$$

and we can neglect the second derivative of u with respect to z yielding the paraxial wave equation:

$$\nabla_T^2 u - 2ik\frac{\partial u}{\partial z} = 0. \tag{1.37}$$

The Hermite-Gauss (HG) modes are a family of solutions to the paraxial wave equation. They are labeled and categorized by two indices, $m, n \in \mathbb{Z}$, and given by the formula

$$u_{mn} = \frac{1}{w(z)} H_m\left(\frac{\sqrt{2}x}{w(z)}\right) H_n\left(\frac{\sqrt{2}y}{w(z)}\right) e^{-(x^2+y^2)/w^2(z)} e^{-ik(x^2+y^2)/2R(z)} e^{i(m+n+1)\phi(z)}, \tag{1.38}$$

where we have introduced the beam radius,

$$w^2(z) = w_0^2\left[1 + \left(\frac{z}{z_R}^2\right)\right], \tag{1.39}$$

the radius of curvature,

$$R(z) = \frac{z^2 + z_0^2}{z}, \tag{1.40}$$

the beam is focused at $z = 0$ with radius w_0, $\phi(z) = tan^{-1}\left(\frac{z}{z_R}\right)$, the Rayleigh range, $z_R = \pi\omega_0^2 n_r/\lambda$, is the distance light travels while maintaining only a slow increase in beam radius, n_r is the index of refraction, where the subscript is used to differentiate from the

mode number n, and $H_\nu(\xi)$ are Hermite polynomials. These modes are termed Transverse Electromagnetic Modes (TEM_{mn}), and higher mode numbers correspond to more complicated intensity patterns with regions alternating between high and low intensity. Figure 1.3 shows the intensity patterns corresponding to the first few TEM modes which are the result of the squared modulus of the field amplitude, $|u_{mn}(x, y, z)|^2$.

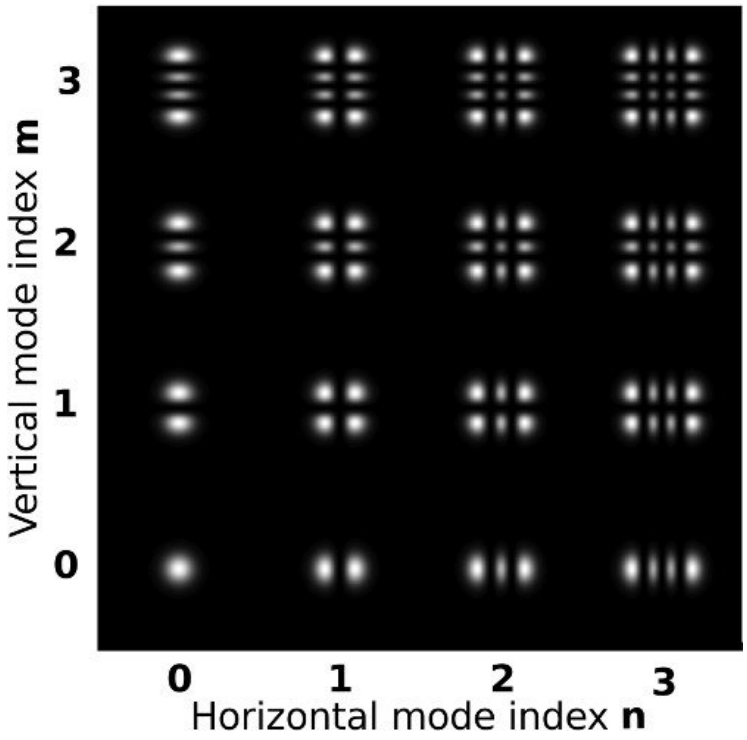

Figure 1.3: Intensity patterns of Hermite-Gauss (HG) modes with varying mode indices. © L. Carbone et al., (2013) [1].

The lowest order solution, TEM_{00}, is of particular interest and has the following form:

$$u_{00}(x, y, z) = \frac{w_0}{w(z)} e^{-(x^2+y^2)/w^2(z)} e^{-ik(x^2+y^2)/2R(z)} e^{i\phi(z)}. \tag{1.41}$$

This mode is a 2D-Gaussian function and is sometimes referred to as the single spatial mode. It is the dominant spatial mode output from many laser resonators in which the curvature of the cavity mirrors is matched with the radius of curvature, $R(z)$, of the desired beam output. Single mode fibers are used throughout this thesis because they collect/output only the TEM_{00} spatial mode. They have a very small core of $\sim 5\mu$m

diameter which filters all higher order modes. Some experiments prefer to collect higher order spatial modes of light when coupling from free-space to fiber, and can do so with multi-mode fibers. These have a larger core size of anywhere between $10\mu\text{m} - 100\mu\text{m}$ in diameter.

1.3.3 Orbital Angular Momentum

A particularly interesting family of solutions to the paraxial wave equation describe beams of light that have an azimuthal phase dependency, $e^{il\phi}$, which are referred to as vortex beams. A 2D cross section of such a beam reveals a phase singularity at the coordinate which the phase is varying around with angle ϕ [15]. At this point, the phase is undefined and the intensity is zero. These singularities are called optical vortices and can occur sporadically in nature [16], or be specifically engineered with a particular azimuthal phase dependence. In 3D space, as light propagates, a phase singularity draws out a line at which the phase is undefined, and the azimuthal phase dependence carves out a helical phase pattern around the singularity. These beams can have multiple interwoven helical phase fronts counted by the unbounded integer $l \in \{-\infty, ..., -1, 0, 1, ..., \infty\}$ and carry orbital angular momentum (OAM), $l\hbar$, per photon. The sign of l determines the handedness of the helical phase, and beams with opposite handedness have seen applications in determining the chirality of molecules and materials [17].

The unbounded nature of the helicity parameter, l, provides access to a large alphabet in which quantum information can be encoded in a single photon. Two-level quantum systems, or qubits, were introduced during the discussion of polarization. Here, OAM is a vehicle to introduce a d-dimensional system called a qudit, where instead of being constrained by a two-dimensional Hilbert space, we are limited only by our engineering capability of preparation and measurement of higher-order modes. Higher dimensional optical quantum states have lead to applications in quantum cryptography [18], quantum communication [19, 2], and quantum computing [20].

To introduce a mathematical formalism for vortex beams, we move to the cylindrical coordinates (r, ϕ, z) and represent the electric field as

$$E(r, \phi, z, t) = A(r, \phi, z)e^{-i(\omega t - kz)}, \tag{1.42}$$

where $A(r, \phi, z)$ is the complex amplitude of the field and contains the spatial distribution of a 2D cross section of light. In the case of vortex beams, the amplitude can be written as a superposition of helical modes labelled by their azimuthal number, l, as

$$A(r, \phi, z) = \sum_l c_l(r, z) e^{il\phi} \tag{1.43}$$

where coefficients c_l are determined by the angular Fourier transform of the field amplitude as

$$c_l(r, z) = \frac{1}{2\pi} \int_0^{2\pi} d\phi e^{-il\phi} A(r, \phi, z). \tag{1.44}$$

By radially integrating the absolute value squared of these coefficients, we get the probability, $P(l)$, that a photon is in the l OAM state as

$$P(l) = \frac{1}{B} \int_0^{\infty} dr r |c_l(r, z)|^2 \tag{1.45}$$

where the probability is normalized by the transverse plane beam power,

$$B = \sum_l \int_0^{\infty} dr r |c_l(r, z)|^2. \tag{1.46}$$

Note, the probability is not dependent on the longitudinal coordinate z because OAM is conserved as light propagates [21]. A full analysis of the transverse spatial mode requires reference to the radial component of the field. While there are many spatial modes with helical phase factors which differ in their radial amplitude, it is most common to focus on field amplitudes, A, which are written as superpositions of Laguerre-Gaussian modes, $LG_{p,l}$. These are analytic solutions to the wave equation in the paraxial approximation, Eq. 1.37. Similar to the $\text{TEM}_{m,n}$ modes, $LG_{p,l}$ modes are described in reference to special functions and are labelled by two indices. Before, m, n were indices that indicated x and y structure. Now that we have moved to cylindrical coordinates, we used the mode indices p, l to refer to radial and azimuthal structure. $LG_{p,l}$ modes have a lengthy derivation, so only the results will be presented here. Interested readers looking for a detailed derivation of the Laguerre-Gaussian modes are encouraged to visit reference [22]. Introducing dimensionless cylindrical coordinates $\rho = r/w_0$ and $\zeta = z/z_R$, Laguerre-Gaussian modes are represented as

$$LG_{p,l}(\rho,\zeta,\phi) = \sqrt{\frac{2^{|l|+1}p!}{\pi(p+|l|)!(1+\zeta^2)}}\left(\frac{\rho}{\sqrt{1+\zeta^2}}\right)^{|l|} \times e^{\frac{-\rho^2}{1+\zeta^2}} L_p^{|l|}(2\rho^2/(1+\zeta^2)) e^{\frac{i\rho^2}{\zeta+1/\zeta}} e^{il\phi - i(2p+|l|+1)\tan^{-1}(\zeta)}, \tag{1.47}$$

where $p \in \{0,1,2,...\}$, and $L_p^{|l|}(\xi)$ are generalized Laguerre polynomials. Superpositions of these modes give a more radially detailed picture of the electric field amplitude, A, as

$$A(r,\phi,z) = \sum_p \sum_l b_{p,l} LG_{p,l}(r,\phi,z), \tag{1.48}$$

and we can relate these new coefficients $b_{p,l}$ with the angular Fourier transform coefficients from before using

$$b_{p,l} = \int_0^\infty r dr LG^*_{p,l}(r,\phi,z) e^{-il\phi} c_m(r,z). \tag{1.49}$$

Similar to the $\text{TEM}_{m,n}$ modes discussed earlier, Fig 1.4 shows the first few $LG_{p,l}$ intensity patterns. Increasing the radial index adds rings to the intensity pattern, but it is less clear how the azimuthal index changes the state by looking at intensity. This is because intensity measurements wash out the phase of an electromagnetic field, and the azimuthal number refers to the helicity of the phase, $e^{il\phi}$.

The intensity patterns in Fig 1.4 show the theoretical distribution of light in the transverse plane. When measuring the transverse profile of single photons, we use arrays of single photon detectors, also known as single photon cameras. A single measurement will only light up one pixel of the camera. It's only after many subsequent measurements of photons with similar phase patterns that the doughnut shaped intensity patterns emerge. This build up of data can be visualized in Fig 1.5. It should be noted that although $l = 1$ and $l = -1$ LG modes have the same intensity pattern, a superposition of both yields a unique intensity pattern. Using this idea, if you only have access to intensity measurements, it's possible to measure the LG coefficients $b_{p,l}$ by interfering the signal with a reference wave that has identical polarization and frequency and a known spatial distribution [21].

There are many ways to generate OAM states experimentally, including spiral phase plates (SPP), q-plates, fork dislocations, spatial light modulators (SLMs), and metasurfaces. The simplest to describe, and perhaps the most elegant, is the SPP. A SPP is a

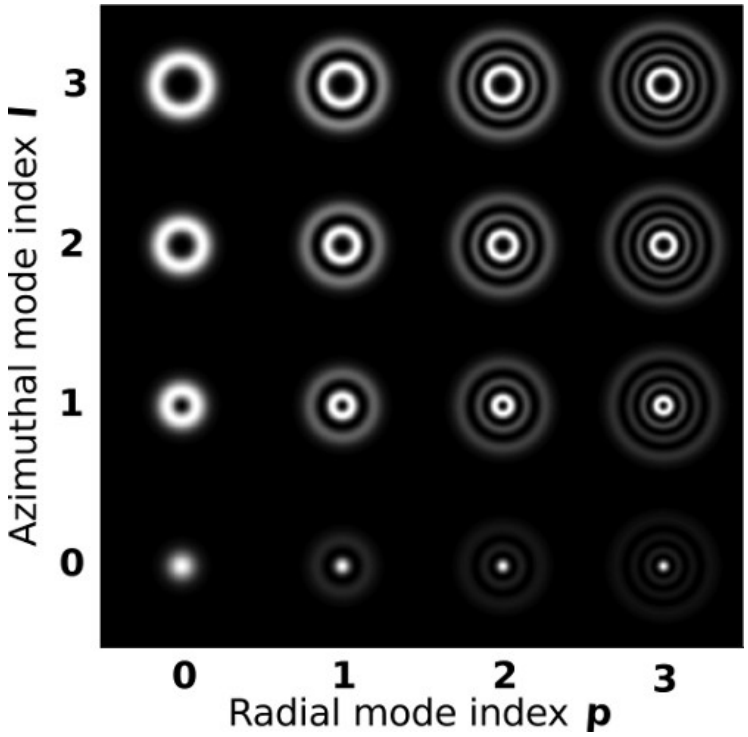

Figure 1.4: Intensity patterns of Laguerre-Gaussian (LG) modes with varying mode indices. © L. Carbone et al., (2013) [1].

piece of glass that has thickness which varies with azimuthal angle, ϕ. An input Gaussian beam will therefore have each transverse coordinate of the electric field delayed based on its azimuthal coordinate, i.e., how much time the light spent in the glass [23]. With this method, each OAM state you may want to prepare requires a particular SPP tailored to your desired output. A similar device with slightly more versatility is the q-plate. These devices have a birefringence that varies across the face of the optic, which leads to the output OAM state being dependent on the input polarization [24]. Specifically, the original q-plates transformed right circularly-polarized light to OAM with $l = 2q$ where q is a fabrication controlled integer relating to glass thickness and birefringence, and transformed left circularly polarized glass to OAM with $l = -2q$. Similar to waveplates discussed in Sec. 1.3.1, q-plates can be described by Jones matrices with the form

$$\mathbf{M} = \begin{pmatrix} \cos(2\alpha) & \sin(2\alpha) \\ \sin(2\alpha) & -\cos(2\alpha) \end{pmatrix}, \tag{1.50}$$

where $\alpha(r, \phi) = q\phi + \alpha_0$, and α_0 is a constant. Circularly polarized light carries spin-angular momentum (SAM), so q-plates are an example of spin-orbit coupling where the OAM component of light is dependant on the SAM component.

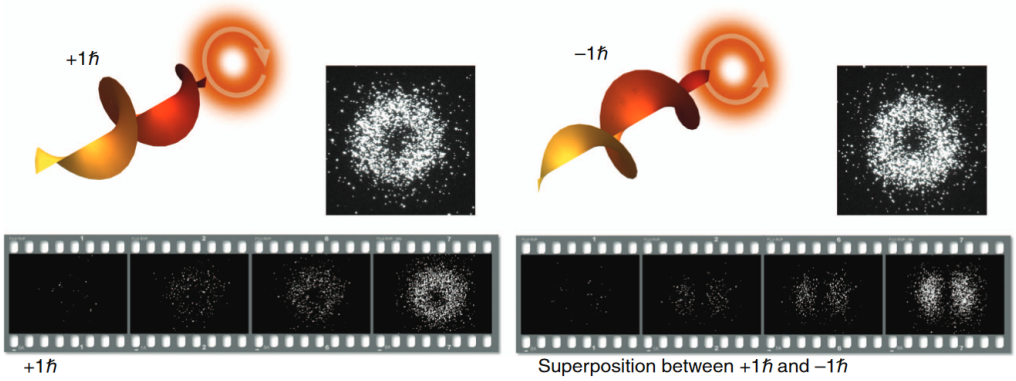

Figure 1.5: Single photon images built up over many measurements. © Fickler et al., (2013) [2, 3].

While it is straightforward to associate right circularly polarized light with "spinning" of the electric field, and OAM with an angular phase dependence, it can be less obvious how these particular instances of light relate to spin and orbital angular momentum. To address this, it is much easier to think about what happens when light with SAM or OAM interacts with an atom. Circularly polarized light will transfer spin angular momentum to an atom and has been used to rotate quartz waveplates [25], while light with helical phase patterns will transfer orbital angular momentum to an atom causing the atom to revolve around the optical singularity [26, 27]. These mechanical forces due to OAM transfer have since been applied to optical tweezers [28], which are light beams that trap and manipulate atoms. The familiar analogy of the earth-sun system may help to visualize. The earth spins on its axis with SAM, and revolves around the sun with OAM, much like the atom described in a light beam.

Optics with fork dislocations, also known as screw dislocations, will impart helical phase patterns on light beams that pass through [29]. Fork dislocations have also been applied to beams by holographically imprinting a fork pattern onto a beam using a grating mask [30]. Most recent single photon OAM experiments use SLMs in order to prepare and measure higher level OAM modes in a programmable way, the first demonstration of which was done by Gibson et al. [31]. You could consider these SLM preparations as more on-the-fly programmable successors to the fork dislocation methods, because the pattern encoded in

the SLM to produce OAM states is also fork-shaped. It's worth noting that in the broader community, spatial light modulators are known for modulating beam intensity, such as the overhead transparencies used in presentations [2]. In contrast, for OAM purposes, we are always referring to SLMs which modulate the phase of light at different spatial positions.

The last generation and measurement method I will mention uses metasurfaces. These are artificially fabricated thin materials with small scale structures across the transverse face. They modulate the electromagnetic field either through transmission or reflection and can generally be printed with finer, sub-wavelength spatial resolution than state-of-the-art SLMs. [32, 33, 34]

1.3.4 Time & Frequency

The time-frequency degree of freedom provides another high-dimensional Hilbert space for encoding quantum information. Unlike OAM states which are essentially washed out during fiber transmission [1], it is robust against decoherence over long-distance fiber networks of up to 100 kilometers [37, 38, 39]. Additionally, polarization mode-dispersion, which can complicate fiber networks using polarization states, does not affect the time-frequency degree of freedom. For quantum communication specifically, energy-time entanglement is being considered to take advantage of the current telecommunications infrastructure around the world which already encodes classical information in frequency and time [40]. I will discuss three quantum information encodings associated with the time and frequency of single photons. The first two consider a single property of light by discretizing the continuous range, of either time-of-arrival or frequency, into bins. The third encoding, referred to as temporal-mode encoding, uses the continuous nature of time and frequency simultaneously.

Time-bin encoding makes use of an unbalanced Mach-Zehnder interferometer as illustrated in Fig. 1.6. Photons which take the shorter path are given the label $|e\rangle$ for "early", while photons taking the longer path are denoted $|l\rangle$ for "late". A coherent superposition of the form

$$|\Psi\rangle = \alpha\,|e\rangle + \beta\,|l\rangle \tag{1.51}$$

[2] maybe a relic of the past for some younger readers, but in 2019 I saw Roger Penrose give a talk at Perimeter using only overhead transparency slides so they're still out there.

[1] There are OAM preserving fibers, but they only preserve a specific target spatial mode [35]. Currently, regular multimode fibers are not sufficient for OAM preservation in quantum optics experiments [36].

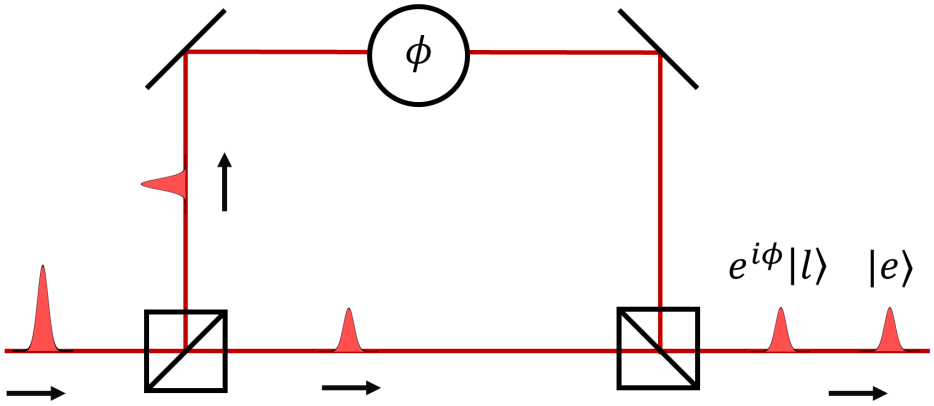

Figure 1.6: Illustration of an unbalanced Mach-Zehnder interferometer generating time-bin states.

is created by varying the amplitude and phase of each path of the interferometer. Amplitudes may be varied by changing the reflectivity of the beamsplitters and thus the portion of photons in each path, while phase may be varied by changing relative path length. Beamsplitters in interferometers are not easy to change out quickly, so it is simpler to implement relative phase differences and fix the amplitudes. Measurement of time-bin states can also be done with a Mach-Zehnder (MZ) interferometer, although single photon detectors may be sufficient if the separation time between $|e\rangle$ and $|l\rangle$ is longer than detector resolution. High-dimensional time bin states can be made by increasing the number of time slots for the encoding, for example using cascaded MZ interferometers [41]. The time difference between each bin is limited by photon coherence length. If the bins are too close together, it is not possible to deterministically distinguish the two paths.

Frequency bin encoding is conceptually similar with the frequency of light defining the different basis states instead of the time-of-arrival. Frequency bin states can be created using ring resonators which produce a frequency "comb" and have been integrated into silicon chips [42, 43]. Relative phases between bins can be applied using Fourier domain pulse shaping in which pulses are stretched out in space into their frequency components with gratings or prisms and an SLM is used to apply the relative phases [44]. Superpositions are made possible by phase modulators that can selectively interfere particular frequency bins, and measurements are made with single photon spectrometers. To avoid the loss in spectrometers, it is also possible to measure frequency bins using a series of dichroic

mirrors. Similar to the time-bin resolution problem, any detection method must have higher spectral resolution than the spacing of frequency bins to ensure deterministic readout.

An optical pulse can be decomposed into orthogonal functions that describe the frequency and temporal profile. In Sec. 1.3.2 the electric field as a function of position was described by 2D Hermite-Gauss modes. In the temporal mode framework, the 1D representation of these functions can also be used to describe the electric field as a function of time or frequency instead. Temporal modes can be produced using pulsed light to pump a spontaneous parametric downconversion (SPDC) crystal. Specific modes can be selected for routing or measurement using a quantum pulse gate [45] which uses sum-frequency generation (SFG) to combine the signal with a spectrally engineered gate pulse [46]. In addition to quantum communication which time and frequency bin encodings are often used for, temporal modes have been touted as a basis for optical quantum computing [10].

1.4 Quantum Entanglement

Quantum entanglement is possibly the most astonishing phenomenon in quantum mechanics. It was first postulated in 1935 by Einstein, Podolsky, and Rosen [47], the three authors which to this day entangled particles, or EPR pairs, are named after. The authors used the hard-to-believe concept of entanglement that came with their prediction as an argument that quantum mechanics was an unfinished theory that did not describe reality in its current form. In 1964, John Bell responded to their claim by narrowing down exactly what constraints reality must abide by if it is truly described by quantum mechanics, stating that quantum mechanics is incompatible with local hidden-variable theories [48]. Clauser, Horne, Shimony, and Holt proposed a test of Bell's theorem that could be implemented experimentally [49]. The test amounted to four, two-particle correlation measurements which combined to create the CHSH inequality, also known as a Bell inequality, which, if violated, would rule out local hidden-variable theories. Aspect, Grangier, and Roger were the first to experimentally violate this inequality by measuring the polarization of correlated photons in 1981[50].

As bothered as the EPR authors seemed to be by their prediction, this experiment was the first of many to disprove local-realism, i.e. the principles of locality and realism could not both be true. Locality is the notion that particles can only be affected by their surroundings, and realism is the theory that describes a particle as having a definite state before it is measured. Entanglement, now experimentally verified, began to be considered as a resource for quantum communication. Superdense coding, proposed by Bennett and Weisner [51] and experimentally demonstrated by Zeilinger et al. [52], uses maximally

entangled states as a resource shared by a sender and receiver to send two bits of classical information by only sending a single qubit. Quantum teleportation, proposed by Bennett et al. [53] and again experimentally demonstrated by Zeilinger et al. [54], allows the receiver to transport the state of a qubit by sending a classical bit. Entanglement is a property of generic multi-particle quantum systems, but photons in particular played an important role in the pivotal experiments proving its existence and using it as a resource. Note, the original experimental CHSH violations have a number of small issues which have been the topic of much debate. In the decades since that experiment, there have been many experiments that closed so-called "loopholes" that could be exploited to show local hidden-variable theories may indeed describe the experimental outcomes. With each experiment, the likelihood that nature obeys local-realism diminishes further [55].

1.4.1 CHSH inequality

Here, an experiment is described to derive the CHSH inequality and use it as a working example to introduce two qubit states. A source prepares two particles in a repeatable manner. Each particle is sent to a different party, Alice and Bob. They both have two measurement apparatuses which are capable of measuring physical properties of the particle they receive. Call the properties Alice can measure P_Q and P_R, and the properties Bob can measure P_S and P_T. When either party receives a particle, they flip a coin to decide which measurement to take. Each of the four physical properties can result in a measurement outcome of either 1 or -1. We will give the label Q to the outcome of the measurement of P_Q, and follow a similar convention for $R, S,$ and T. Now, set Alice and Bob far apart from each other and time the experiment such that they receive and measure their particle at the same time. Say they are far enough apart that the outcome of one party's measurement is unable to affect the other due to physical influences being limited by the speed of light [56].

If this experiment is repeated many times, we can build up a list of the four outcome pairs, $QS, RS, RT,$ and QT. Consider the following expression of these measurement outcome pairs:

$$QS + RS + RT - QT = (Q + R)S + (R - Q)T. \tag{1.52}$$

Note that $(Q + R) = 0$ if $Q \neq R$, and $(Q - R) = 0$ if $Q = R$. From this we can see that Eq. 1.52 is equal to either ± 2. Next, we can introduce state probabilities. Say that $p(q, r, s, t)$ is the probability that the system is in a state where $Q = q, R = r, S = s,$ and $T = t$ before Alice and Bob perform their measurements. The mean value, $\mathbf{E}(\cdot)$, of our algebraic quantity is written as

$$\begin{aligned}\mathbf{E}(QS+RS+RT-QT) &= \sum_{qrst} p(q,r,s,t)(qs+rs+rt-qt) \\ &\leq \sum_{qrst} p(q,r,s,t)(2) \\ &= 2\sum_{qrst} p(q,r,s,t) \\ &= 2.\end{aligned} \tag{1.53}$$

where to move from the first to the second line we have taken the largest possible value of $(qs+rs+rt-qt)$ which is 2 (See Eq. 1.52). We can also implement the distributive property on the RHS of the first line to get

$$\begin{aligned}\mathbf{E}(QS+RS+RT-QT) &= \sum_{qrst} p(q,r,s,t)qs + \sum_{qrst} p(q,r,s,t)rs \\ &\quad + \sum_{qrst} p(q,r,s,t)rt - \sum_{qrst} p(q,r,s,t)qt \\ &= \mathbf{E}(QS)+\mathbf{E}(RS)+\mathbf{E}(RT)-\mathbf{E}(QT).\end{aligned} \tag{1.54}$$

We can equate Eq. 1.53 and Eq. 1.54 to obtain the CHSH inequality,

$$\mathbf{E}(QS)+\mathbf{E}(RS)+\mathbf{E}(RT)-\mathbf{E}(QT) \leq 2. \tag{1.55}$$

Experimentally, Alice and Bob can estimate the mean of all four quantities by repeating the experiment many times. The classical CHSH bound for general measurements described in this simple experiment is 2, but introducing quantum systems which are entangled changes the game.

Consider a source that prepares a two-qubit state of the form

$$\left|\Psi^-\right\rangle = \frac{|HV\rangle - |VH\rangle}{\sqrt{2}}, \tag{1.56}$$

where $|HV\rangle = |H\rangle \otimes |V\rangle$ represents a photon with horizontal polarization in one local Hilbert space and a second photon with vertical polarization in a second local Hilbert space. Alice will measure the observables,

$$Q = \sigma_z \qquad R = \sigma_x, \tag{1.57}$$

on her qubit while Bob will measure the observables,

$$S = \frac{-\sigma_z - \sigma_x}{\sqrt{2}} \qquad T = \frac{\sigma_z - \sigma_x}{\sqrt{2}}, \tag{1.58}$$

on his qubit. Average values of the outcome of QS, denoted $\langle QS \rangle$, can be calculated as

$$\begin{aligned}
\langle QS \rangle &= \left\langle \Psi^- \right| (Q \otimes S) \left| \Psi^- \right\rangle \\
&= \left(\frac{\langle HV| - \langle VH|}{\sqrt{2}} \right) \left(\sigma_z \otimes (\frac{-\sigma_z - \sigma_x}{\sqrt{2}}) \right) \left(\frac{|HV\rangle - |VH\rangle}{\sqrt{2}} \right) \\
&= \frac{-1}{2\sqrt{2}} (\langle HV| - \langle VH|)(\sigma_z \otimes \sigma_z + \sigma_z \otimes \sigma_x))(|HV\rangle - |VH\rangle) \\
&= \frac{-1}{2\sqrt{2}} (\langle HV| - \langle VH|)(-|HV\rangle + |VH\rangle + |HH\rangle + |VV\rangle) \\
&= \frac{-1}{2\sqrt{2}} (-2) \\
&= \frac{1}{\sqrt{2}}
\end{aligned} \tag{1.59}$$

where the distributive property of tensor products was used from the second to the third line, the Pauli matrix properties $\sigma_z |H\rangle = |H\rangle$, $\sigma_z |V\rangle = -|V\rangle$, $\sigma_x |H\rangle = |V\rangle$, and $\sigma_x |V\rangle = |H\rangle$ are used from the third to the fourth line, and the orthonormality of basis states $\langle H|V\rangle = \langle V|H\rangle = 0$, and $\langle H|H\rangle = \langle V|V\rangle = 1$ was used from the fourth to the fifth line. Similarly, the three other expectation values can be calculated,

$$\langle RS \rangle = \frac{1}{\sqrt{2}}, \quad \langle RT \rangle = \frac{1}{\sqrt{2}}, \quad \text{and } \langle QT \rangle = \frac{-1}{\sqrt{2}}. \tag{1.60}$$

substituting these quantities in to the CHSH inequality gives

$$\langle QS \rangle + \langle RS \rangle + \langle RT \rangle - \langle QT \rangle = 2\sqrt{2}. \tag{1.61}$$

This is a clear violation of the classical bound of 2. States which violate this equality are called entangled states, and the $|\Psi^-\rangle$ state used for this example is a maximally entangled

state meaning it reaches the upper quantum bound of $2\sqrt{2}$. $|\Psi^-\rangle$ is one of the four Bell states, which are written as

$$\begin{aligned}
\left|\Phi^+\right\rangle &= \frac{|HH\rangle + |VV\rangle}{\sqrt{2}}, \\
\left|\Phi^-\right\rangle &= \frac{|HH\rangle - |VV\rangle}{\sqrt{2}}, \\
\left|\Psi^+\right\rangle &= \frac{|HV\rangle + |VH\rangle}{\sqrt{2}}, \\
\left|\Psi^-\right\rangle &= \frac{|HV\rangle - |VH\rangle}{\sqrt{2}},
\end{aligned} \tag{1.62}$$

which together make a complete two-qubit basis that any two-qubit system can be described by. States which obey the classical limitation of the CHSH inequality are called separable states and can be written as a tensor product of two one-qubit states,

$$|\Psi\rangle = |\phi\rangle \otimes |\phi'\rangle \,. \tag{1.63}$$

When a joint state is separable, it is possible to independently describe each single qubit state it is comprised of. In this section, entanglement was introduced with an operational definition as a state that exceeds the classical bound of the CHSH inequality. The formal definition of an entangled state is a state which is not separable.

1.4.2 GHZ States

Entanglement can also be extended to more than two particles. Much like how the Bell states are a maximally entangled two-qubit state, GHZ states are maximally entangled d-qubit states. For example, the three-qubit GHZ state is written as

$$\left|\mathrm{GHZ}^+\right\rangle = \frac{1}{\sqrt{2}}(|HHH\rangle + |VVV\rangle). \tag{1.64}$$

Interestingly, measuring one of the three qubits in the orthogonal D/A basis prepares a Bell state between the remaining two qubits. This makes the GHZ state a valuable resource in quantum information because Bell states are often produced probabilistically, while a

GHZ state gives access to an on-demand Bell state. Photon GHZ states are in general very difficult to produce with both high count rates and high fidelity [57]. For example, Hübel et al. generated GHZ states with triple coincidence count rates around four counts per hour using cascaded SPDC sources [58]. Two of these three-qubit GHZ states may be combined using entanglement swapping to entangle four qubits together [59]. Continuing this process, small entangled clusters can be combined to generate a network of entangled qubits called a cluster state [60]. Generation of cluster states using this technique is referred to as ballistic quantum computing [61]. For this reason, GHZ states may play a critical role in photonic quantum computing in the future.

GHZ states are not limited to two-level systems. In theory, higher dimensional systems such as those presented in the discussion of spatial and time-frequency modes can be entangled to create d-dimensional GHZ states with the form

$$|\text{GHZ}\rangle = \frac{1}{\sqrt{d}} \sum_{i=0}^{d-1} |i\rangle \otimes ... \otimes |i\rangle \,. \tag{1.65}$$

1.4.3 Density Matrix Formalism

So far throughout the thesis, the bra-ket notation, $\langle|\rangle$, has been used to indicate the state vector describing a quantum state. We have seen entangled state vectors describing multi-particle states; however, a state vector cannot describe particle 1 in an entangled state precisely because it isn't possible to separate the state into two separate Hilbert spaces. In order to describe the state of particle 1, we introduce a more general description of quantum states involving density operators, denoted ρ, also known as state operators [62]. The density operator is defined as

$$\rho = \sum_{\alpha} p_\alpha \, |\phi_\alpha\rangle \, \langle\phi_\alpha| \,, \tag{1.66}$$

where the system has probability p_α of being in state $|\phi_\alpha\rangle$. This operator can be represented by a $d \times d$ matrix called the density matrix, where d is the dimension of the quantum state vectors $|\phi_\alpha\rangle$. Expectation values of a physical property A are given by

$$\langle A\rangle = \sum_{\alpha} p_\alpha \, \langle A\rangle_\alpha = \sum_{\alpha} p_\alpha \, \langle\phi_\alpha| \, A \, |\phi_\alpha\rangle = \text{Tr}(\rho A). \tag{1.67}$$

The density operator is Hermitian, meaning it is self adjoint: $\rho = \rho^\dagger$. It has unit trace, $\mathrm{Tr}(\rho) = 1$, and is positive-semidefinite, i.e. $\langle\phi|\,\rho\,|\phi\rangle \geq 0$ for all $|\phi\rangle$. If there are two or more terms in the sum $\sum_\alpha$, we say that the quantum state is a probabilistic mixture, or mixed state, and the sum carried out in Eq. 1.66 represents an incoherent mixture as opposed to the coherent superpositions symbolized by the addition of state vectors. If there is only one term, we say that the state is *pure*, and the equality $\rho^2 = \rho$ holds. So far, all states described in this thesis have been pure states, but the states we create in the lab are only approximately pure.

Density operators of different quantum systems ρ and ρ' can be compared to understand the degree of similarity between them. Fidelity is a measurement of similarity which can be calculated using the formula

$$F(\rho, \rho') = \left(\mathrm{Tr}\sqrt{\sqrt{\rho'}\rho\sqrt{\rho'}}\right)^2. \tag{1.68}$$

In the special case where both density matrices represent pure quantum states, the fidelity equation simplifies to

$$F(\rho, \rho') = |\,\langle\psi_\rho|\psi_{\rho'}\rangle\,|^2, \tag{1.69}$$

where $\rho = |\psi_\rho\rangle\,\langle\psi_\rho|$ and $\rho' = |\psi_{\rho'}\rangle\,\langle\psi_{\rho'}|$ [63].

We have seen how CHSH inequalities are maximally violated by Bell states and not violated by separable states. Fidelity can also be used to differentiate separable and entangled states when the density matrix is known. This is done by calculating the fidelity of the state with each of the four Bell states and taking the highest fidelity value of the four. A qubit separable state can not achieve a Bell state fidelity of more than 0.5, while a Bell state will acheive a fidelity of exactly 1 [64]. Therefore, states with a Bell state fidelity greater than 0.5 are entangled. This metric is an example of an entanglement witness and is a sufficient condition for demonstrating entanglement.

To describe the state of particle 1 in an entangled state, we introduce the reduced density operator,

$$\rho^{(1)} = \mathrm{Tr}_2\rho, \tag{1.70}$$

where we are assuming the global state space is a tensor product of two Hilbert spaces, $\mathcal{H}_1 \otimes \mathcal{H}_2$, particle 1 is in $\mathcal{H}_1$, ρ is the global density operator, and Tr_2 is the partial trace which represents a trace on the space $\mathcal{H}_2$ and can be computed with the formula

$$\mathrm{Tr}_2(\rho) = \sum_j (I \otimes \langle \phi_j |)\rho(I \otimes |\phi_j\rangle), \tag{1.71}$$

where $|\phi_j\rangle$ is any orthonormal basis for the Hilbert space $\mathcal{H}_2$. Now, we can calculate the expectation value of an operator A which only depends on particle 1 as

$$\langle A \rangle = \mathrm{Tr}(\rho^{(1)} A). \tag{1.72}$$

As an example, consider the global two-photon Bell state given by

$$\left|\Phi^+\right\rangle = \frac{1}{\sqrt{2}}(|HH\rangle + |VV\rangle). \tag{1.73}$$

The reduced density operator of this state is

$$\begin{aligned} \rho^{(1)} &= \mathrm{Tr}_2 \rho \\ &= \mathrm{Tr}_2 \left|\Phi^+\right\rangle \left\langle\Phi^+\right| \\ &= \frac{1}{2}\left[(I \otimes \langle H|) \left|\Phi^+\right\rangle \left\langle\Phi^+\right| (I \otimes |H\rangle) + (I \otimes \langle V|) \left|\Phi^+\right\rangle \left\langle\Phi^+\right| (I \otimes |V\rangle)\right] \\ &= \frac{1}{2}\left[|H\rangle \langle H| + |V\rangle \langle V|\right], \end{aligned} \tag{1.74}$$

where we have chosen the computational basis, $|H\rangle / |V\rangle$, as our orthonormal basis to compute the partial trace in Eq. 1.71. Even though the global state, ρ, was in a pure state, particle 1 is in a mixed state with an incoherent mixture of $|H\rangle$ and $|V\rangle$. Using the Poincaré sphere for visualization introduced in Sec. 1.3.1, mixed states can be represented as vectors with length less than one inside the surface of the sphere.

1.4.4 Concurrence

Measures of entanglement are a widely discussed topic in quantum information science [65]. Bell state fidelity as an entanglement witness is useful for classifying states as entangled or separable, but it doesn't order entangled states and claim that one entangled state is more entangled than another. There are many ways to quantify entanglement which can

be used in different situations [66, 67]. I will focus on concurrence and tangle which have been favoured by many experimental physicists and can be analytically computed [68, 69].

Concurrence is defined for two qubit states with density matrix ρ as

$$C(\rho) = \max\{0, \lambda_1 - \lambda_2 - \lambda_3 - \lambda_4\}, \tag{1.75}$$

where λ_i are the eigenvalues, in decreasing order, of the matrix

$$\sqrt{\sqrt{\rho}(\sigma_y \otimes \sigma_y)\rho^*(\sigma_y \otimes \sigma_y)\sqrt{\rho}}, \tag{1.76}$$

where $*$ indicates complex conjugate and matrix square roots are calculated by diagonalizing the matrix and taking the square root of each of the diagonal elements. This formula simplifies for a pure state to

$$C(\rho) = \sqrt{2[1 - \mathrm{Tr}(\rho_1^2)]}. \tag{1.77}$$

where ρ_1 is the reduced density operator describing particle 1. The concurrence of a separable state is zero, the concurrence of a maximally entangled state is one, and, in general, higher concurrence values indicate a state is more entangled. The square of concurrence is referred to as *tangle* and is often reported instead.

Another commonly discussed entanglement measure, especially among theorists, is *entanglement of formation*, E_f. I'll leave out a detailed description of the quantity but instead mention it can be written as a monotonically increasing function of concurrence as

$$E_F(\rho) = h\left(\frac{1 + \sqrt{1 - C^2(\rho)}}{2}.\right), \tag{1.78}$$

where $h(x) = -x\log(x) - (1-x)\log(1-x)$ is the binary entropy function from information theory. If you calculate the density matrix of your quantum state in an experiment, concurrence, tangle, and entanglement of formation, to name a few, can be calculated to quantify the entanglement of the system. This brings us to how we experimentally determine the density matrix of a system using quantum state tomography.

1.5 Quantum State Tomography

Systems in quantum mechanics are intrinsically probabilistic, so the same measurement on two identical qubits can result in different outcomes. Projective measurements of a quantum system, such as a polarization qubit passing through a PBS, provide a sample of the statistics describing the possible outcomes associated with the measurement. If the same measurement is performed many times on copies of the same state, the statistics of the measurement can be built up enough to calculate the expected value of that measurement. For a general state, ρ, the expectation value of a single measurement is not sufficient to reconstruct the full density matrix, but collecting expectation values of the system in different bases can begin to build up a more complete picture [56]. This process is called quantum state tomography, and requires a tomographically complete set of measurements which span the operator space of ρ in order to measure sufficient count statistics so that the density matrix can be fully constructed.

First we consider a single qubit density operator. It must be trace one, Hermitian, and positive-semidefinite. These constraints enable the parametrization

$$\rho = \begin{pmatrix} \rho_{11} & \rho_{12} \\ \rho_{21} & \rho_{22} \end{pmatrix} = \begin{pmatrix} \rho_{11} & \rho_{12} \\ \rho_{12}^* & 1-\rho_{11} \end{pmatrix}. \tag{1.79}$$

One example of a tomographically complete set of measurements for a single qubit is $\{H, V, D, R\}$. Starting with H, Born's rule gives the probability of the projective measurement

$$P_H = \mathrm{Tr}(\rho \left|H\right\rangle \left\langle H\right|). \tag{1.80}$$

In a quantum optics lab, we typically produce many photons with equivalent quantum states and measure detector counts (or more colloquially, clicks) to infer the probability of the measurement. Adding up the counts of both measurements in a basis, for example $N_H + N_V = N$, gives the total number of photons, N, and allows us to convert counts to probabilities by division, $P_H = N_H/N$.

Born's rule can be applied to all four measurements, $\{H, V, D, R\}$, to create the system of equations

$$
\begin{aligned}
N_H &= N\rho_{11} \\
N_V &= N(1-\rho_{11}) \\
N_D &= \frac{N}{2}(1+\rho_{12}+\rho_{12}^*) \\
N_R &= \frac{N}{2}(1+i\rho_{12}-i\rho_{12}^*),
\end{aligned}
\tag{1.81}
$$

There are four elements of the density matrix to solve for, and four equations generated by Born's rule. Solving this system of equations gives

$$
\rho = \begin{pmatrix} N_H/N & \frac{N_D}{N} - 1 - i(\frac{N_R}{N} - 1) \\ \frac{N_D}{N} - 1 + i(\frac{N_R}{N} - 1) & 1 - N_H/N \end{pmatrix}. \tag{1.82}
$$

This type of quantum state tomography is called *linear inversion*. Similarly, Born's rule can be used to generate equations for two or more qubits and the linear inversion protocol can reconstruct density matrices of larger quantum systems. In these cases, coincidence counts are considered instead of detector singles.

Linear inversion can lead to unphysical density matrices when the count statistics are noisy. For this reason, maximum likelihood estimation quantum state tomography is a more common method for experimentally determining quantum states [70]. With this approach, a density matrix which is constrained to be physical is randomly generated as an initial guess for an optimization routine. These constraints include normalization, hermiticity, and positivity [71]. To ensure these properties, the density matrix is constrained by

$$
\rho = T^\dagger T / \mathrm{Tr}(T^\dagger T) \tag{1.83}
$$

where T is a square matrix with the same dimensions as ρ. Any matrix that can be written as $T^\dagger T$ must be positive-semi definite as $\langle\psi| T^\dagger T |\psi\rangle = \langle\psi'|\psi'\rangle \geq 0$, taking the adjoint proves Hermiticity as $(T^\dagger T)^\dagger = T^\dagger (T^\dagger)^\dagger = T^\dagger T$, and dividing by $\mathrm{Tr}(T^\dagger T)$ ensures normalization.

The experiments in chapter 3 and chapter 4 implement this method to reconstruct two-qubit density matrices which require 16 tomographically complete measurements for a 16 element density matrix. The maximum likelihood estimation algorithm requires inverting

T to relate its elements to the elements of ρ. It is therefore helpful to represent T as a lower triangular matrix with elements

$$T = \begin{pmatrix} t_1 & 0 & 0 & 0 \\ t_5 + it_6 & t_2 & 0 & 0 \\ t_{11} + it_{12} & t_7 + it_8 & t_3 & \\ t_{15} + it_{16} & t_{13} + it_{14} & t_9 + it_{10} & t_4 \end{pmatrix}. \tag{1.84}$$

A likelihood error function, $\mathcal{L}$, is minimized numerically by searching for the physical density matrix which is most likely to fit the data. The following function is minimized with respect to the density matrix elements,

$$\mathcal{L}(\hat{\rho}) = \sum_{i=1}^{16} \frac{\left[\mathcal{N}\mathrm{Tr}(\hat{\rho}|\psi_i\rangle\langle\psi_i|) - n_i\right]^2}{2\mathcal{N}\mathrm{Tr}(\hat{\rho}|\psi_i\rangle\langle\psi_i|)}, \tag{1.85}$$

where $\hat{\rho}$ is the density matrix which describes the two-photon state and is parameterized by Eq. 1.83 and Eq. 1.84, i is the variable which indexes the 16 different measurements required for a two-qubit density matrix reconstruction, $|\psi_i\rangle\langle\psi_i|$ are the tomographically complete measurement operators, n_i are the raw coincidence counts measured in the experiment, and $\mathcal{N}$ is the total number of counts before the projective measurement. Similar to the one-qubit linear inversion example, $\mathcal{N}$ is inferred from a subset of the measurements using the following relationship

$$\begin{aligned} \mathcal{N} = {} & \mathrm{Tr}(\hat{\rho}|\mathrm{HH}\rangle\langle\mathrm{HH}|) + \mathrm{Tr}(\hat{\rho}|\mathrm{VV}\rangle\langle\mathrm{VV}|) \\ & + \mathrm{Tr}(\hat{\rho}|\mathrm{HV}\rangle\langle\mathrm{HV}|) + \mathrm{Tr}(\hat{\rho}|\mathrm{VH}\rangle\langle\mathrm{VH}|). \end{aligned} \tag{1.86}$$

In contrast to the linear inversion technique, maximum likelihood estimation can be employed on a measurement dataset that is tomographically overcomplete containing more than the minimum number of measurements.

Chapter 2

Nonlinear optics

2.1 Chapter Overview

Nonlinear media are imperative for each experiment in this thesis, from entangled photon generation to ultrafast pulse measurement. Nonlinear optics describes the physics behind phenomena which occur when light modifies the optical properties of material systems, which generally requires intense light fields as in those provided by lasers. I begin by introducing the polarization field generated by an electric field in matter in Sec. 2.2, and discuss the relation between the two fields. Sec. 2.3 derives and discusses the process of second harmonic generation (SHG). Spontaneous parametric downconversion (SPDC) for the generation of entangled photons is described in Sec. 2.4. The optical Kerr effect is presented as a method for measuring ultrafast single photons in Sec. 2.5. I conclude with a discussion on ultrafast optics in Sec 2.6, which provides details on ultrafast pulse propagation in dispersive media.

2.2 Electric Fields in Matter

Nonlinear optical processes discussed in this thesis occur in specifically engineered dielectric materials. These are materials which are poor conductors that can be polarized by an input electric field. Unlike conductors, the electrons in a dielectric may not flow freely through the material. When an electric field is applied, the average position of electrons in the material shifts enough to create a dipole moment between the electron and atomic nucleus. The dipole moments between each of the electrons and their respective nuclei add up to

produce a second electric field which we call the polarization field, $P(t)$. The material response is altered in a perturbative way [4], which means we can describe $P(t)$ as a Taylor expansion of the applied electric field, $E(t)$, given by

$$\begin{aligned} P(t) &= \epsilon_0 \left[\chi^{(1)} E(t) + \chi^{(2)} E^2(t) + \chi^{(3)} E^3(t) + \cdots \right] \\ &= P^{(1)}(t) + P^{(2)}(t) + P^{(3)}(t) + \cdots . \end{aligned} \tag{2.1}$$

where the proportionality constants, $\chi^{(i)}$, are known as the linear, second order, and third order optical susceptibilities, for increasing i, respectively. This representation of the field assumes instantaneous polarization only depends on the instantaneous electric field, which is true if the medium responds instantaneously. The Kramers-Kronig relations can be used to show that this implies the medium is lossless and dispersionless [72, 6]. In general, the susceptibilities are tensors and depend on the frequencies of the electric field, but under the current assumptions we take them to be constants.

In the linear optic regime, the polarization field is simply the first term in Eq. 2.1. The study of nonlinear optics refers to polarization fields which depend nonlinearly on the applied electric field, and as such, the higher order terms in Eq. 2.1 cannot be ignored. Note, at high intensities of around 10^{16}W/cm^2, corresponding to electric field strengths on the order of atomic field strengths, a Taylor series expansion of $E(t)$ does not converge and therefore the polarization field cannot be defined in this way. This regime is referred to as intense-field nonlinear optics [4], and will not be discussed further here [1]. The fields are written as scalars for simplicity, but the full vector representation of the polarization requires tensor representations of the optical susceptibilities for each spatial component of the electric field. It is often convenient to group all higher order terms into one nonlinear polarization term as

$$P(t) = P^{(1)}(t) + P^{\text{NL}}(t). \tag{2.2}$$

The polarization field is introduced into Maxwell's equations presented at the beginning of Sec. 1.2 by rewriting them in terms of $\mathbf{D}$ and $\mathbf{H}$ as a replacement for $\mathbf{E}$ and $\mathbf{B}$, respectively, where $\mathbf{D}$ is the electric displacement field and $\mathbf{H}$ is the magnetic auxiliary field [73]. These substitutions give

$$\boldsymbol{\nabla} \cdot \mathbf{D} = \rho_f \tag{2.3}$$

[1] Some physicists do not consider this regime nonlinear optics at all. When discussing the regime, be sure to clarify "intense-field" nonlinear optics.

$$\boldsymbol{\nabla} \cdot \mathbf{B} = 0 \tag{2.4}$$

$$\boldsymbol{\nabla} \times \mathbf{E} = -\frac{\partial \mathbf{B}}{\partial t} \tag{2.5}$$

$$\boldsymbol{\nabla} \times \mathbf{H} = \mathbf{J}_f + \frac{\partial \mathbf{D}}{\partial t}, \tag{2.6}$$

where ρ_f is the free charge density, the electric displacement field includes the applied electric field and the material polarization field as $\mathbf{D} = \epsilon_0 \mathbf{E} + \mathbf{P}$, $\mathbf{J}_f$ is the free current running through the material, the auxiliary magnetic field includes the applied magnetic field and magnetization, $\mathbf{M}$, as $\mathbf{H} = \frac{1}{\mu_0}\mathbf{B} - \mathbf{M}$, and μ_0 is the permeability of free space. For the purposes of describing crystals in the lab where we encounter nonlinear optic effects, dielectric materials do not have free charges, $\rho_f = 0$, we have no wires around the crystals applying free currents, $\mathbf{J}_f = 0$, and the crystals are non-magnetic, $\mathbf{M} = 0$. Therefore, the effective difference of Maxwell's equations, as we move from free space to mattter, comes from the polarization field, $\mathbf{P}$. We will see in the following sections how the nonlinear components of the polarization field generate new fields with new frequency components.

2.2.1 The Wave Equation in Nonlinear Media

With the previous assumptions on free currents, charges, and magnetization, the forced wave equation will be derived to illustrate how the nonlinear polarization field affects wave propagation through a material. Taking the curl of Eq. 2.5 gives

$$\begin{aligned} \boldsymbol{\nabla} \times \boldsymbol{\nabla} \times \mathbf{E} &= \boldsymbol{\nabla} \times -\frac{\partial \mathbf{B}}{\partial t} \\ &= -\frac{\partial}{\partial t} \left(\boldsymbol{\nabla} \times \mathbf{B} \right) \\ &= -\frac{\partial}{\partial t} \left(\mu_0 \frac{\partial \mathbf{D}}{\partial t} \right) \\ &= -\mu_0 \frac{\partial^2}{\partial t^2} \left(\epsilon_0 \mathbf{E} + \mathbf{P} \right), \end{aligned} \tag{2.7}$$

where we substituted in Eq. 2.6 to get from line two to three. Rearranging and replacing μ_0 by $1/\epsilon_0 c^2$ we get

$$\boldsymbol{\nabla} \times \boldsymbol{\nabla} \times \mathbf{E} + \frac{1}{c^2}\frac{\partial^2}{\partial t^2}\mathbf{E} = -\frac{1}{\epsilon_0 c^2}\frac{\partial^2}{\partial t^2}\mathbf{P}. \tag{2.8}$$

Just as we proceeded in Sec. 1.3.2, we employ the vector calculus identity $\boldsymbol{\nabla} \times \boldsymbol{\nabla} \times \mathbf{A} = \boldsymbol{\nabla}(\boldsymbol{\nabla} \cdot A) - \boldsymbol{\nabla}^2 A$ which gives

$$\boldsymbol{\nabla}(\boldsymbol{\nabla} \cdot \mathbf{E}) - \boldsymbol{\nabla}^2\mathbf{E} + \frac{1}{c^2}\frac{\partial^2}{\partial t^2}\mathbf{E} = -\frac{1}{\epsilon_0 c^2}\frac{\partial^2}{\partial t^2}\mathbf{P}. \tag{2.9}$$

In previous sections, $\boldsymbol{\nabla} \cdot \mathbf{E}$ was set to zero by Maxwell's first equation. We have to be more careful here because Maxwell's first equation is now written in terms of $\mathbf{D}$ and by extension includes $\mathbf{P}$. However, in practice for the frequencies considered in this thesis which are fast relative to the field amplitude envelope, this second derivative term is very small compared to the other terms due to the slowly-varying amplitude approximation explained in Sec. 1.3.2, so we will leave it out and write the wave equation as

$$\boldsymbol{\nabla}^2\mathbf{E} - \frac{1}{c^2}\frac{\partial^2}{\partial t^2}\mathbf{E} = \frac{1}{\epsilon_0 c^2}\frac{\partial^2}{\partial t^2}\mathbf{P}. \tag{2.10}$$

Splitting up the polarization field into its linear and nonlinear components, $\mathbf{P} = \mathbf{P}^{(1)} + \mathbf{P}^{\mathrm{NL}}$, and labeling the linear component of the electric displaced field as $\mathbf{D}^{(1)} = \epsilon_0\mathbf{E} + \mathbf{P}^{(1)}$, we can rewrite the wave equation as

$$\boldsymbol{\nabla}^2\mathbf{E} - \frac{1}{\epsilon_0 c^2}\frac{\partial^2}{\partial t^2}\mathbf{D}^{(1)} = \frac{1}{\epsilon_0 c^2}\frac{\partial^2}{\partial t^2}\mathbf{P}^{\mathrm{NL}}. \tag{2.11}$$

This equation is simpler to interpret with an example. Suppose the nonlinear medium is lossless, dispersionless, and isotropic. The linear electric displacement field is simplified to $\mathbf{D}^{(1)} = \epsilon_0\epsilon^{(1)}\mathbf{E}$, where $\epsilon^{(1)}$ is a permittivity constant which is specific to the dielectric material. The wave equation in this example simplifies to

$$-\boldsymbol{\nabla}^2\mathbf{E} + \frac{\epsilon^{(1)}}{c^2}\frac{\partial^2}{\partial t^2}\mathbf{E} = -\frac{1}{\epsilon_0 c^2}\frac{\partial^2}{\partial t^2}\mathbf{P}^{\mathrm{NL}}. \tag{2.12}$$

Now that the E-field is in both the spatial and temporal second derivatives, this equation has the form of a driven wave equation where the nonlinear polarization acts as a source term [4]. This is called a source term because it can generate new waves with different

frequencies, which will be the key to the nonlinear optical effects discussed in the coming sections and used throughout the experiments in the thesis. If you take away the source term, the equation describes free waves propagating with velocity $c/\sqrt{\epsilon^{(1)}}$ with the same frequency as the applied electric field $\mathbf{E}$. So far, I've assumed the electric field is monochromatic, but a driven wave equation can be given for each frequency component, n, as

$$-\boldsymbol{\nabla}^2\mathbf{E}_n + \frac{\epsilon^{(1)}(\omega_n)}{c^2}\frac{\partial^2}{\partial t^2}\mathbf{E}_n = -\frac{1}{\epsilon_0 c^2}\frac{\partial^2}{\partial t^2}\mathbf{P}_n^{\mathrm{NL}}, \tag{2.13}$$

where the permittivity, $\epsilon^{(1)}(\omega_n)$, is now a function of frequency.

2.3 Second Harmonic Generation

The field of nonlinear optics is said to have begun with the first demonstration of second harmonic generation (SHG). In 1961, only one year after the laser was invented, Franken et al. [74] detected light with twice the energy of the input optical ruby maser after propagation through a crystalline quartz sample. This effect is due to the $\chi^{(2)}$ term of the nonlinear polarization and will be derived below. The electric field of the laser can be written as

$$E(t) = Ee^{-i\omega t} + E^* e^{i\omega t}. \tag{2.14}$$

SHG requires a material with a nonzero second-order susceptibility, $\chi^{(2)}$, for which you need a material that is non-centrosymmetric. The nonlinear $P^{(2)}(t)$ term is nonzero and expressed as

$$\begin{aligned} P^{(2)}(t) &= \epsilon_0\chi^{(2)}E^2(t) \\ &= \epsilon_0\chi^{(2)}E(t)E(t)^* \\ &= 2\epsilon_0\chi^{(2)}EE^* + \epsilon_0\chi^{(2)}E^2e^{-i2\omega t} + \epsilon_0\chi^{(2)}(E^*)^2e^{i2\omega t}. \end{aligned} \tag{2.15}$$

Consider this equation as the source term for the driven wave equation in Eq. 2.12. The second time derivative will kill the first term, but when applied to the the second and third terms it will lead to the generation of new electromagnetic modes with frequency 2ω.

These modes are called the second harmonic of E. Energy conservation must hold, so the absorption of two input photons results in the emission of a single photon with twice the energy. SHG is thereby classified as a three-wave mixing processes where the two input waves have equal frequency. We number the modes involved in this process as E_1 and E_2 which must satisfy the driven wave equation and so can be represented as

$$E_1(z,t) = A_1 e^{i(k_1 z - \omega_1 t)} + A_1^* e^{-i(k_1 z - \omega_1 t)} \tag{2.16}$$

$$E_2(z,t) = A_2 e^{i(k_2 z - \omega_2 t)} + A_2^* e^{-i(k_2 z - \omega_2 t)} \tag{2.17}$$

where ω_i and k_i are the frequency and wave number of mode i, respectively. Energy conservation mandates $\omega_2 = 2\omega_1$, and k_i is given by

$$k_i = \frac{n_i \omega_i}{c} \tag{2.18}$$

where $n_i = \sqrt{\epsilon^{(1)}(\omega_i)}$. Both of the modes have a corresponding polarization field,

$$P_1(z,t) = B_1(z) e^{-i\omega_1 t} + B_1^*(z) e^{i\omega_1 t} \tag{2.19}$$

$$P_2(z,t) = B_2(z) e^{-i\omega_2 t} + B_2^*(z) e^{i\omega_2 t} \tag{2.20}$$

and must independently obey the driven wave equation,

$$\frac{\partial^2}{\partial z^2} E_j(z,t) - \frac{\epsilon^{(1)}(\omega_j)}{c^2} \frac{\partial^2}{\partial t^2} E_j(z,t) = \frac{1}{\epsilon_0 c^2} \frac{\partial^2}{\partial t^2} P_j(z,t) \qquad (j = 1, 2), \tag{2.21}$$

where $\boldsymbol{\nabla}^2$ has been simplified to $\frac{\partial^2}{\partial z^2}$ as we are considering fields that only depend on a longitudinal coordinate z. The amplitudes for the polarization fields are written as

$$B_1(z) = 2\epsilon_0 \chi^{(2)} A_2 A_1^* e^{i(k_2 - k_1)z} \tag{2.22}$$

$$B_2(z) = \epsilon_0 \chi^{(2)} A_1^2 e^{2ik_1 z}. \tag{2.23}$$

After substitution of electric and polarization fields into Eq. 2.21, we get the following coupled-amplitude equations

$$\frac{dA_1}{dz} = \frac{i\omega_1^2\chi^{(2)}}{k_1c^2}A_2A_1^*e^{-i(2k_1-k_2)z} \tag{2.24}$$

$$\frac{dA_2}{dz} = \frac{i\omega_2^2\chi^{(2)}}{2k_2c^2}A_1^2e^{i(2k_1-k_2)z}. \tag{2.25}$$

where the differential equations have been simplified by employing the slowly-varying amplitude approximation introduced in Eq. 1.36 to each A_j to neglect second derivatives as,

$$\left|\frac{d^2A_j}{dz^2}\right| \ll \left|k_j\frac{dA_j}{dz}\right|. \tag{2.26}$$

These coupled differential equations describe the propagation of input beam and second harmonic field amplitudes through the crystal and illustrate how the second harmonic is generated in the crystal as a consequence of the nonlinear polarization field $P^{\mathrm{NL}}(z,t) = P^{(2)}(z,t)$. The undepleted-pump approximation assumes that A_1 is constant and enables a direct integration of Eq. 2.25 to see how the second harmonic field generates and progresses through the crystal. As more of the pump field is converted into the second harmonic field, this approximation is no longer accurate and the two coupled equations must be solved simultaneously. In the undepleted-pump regime of a crystal with length L,

$$\begin{aligned}\int_0^L dA_2 &= \frac{i\omega_2^2\chi^{(2)}A_1^2}{2k_2c^2}\int_0^L dze^{i(2k_1-k_2)z} \\ A_2(L) &= \frac{i\omega_2^2\chi^{(2)}A_1^2}{2k_2c^2}\left(\frac{e^{i\Delta kL}-1}{i\Delta k}\right)^2\end{aligned} \tag{2.27}$$

where $\Delta k = 2k_1 - k_2$ is the SHG wavevector mismatch. The intensity of the second harmonic field is obtained by the time-averaged Poynting vector, $I_2 = 2n(\omega_2)\epsilon_0c|A_2|^2$, giving

$$
\begin{aligned}
I_2 &= \frac{n(\omega_2)\epsilon_0\omega_2^4(\chi^{(2)})^2|A_1|^4}{2k_2^2c^3}\left|\frac{e^{i\Delta kL}-1}{i\Delta k}\right|^2 \\
&= \frac{n(\omega_2)\epsilon_0\omega_2^4(\chi^{(2)})^2|A_1|^4}{2k_2^2c^3}L^2\mathrm{sinc}^2(\Delta kL/2) \\
&== \frac{\omega_2^2(\chi^{(2)})^2I_1^2}{8c^3\epsilon_0 n(\omega_2)n^2(\omega_1)}L^2\mathrm{sinc}^2(\Delta kL/2),
\end{aligned}
\tag{2.28}
$$

where sinc $= \sin(x)/x$, and constants have been simplified using $k_j = \omega_j n(\omega_j)/c$. By tuning the wave vector mismatch parameter, I_2 can be maximized. This process is called phase-matching and will be discussed in more detail in the following section. In general, nonlinear optical phenomena involving modes with different frequencies have a wave vector mismatch parameter which changes depending on the number of fields involved and the type of nonlinear optical phenomenon, but the concept of phase-matching is universal to all of these processes.

Here, we focused on the second harmonic of a laser. This is the only harmonic used in experiments in this thesis, but for interested readers, it should be noted that higher harmonics are also studied. In crystals with strong $\chi^{(3)}$ or $\chi^{(4)}$ susceptibility components, third harmonic generation (THG) and fourth harmonic generation (FHG) respectively, is possible. Note, FHG can also be effectively accomplished with two cascaded SHG crystals, and thus even higher frequency modes are theoretically accessible using multiple stages of SHG and THG. High harmonic generation (HHG) refers to the fifth harmonic and above, and in practice utilizes other strategies such as working with a rare gas medium and high intensity lasers [75].

SHG has seen many different applications including microscopy [76], characterization of crystalline materials [77], and ultrashort pulse measurement [78, 79]. Many researchers employ SHG to produce light with a higher frequency than their laser can generate, or when multiple frequencies are needed on a table with only one laser. Crystals can be purchased and mounted for free-space optics, and prealigned fiber-integrated SHG modules are available for fiber optic applications. Interestingly, many sub-research grade green laser pointers available to the public are actually IR laser pointers with an inefficient SHG crystal embedded. You can't see the IR frequency with your eyes, but it is often the dominant intensity.

2.3.1 Phase-matching

We have seen that the intensity of the second harmonic field in the previous section depends on the length of the crystal and the wavevector mismatch as $\text{sinc}^2(\Delta kL/2)$. This function is presented in Fig. 2.1 and decreases as $|\Delta k|L$ increases. This efficiency drop occurs when the second harmonic field falls out of phase with the input laser field. Both fields are in a medium with an index of refraction which varies with light frequency. As soon as higher frequency second harmonic light is generated, it travels through the medium with a different speed than the input light field and the longer the crystal, the more out of phase the two fields become. Once out of phase, newly generated second harmonic light will destructively interfere with previously generated second harmonic light. The goal of phase-matching is to keep the input and SHG fields in phase with each other such that newly generated light fields will constructively interfere with previously generated light fields and boost the second harmonic intensity.

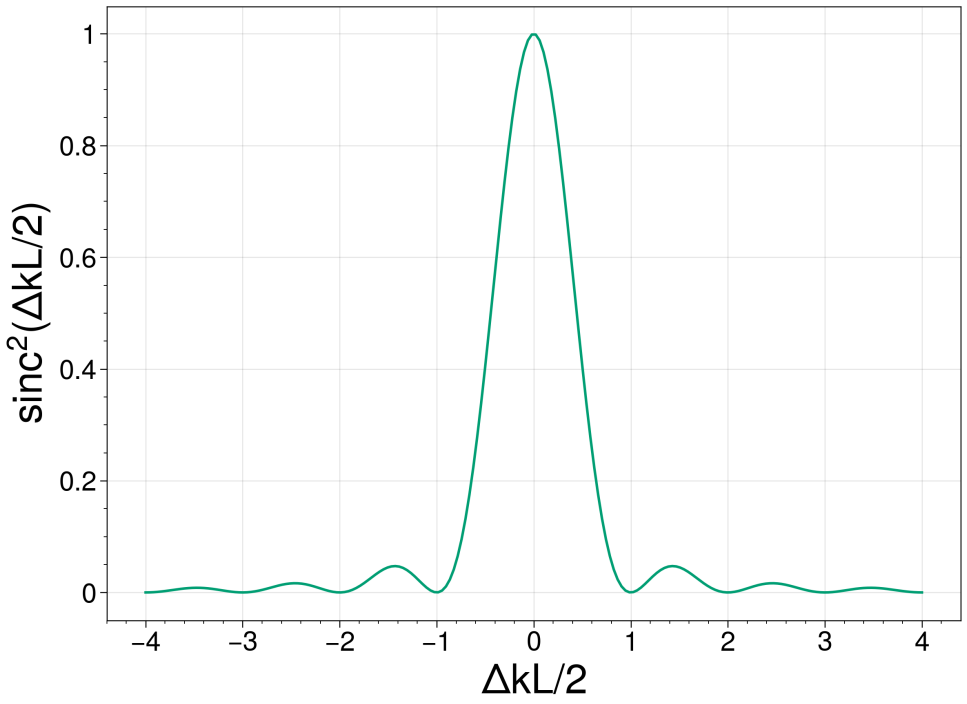

Figure 2.1: Visualization of relationship between SHG efficiency and wavevector mismatch.

Perfect phase-matching occurs when $\Delta k = 0$. In practice, this comes down to tuning the index of refraction of the material as

$$\begin{aligned} \Delta k &= 0 \\ 2k_1 &= k_2 \\ \frac{2n(\omega_1)\omega_1}{c} &= \frac{n(\omega_2)\omega_2}{c} \\ n(\omega_1) &= n(2\omega_1), \end{aligned} \tag{2.29}$$

where $\omega_2 = 2\omega_1$. The difficulty of phase-matching arises from the fact that the index of refraction of most materials exhibits normal dispersion. Visualized in Fig. 2.2, normal dispersion results in an index of refraction which monotonically decreases with increasing wavelength.

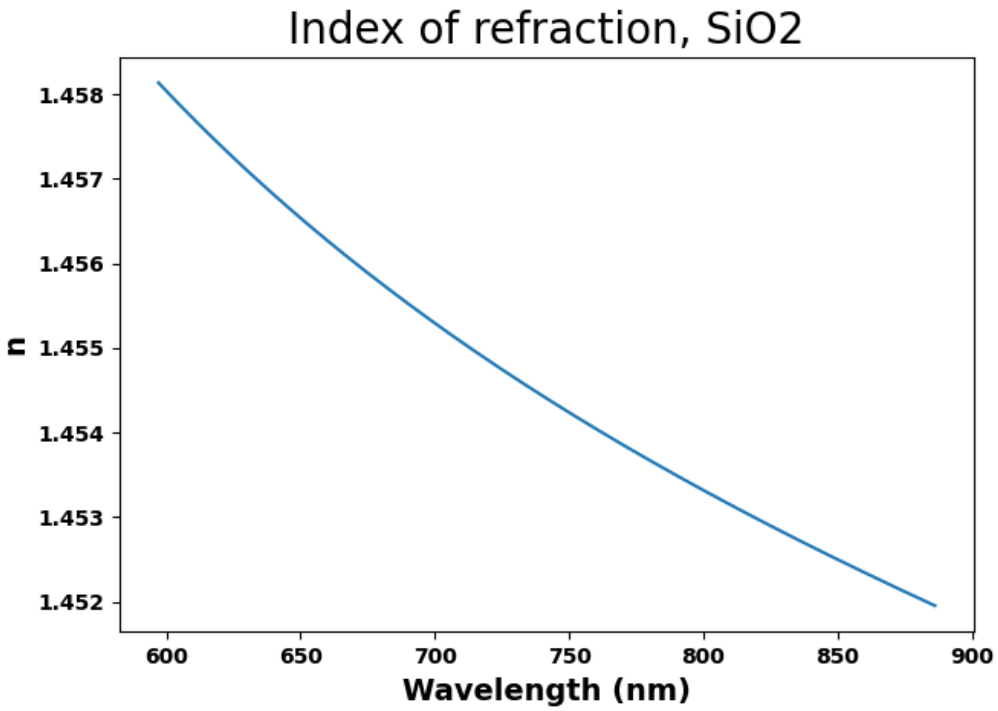

Figure 2.2: Index of refraction in silica as a function of wavelength.

To circumvent this, a common phase-matching technique takes advantage of birefringence. If the input light has a different polarization than the second harmonic light, then the two fields "see" a different index of refraction in a birefringent material.

The relative index of refraction difference between the two fields must be tuned in order to satisfy $n(\omega_1) = n(2\omega_1)$. This is done in two ways: Temperature tuning and angle tuning. The index of refraction is a function of crystal temperature, and in many birefringent materials the birefringence also depends on temperature. Nonlinear crystals can be heated to a particular temperature in an oven with a window for input and output beams. Angle tuning involves changing the angle between the incoming light and and optic axis of the crystal in order to tune the relative birefringence experienced by the two fields. This technique is limited because large angles between the surface of the crystal and the incoming light will lead to spatial walk-off between the two fields. However, when combined with temperature tuning, a Goldilocks angle/temperature combination can lead to perfect phase-matching without large angle changes. In some cases, angle tuning is sufficient for high efficiency nonlinear optical processes. Crystals are pre-cut to ensure the incidence angle is very close to the perfect phase-matching angle to avoid large incidence angles and spatial walk-off.

2.3.2 Non-centrosymmetric Media

Earlier it was stated that as a $\chi^{(2)}$ process, SHG requires non-centrosymmetric materials, that is, materials that do not possess inversion symmetry. Below, SHG is used as an example of $\chi^{(2)}$ vanishing in centrosymmetric media to provide more intuition between the relationship between $\chi^{(2)}$ and crystal symmetry as shown in Ref [4].

We have shown that the nonlinear polarization is related to the incident electric field as

$$P^{(2)}(t) = \epsilon_0 \chi^{(2)} E^2(t). \tag{2.30}$$

Assume the applied field is given by

$$E(t) = A\cos\omega t. \tag{2.31}$$

Now, if we take an identical applied field with the opposite sign, we expect the polarization field to change as well because the medium is symmetric under spatial inversion. This would change Eq. 2.30 to

$$-P^{(2)}(t) = \epsilon_0 \chi^{(2)}[-E(t)]^2, \tag{2.32}$$

which simplifies to

$$-P^{(2)}(t) = \epsilon_0 \chi^{(2)} E^2(t). \tag{2.33}$$

Comparing this to Eq. 2.30, it follows that both statements can only be true if $P^{(2)}(t) = 0$, implying that $\chi^{(2)} = 0$.

2.4 Spontaneous Parametric Downconversion

Spontaneous parametric down-conversion (SPDC) is another three-wave mixing process which occurs in a $\chi^{(2)}$ medium. In contrast to SHG, the input field is higher in frequency and a photon "down-converts" into two lower frequency photons. This process is how all entangled photon pairs are created in the experiments in this thesis, and for historical reasons, we refer to the high-frequency parent photon as the "pump" and the two entangled daughter photons as the "signal" and "idler". The signal and idler photons need not be equal in energy, but energy conservation must hold giving $\omega_p = \omega_s + \omega_i$. This phenomenon was first observed in 1967 by Harris et al. [80] by pumping a lithium niobate ($LiNbO_3$) crystal with a 488 nm argon laser. They observed that spontaneous fluorescence was tunable from 540 nm to 660 nm by temperature phase-matching the crystal.

Three years later in 1970, Burnham and Weinberg [81] demonstrated SPDC in an ammonium dihydrogen phosphate crystal by pumping with a 324 nm He-Cd laser. This experiment is particularly important in the history of quantum optics because they recorded single photon pair coincidence-counts. When they moved one of the two photo-multiplier detectors in either the horizontal or vertical direction, changed the spectral filters, or altered the relative delay time between the two paths, the coincidence rates would drop down to the expected accidental rates. This demonstrated that energy conservation and momentum conservation of photon pairs both had to be satisfied in order to detect pair-coincidences. This groundbreaking experiment laid the foundation for SPDC to become the workhorse of future quantum optics experiments. Other single photon generation methods are employed today such as quantum dots [82], single atom systems [83], and nitrogen-vacancy centres in diamond [84], to name a few. While they each have their advantages, SPDC remains the most commonly used in academia and industry for quantum information and

communication experiments, with a plethora of applications across quantum cryptography, quantum metrology, quantum simulation, and exploring the foundations of quantum mechanics [85, 86].

Similar to the derivation of the SHG coupled differential equations, the amplitudes of the fields in a three wave mixing process are described by coupled differential equations given by

$$\begin{aligned}
\frac{dA_1}{dz} &= \frac{i\chi^{(2)}\omega_1^2}{k_1 c^2} A_3 A_2^* e^{-i\Delta k z} \\
\frac{dA_2}{dz} &= \frac{i\chi^{(2)}\omega_2^2}{k_2 c^2} A_3 A_1^* e^{-i\Delta k z} \\
\frac{dA_3}{dz} &= \frac{i\chi^{(2)}\omega_3^2}{k_3 c^2} A_1 A_2 e^{i\Delta k z},
\end{aligned} \tag{2.34}$$

where $\Delta k = k_1 + k_2 - k_3$ is the wave vector mismatch, and $\omega_3 = \omega_1 + \omega_2$. SPDC starts with a strong $A_3(t = 0)$ field coming from the laser and no photons in the other two modes, $A_1(t = 0) = A_2(t = 0) = 0$. Note, these initial conditions set all three coupled differential equations to zero. So, classically this process cannot be sparked by just the A_3 field. A quantum mechanical description of the fields and the vacuum of unpopulated modes allows for spontaneous production of signal and idler photons [87]. SPDC has been wonderfully described quantum mechanically by many past group members. Interested readers are strongly recommended to check out similar descriptions to what is presented below in references [88, 89].

2.4.1 SPDC in the Discrete Picture

To begin, we assume the pump is in an initial single-mode coherent state and the signal and idler are in the vacuum state. We also assume, as we did in the SHG derivation, that there is only a single component to the $\chi^{(2)}$ tensor and it can be treated as a scalar. The Hamiltonian describing this system will be broken into two terms, the free Hamiltonian in the media, $\hat{H}_0$, and the nonlinear interaction term, $\hat{H}^{NL}$, as

$$\hat{H} = \hat{H}_0 + \hat{H}^{NL}. \tag{2.35}$$

The nonlinear interaction term in the Hamiltonian couples the three fields together and is given by the normal-ordered energy conserving terms as

$$\hat{H}^{NL} = -\frac{\epsilon_0}{3}\chi^{(2)}\int_V dV\,\hat{E}_s^{(-)}\hat{E}_i^{(-)}\hat{E}_p^{(+)} + \hat{E}_p^{(-)}\hat{E}_s^{(+)}\hat{E}_i^{(+)}, \tag{2.36}$$

where $\hat{E}^{(+)}$ and $\hat{E}^{(-)}$ are previously defined in Eq. 1.12. Time evolution of our state is given by

$$|\psi\rangle = e^{-i\hat{H}^{NL}t/\hbar}\,|0\rangle_s\,|0\rangle_i\,|\alpha\rangle_p\,, \tag{2.37}$$

which to first order is expanded to

$$\begin{aligned}|\psi\rangle = |0\rangle_s\,|0\rangle_i\,|\alpha\rangle_p + \frac{it\epsilon_0\chi^{(2)}}{3\hbar}\int_0^t dt'\int_V dV\,\hat{E}_s^{(-)}\hat{E}_i^{(-)}\hat{E}_p^{(+)}\,|0\rangle_s\,|0\rangle_i\,|\alpha\rangle_p \\ + \frac{it\epsilon_0\chi^{(2)}}{3\hbar}\int_0^t dt'\int_V dV\,\hat{E}_p^{(-)}\hat{E}_s^{(+)}\hat{E}_i^{(+)}\,|0\rangle_s\,|0\rangle_i\,|\alpha\rangle_p\,.\end{aligned} \tag{2.38}$$

The second term in the state describes the process of SPDC where a pump photon is annihilated and a signal and idler photon are created. Recall that the $\hat{E}^{(+)}$ and $\hat{E}^{(-)}$ rather unintuitively correspond to destruction and creation ladder operators, respectively. The third term describes the reverse process, sum-frequency generation (SFG), where the signal and idler photons are detroyed to create a pump photon. SHG is the special case of SFG where both input photons are the same frequency.

Focusing on the second term which we now label as $|\psi\rangle_{\text{spdc}}$, and dropping the constant coefficient, we substitute in Eq. 1.12 to get

$$|\psi\rangle_{\text{spdc}} \propto \sum_{\mathbf{k}_s\mathbf{k}_i}\int_0^t dt'\int_V dV\,\alpha a^\dagger_{\mathbf{k}_s}a^\dagger_{\mathbf{k}_i}e^{i(\omega_s+\omega_i-\omega_p)t'}e^{i(\mathbf{k}_s+\mathbf{k}_i-\mathbf{k}_p)\cdot\mathbf{r}}\,|0\rangle_s\,|0\rangle_i\,|\alpha\rangle_p\,, \tag{2.39}$$

where the mathematical definition of a coherent state $\hat{a}_{\mathbf{k}_p}\,|\alpha\rangle = \alpha\,|\alpha\rangle$ and the fact that the pump is in a single spatial mode was used to simplify the expression. Carrying out the time integral over long integration times yields

$$\lim_{t\to\infty}\int_0^t dt' e^{i(\omega_s+\omega_i-\omega_p)t'} = 2\pi\delta(\omega_s+\omega_i-\omega_p), \tag{2.40}$$

where we can see energy conservation and note that fixing the pump frequency constrains the sum $\omega_s + \omega_i$. The bandwidth of each photon is not constrained individually, however, energy conservation leads to anti-correlated frequencies. The higher the signal frequency is, the lower the idler frequency must be, and vice-versa. The energy level diagram of this system is displayed in Fig. 2.3.

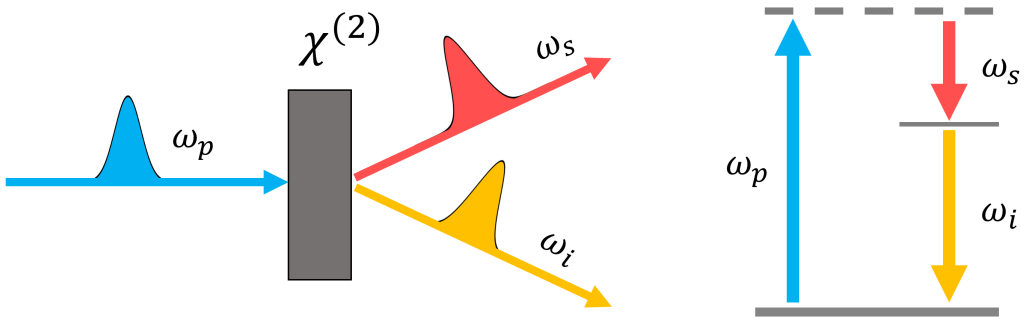

Figure 2.3: Energy level diagram for spontaneous parametric downconversion. A high frequency pump field, ω_p, is incident on a $\chi^{(2)}$-nonlinear crystal and downconverted to lower frequency signal, ω_s, and idler, ω_i, fields.

Assuming a crystal with physical dimensions L_x,L_y, and L_z, we can write the volume integral as

$$\int_V dV e^{-i(\mathbf{k}_s+\mathbf{k}_i-\mathbf{k}_p)\cdot r} = \int_0^{L_x} dx e^{-i\Delta k_x x} \int_0^{L_y} dy e^{-i\Delta k_y y} \int_0^{L_z} dz e^{-i\Delta k_z z} \tag{2.41}$$

where $\Delta k_j = k_{s,j} + k_{i,j} - k_{p,j}$ for $j = (x, y, z)$. Each of these integrals can be solved as

$$\int_0^{L_x} dx e^{-i\Delta k_x x} = e^{\frac{-i\Delta k_x L_x}{2}} L_x \text{sinc}\left(\frac{\Delta k_x L_x}{2}\right) \tag{2.42}$$

Resulting in a $\text{sinc}(\Delta k_j L_j/2)$ function for each direction. Similar to our classical approach to phase-matching in SHG, we see an optimal phase-matching region near $\Delta k_z L_z/2 = 0$.

2.4.2 SPDC in the Continuum Picture

So far we have been analyzing the Hamiltonian in terms of ladder operators defined for discrete wave vectors by using the discrete definition of the $E^{(+)}$ and $E^{(-)}$ terms derived in Eq. 1.12 by assuming the field is quantized in a cavity. We can also learn from an analysis in the continuum picture using the definitions from Eq. 1.13 instead. In this picture, the Hamiltonian is written as

$$\begin{aligned}\hat{H}^{NL} = &-\frac{\epsilon}{3}\chi^{(2)}\left(\frac{\hbar}{4\pi\epsilon_0 cA}\right)^{\frac{3}{2}}\int_0^{L_z} dz\left(\int d\omega_s \frac{\sqrt{\omega_s}}{n(\omega_s)}a_s^\dagger(\omega_s)e^{-i(\omega_s t-k_s z)}\right)\\ &\times\left(\int d\omega_i \frac{\sqrt{\omega_i}}{n(\omega_i)}a_i^\dagger(\omega_i)e^{-i(\omega_i t-k_i z)}\right)\\ &\times\left(\int d\omega_p \frac{\sqrt{\omega_p}}{n(\omega_p)}a_p(\omega_p)e^{i(\omega_p t-k_p z)}\right)+h.c.\end{aligned} \tag{2.43}$$

where $h.c.$ implies Hermitian conjugate to avoid writing out the other three integrals describing three-wave mixing. Although each free wave was originally defined out to $L\to\infty$ in the z direction, the interaction Hamiltonian only describes waves inside the crystal of length L_z. An integral along the z-axis will once again provide phase-matching information as

$$\frac{1}{L_z}\int_0^{L_z} dz e^{i(k_p-k_s-k_i)z} = e^{\frac{i\Delta kL_z}{2}}\text{sinc}\left(\frac{\Delta kL_z}{2}\right), \tag{2.44}$$

where the phase mismatch, $\Delta k = k_p - k_s - k_i$, is along the z-axis. This term is given the name phase-matching function, denoted

$$\Phi(\omega_s,\omega_i,\omega_p) = e^{\frac{i\Delta kL_z}{2}}\text{sinc}\left(\frac{\Delta kL_z}{2}\right), \tag{2.45}$$

where frequency dependence stems from the dependence of k_j on ω_j, as $k_j = \frac{n(\omega_j)\omega_j}{c}$. As done in Sec. 2.4.1, time evolution of this Hamiltonian to first order gives

$$
\begin{aligned}
|\psi\rangle_{spdc} &\propto \int d\omega_s d\omega_i d\omega_p \alpha(\omega_p)\Phi(\omega_s,\omega_i,\omega_p)\left(2\pi\delta(\omega_s+\omega_i-\omega_p)\right) a_s^\dagger(\omega_s)a_i^\dagger(\omega_i)\,|0\rangle_s\,|0\rangle_i\,|\alpha\rangle_p \\
&\propto \int d\omega_s d\omega_i \alpha(\omega_s+\omega_i)\Phi(\omega_s,\omega_i,\omega_s+\omega_i) a_s^\dagger(\omega_s)a_i^\dagger(\omega_i)\,|0\rangle_s\,|0\rangle_i\,,
\end{aligned}
\tag{2.46}
$$

where the delta function removes all reference to pump frequency ω_p so we drop the coherent state $|\alpha\rangle$ from the description.

This representation of the SPDC state can be thought of as a distribution of photon pairs with frequencies ω_s and ω_i weighted by the pump amplitude $\alpha(\omega_s+\omega_i)$ and phase-matching function $\Phi(\omega_s,\omega_i,\omega_s+\omega_i)$. Depending on these weighting functions, some joint-frequency probabilities will be larger than others. The pump amplitude is a function of the incoming laser only, while the phase-matching function is unique to the nonlinear medium. Note, ω_s does not necessarily need to be equivalent to ω_i, but can be depending on pump amplitude and phase-matching. The $\omega_s = \omega_i$ case is called degenerate SPDC, and the $\omega_s \neq \omega_i$ case is called nondegenerate SPDC.

2.4.3 Phase-matching

Just as in SHG, birefringent materials can be used to ensure the pump photons and SPDC produced photons "see" a different refractive index. A β-barium borate (BBO) crystal is used to produce photons in chapter 5 and is an example of a negative uniaxial crystal where the extraordinary wave travels faster than the ordinary wave ($n_e < n_o$). Ordinary waves have a polarization parallel to the optic axis, while light waves which travel in the same direction as ordinary waves but with orthogonal polarization are extraordinary waves. They get their name from the fact that they do not obey Snell's law of refraction (which is extraordinary, I suppose) while ordinary waves do obey Snell's law. When an e-polarized pump photon downconverts to two o-polarized photons, its called type-I SPDC. If instead, an e-polarized pump photon downconverts to one e-polarized photon and one o-polarized photon, its called type-II SPDC. When type-I SPDC is employed, the photons can not be separated by polarization. In this case, noncollinear SPDC or nondegenerate SPDC can be implemented to separate the photons spatially or spectrally, respectively. In comparison, type-II SPDC can be collinear and degenerate because the photons can be separated by polarization optics such as a PBS.

BBO crystals can be phasematched by angle tuning the crystal to change the effective extraordinary index of refraction [90], $n_e(\theta)$, given by

$$\frac{1}{n_e(\theta)^2} = \frac{\sin^2\theta}{\bar{n}_e^2} + \frac{\cos^2\theta}{n_o^2}, \tag{2.47}$$

where $\bar{n}_e$ is the principal value of the refractive index along the extraordinary axis, and n_o is the refractive index along the ordinary axis. The orientation of the crystal, θ, can be tuned to match the phase-matching condition $\Delta k = 0$.

2.4.4 Quasi-phase-matching

Phase matching discussed so far relies on birefringence to compensate for the relative chromatic dispersion between the pump wavelength and SPDC-photon wavelengths. In some materials, birefringence is not strong enough to compensate for chromatic dispersion. Even when it is, birefringence can be insufficient to compensate for dispersion when the pump has a short wavelength because the refractive index of a material usually increases more rapidly at shorter wavelengths.

Quasi-phase-matching is an alternative strategy to combat dispersion in a material which involves fabricating periodically poled materials. These are crystals with alternating crystal structure that is periodic in space and where the crystalline axes are inverted in each succeeding segment. The inverted crystalline axes lead to an inversion of the nonlinear coupling coefficient, d_{eff} [4].

We represent $d(z)$ as a square-wave function

$$d(z) = d_{\text{eff}}\text{sign}(\cos(2\pi z/\Lambda)), \tag{2.48}$$

where Λ is the poling period, d_{eff} is the magnitude of nonlinear coupling coefficient, z is the propagation distance, and $d(z)$ is related to $\chi^{(2)}$ by $d(z) = \frac{1}{2}\chi^{(2)}$. In terms of its spatial Fourier series, $d(z)$ is represented by

$$d(z) = d_{\text{eff}} \sum_{m=-\infty}^{\infty} G_m e^{ik_m z}, \tag{2.49}$$

where $k_m = (2\pi m/\Lambda)$ is the grating vector of the mth Fourier component, and Fourier coefficients are given by

$$G_m = (2/m\pi)\sin(m\pi/2). \tag{2.50}$$

Taking $m = 1$ gives $G_1 = 2/\pi$. Coupled amplitude equations presented in Eq. 2.34 are now influenced by the spatially varying nonlinear coupling coefficient and written as

$$\begin{aligned}
\frac{dA_1}{dz} &= \frac{2id_Q\omega_1^2}{k_1c^2}A_3A_2^*e^{-i(\Delta k_Q - 2k_m)z} \\
\frac{dA_2}{dz} &= \frac{2id_Q\omega_2^2}{k_2c^2}A_3A_1^*e^{-i(\Delta k_Q - 2k_m)z} \\
\frac{dA_3}{dz} &= \frac{2id_Q\omega_3^2}{k_3c^2}A_1A_2e^{i(\Delta k_Q)z},
\end{aligned} \tag{2.51}$$

where $d_Q = d_{\text{eff}}G_m$, and the new wave vector mismatch parameter is

$$\Delta k_Q = k_1 + k_2 - k_3 + k_m. \tag{2.52}$$

d_Q decreases for higher values of m, and to a good approximation quasi-phase-matching can be modeled for $m = 1$. This leads to a mismatch factor of

$$\Delta k_Q = k_1 + k_2 - k_3 - 2\pi/\Lambda, \tag{2.53}$$

and a nonlinear coupling coefficient of $d_Q = (2/\pi)d_{\text{eff}}$. Traditionally, quasi-phase matching is done with perfectly periodic poling where the distance between changing nonlinear coupling coefficients is constant. However, recent work has shown more effective phase matching techniques are possible with aperiodic poling involving crystals which are manufactured with numerically optimized pole spacing [91]. More complicated crystal domain engineering involves changing the magnitude of the nonlinear coupling coefficient between neighbouring pole sites, as well as building sections shorter than the coherence length of light to maximize SPDC efficiency and shape the phase-matching function [92].

The experiments described in chapters 3 and 4 use a single photon source where type-II quasi-phase-matching is used to produce single photons in a periodically-poled potassium titanyl phosphate (ppKTP) crystal. Periodic poling is often achieved in other common nonlinear optic materials such as lithium niobate (ppLN) and lithium tantalate (ppLT).

2.4.5 Spectral and Temporal Correlations in SPDC

When considered together, the weighting terms $\Phi(\omega_s, \omega_i, \omega_s+\omega_i)$ and $\alpha(\omega_s+\omega_i)$ introduced in Sec. 2.4.2 are referred to as the joint spectral amplitude (JSA),

$$F(\omega_s, \omega_i) = \alpha(\omega_s + \omega_i)\Phi(\omega_s, \omega_i, \omega_s + \omega_i). \tag{2.54}$$

The JSA is a probability distribution that determines the spectral correlations of the two-photon state. If it is factorable into spectral functions that describe each photon individually, such as $F(\omega_s, \omega_i) = F(\omega_s)F(\omega_i)$, then we say the state is separable because a separable JSA implies a separable wavefunction. If this is not the case, the distribution describes energy-time entangled photons.

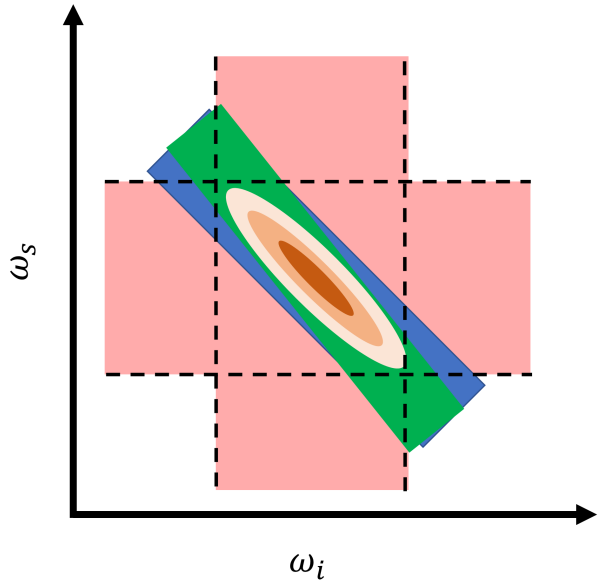

Figure 2.4: Illustration of the joint spectral amplitude (JSA) resulting from SPDC with spectral filters placed in each photon path. The blue rectangle represents the pump amplitude $\alpha(\omega_s, \omega_i)$, the green rectangle represents the phase-matching function, $\Phi(\omega_s, \omega_i, \omega_s + \omega_i)$, and the two larger pink rectangles represent spectral filters $S_s(\omega_s)$ (horizontal), and $S_i(\omega_i)$ (vertical). The spectrally filtered JSA is shown in orange where all four rectangles overlap.

Often, the side-lobes of the $\mathrm{sinc}(\Delta kL/2)$ part of the phase-matching function are undesirable and limit the purity, $P = \mathrm{Tr}(\rho^2)$, of produced photons [93]. This functional-form of the JSA can be avoided by domain engineering $\chi^{(2)}$-nonlinear crystals to have sections of varying nonlinearity smaller than the coherence length of the laser, which are built in to the crystal in the fabrication stage [92]. In contrast, our lab apodizes the side-lobes of the phase-matching function by placing spectral bandpass filters, $S_s(\omega_s)$ and $S_i(\omega_i)$,in each downconverted photon path. The effect of these filters yields the state

$$|\psi\rangle_{spdc} \propto \int d\omega_s d\omega_i F(\omega_s, \omega_i) S_s(\omega_s) S_i(\omega_i) a_s^\dagger(\omega_s) a_i^\dagger(\omega_i) \, |0\rangle_s \, |0\rangle_i \,, \tag{2.55}$$

which is visually represented in Fig. 2.4. In the experiments in this thesis, each filter function is realized with angle-tuned long- and short-pass spectral filters, allowing the bandwidth to be specifically chosen to filter out the side-lobes without filtering the main phase-matching peak. This provides the additional advantage of filtering out the remaining pump light, but comes with the caveat that the brightness of the single photon source is lowered.

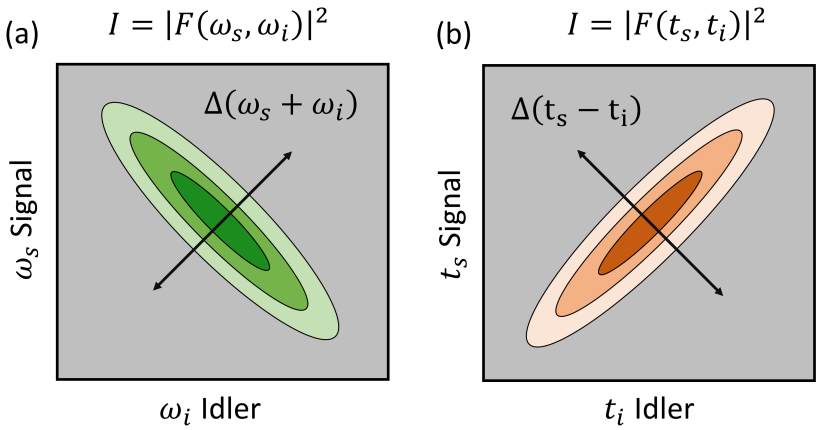

Figure 2.5: Joint spectral intensity (JSI) and joint temporal intensity (JTI) of energy-time entangled photons.

Characterizing spectral and temporal correlations is a major focus in this thesis. Photons from SPDC are naturally anticorrelated in frequency to satisfy energy conservation,

as shown in Fig 2.4, and positively correlated in their time-of-arrival. Since SPDC is a probabilistic process, there is an uncertainty in the generation time of photon pairs corresponding to where in the crystal they were created. Regardless of when they are created, they must be produced at the same time, hence the positive time-of-arrival correlations. The two-photon temporal correlations are obtained by Fourier transforming the joint spectral amplitude,

$$F(t_s, t_i) = \int d\omega_s d\omega_i F(\omega_s, \omega_i) e^{i\omega_s t_s} e^{i\omega_i t_i} \tag{2.56}$$

where the SPDC state can now be written as a double time integral,

$$|\psi\rangle_{spdc} \propto \int dt_s dt_i F(t_s, t_i) a_s^\dagger(t_s) a_i^\dagger(t_i) \, |0\rangle_s \, |0\rangle_i \,, \tag{2.57}$$

and $F(t_s, t_i)$ is called the joint temporal amplitude. Joint measurements of the two-photon state can be filtered to select specific frequency or time-of-arrival components to probe the correlations. Single photon detectors measure counts proportional to the intensity of the spectrally or temporally filtered field, not the amplitude, which are related by the squared absolute value. The joint spectral intensity, $|F(\omega_s, \omega_i)|^2$, and the joint temporal intensity, $|F(t_s, t_i)|^2$, of energy-time entangled photons are conceptually represented by Fig. 2.5. Note, separable states that are not entangled in the energy-time degree of freedom can be written as $F(\omega_s, \omega_i) = F(\omega_s)F(\omega_i)$, and therefore exhibit circular or non-correlated oval shapes in the JSI and JTI, as opposed to positively and negatively correlated ellipses shown in the figure. The widths of these distributions along the $\omega_s = \omega_i$ axis and $t_s = -t_i$ axis can together be measured to verify energy-time entanglement which will be the focus of Chapter 5.

2.5 The Optical Kerr Effect

We have seen how crystals with $\chi^{(2)}$ nonlinear optical properties enable three-wave mixing processes such as SHG and SPDC. In this section, we discuss a four-wave mixing nonlinear optical effect depending on the third order term in the polarization expansion giving a nonlinear polarization

$$P^{\mathrm{NL}}(\omega) = 3\epsilon_0 \chi^{(3)}(\omega = \omega + \omega - \omega)|E(\omega)|^2 E(\omega), \tag{2.58}$$

where we assume linear polarization and take $\chi^{(3)}$ to be a scalar for simplicity. The total polarization is the sum of linear and nonlinear polarization,

$$\begin{aligned} P(\omega) &= P^{(1)}(\omega) + P^{\mathrm{NL}}(\omega) \\ &= \epsilon_0 \chi^{(1)} E(\omega) + 3\epsilon_0 \chi^{(3)} |E(\omega)|^2 E(\omega) \\ &= \epsilon_0 \chi_{\mathrm{eff}} E(\omega), \end{aligned} \tag{2.59}$$

where

$$\chi_{\mathrm{eff}} = \chi^{(1)} + 3\chi^{(3)} |E(\omega)|^2 \tag{2.60}$$

is the effective susceptibility which takes both the linear and nonlinear term into account. Generally [4], the index of refraction of a medium is given by

$$n = \sqrt{1 + \chi_{\mathrm{eff}}}. \tag{2.61}$$

In many materials, the index of refraction has a component that increases with increasing electric field intensity as

$$n = n_0 + \bar{n}_2 \left\langle E^2(t) \right\rangle, \tag{2.62}$$

where n_0 is the weak-field refractive index and $\bar{n}_2$ is the second-order index of refraction, and

$$\left\langle E^2(t) \right\rangle = \left\langle (E(\omega) e^{-i\omega t} + E^*(\omega) e^{i\omega t})^2 \right\rangle = 2|E(\omega)|^2. \tag{2.63}$$

Comparing the two equations for index of refraction, Eq. 2.61 and Eq. 2.63, gives

$$\begin{aligned} [n_0 + 2\bar{n}_2 |E(\omega)|^2] &= 1 + \chi^{(1)} + 3\chi^{(3)} |E(\omega)|^2 \\ [n_0^2 + 4n_0 \bar{n}_2 |E(\omega)|^2 + 4n_0 \bar{n}_2^2 |E(\omega)|^4] &= 1 + \chi^{(1)} + 3\chi^{(3)} |E(\omega)|^2. \end{aligned} \tag{2.64}$$

By only considering terms up to order $|E(\omega)|^2$, the constant terms and squared terms can be compared to give

$$n_0 = \sqrt{1 + \chi^{(1)}}, \qquad \bar{n}_2 = \frac{3\chi^{(3)}}{4n_0}. \tag{2.65}$$

Here, we see higher $\chi^{(3)}$ susceptibilities correspond to a larger intensity-dependent index of refraction.

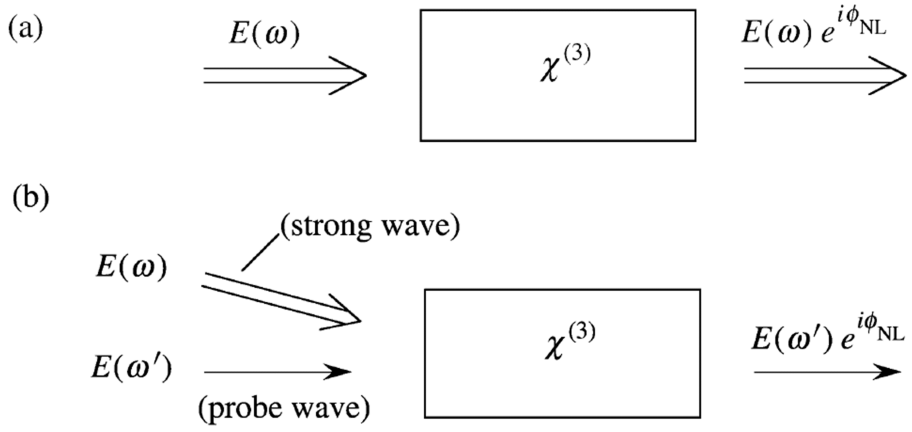

Figure 2.6: Two ways of measuring an intensity dependent refractive index. (a) A strong beam modifies its own propagation via self-phase modulation (SPM), and (b) a strong beam modifies the propagation of a weak beam via cross-phase modulation (XPM). © Boyd (2008) [4].

An intensity-dependent index of refraction can also be measured by a weaker probe beam, $E(\omega')$, when the nonlinear polarization is due to a strong beam of amplitude $E(\omega)$ like before. In this case, the nonlinear polarization is given by

$$P^{\mathrm{NL}}(\omega') = 6\epsilon_0\chi^{(3)}(\omega' = \omega' + \omega - \omega)|E(\omega)|^2 E(\omega'). \tag{2.66}$$

Note, the proportionality constant is bigger than the previous nonlinear polarization by a factor of two. The derivation of intensity dependent refractive index remains the same except for this factor yielding an index of refraction,

$$n = n_0 + 2\bar{n}_2^{(\mathrm{cross})}|E(\omega)|^2, \tag{2.67}$$

where

$$\bar{n}_2^{(\text{cross})} = \frac{3\chi^{(3)}}{2n_0}. \tag{2.68}$$

Thus, a strong laser induces an intensity-dependent index of refraction change in a weak probe wave twice as much as it induces in its own index of refraction. These two processes are depicted in Fig. 2.6. The intensity-dependent change in the nonlinear index of a strong beam influencing itself is referred to as self-phase modulation (SPM) and shown in Fig.2.6(a), while a strong beam influencing a second beam in this way is called cross-phase modulation (XPM), as shown in Fig.2.6(b).

Note that it is also common to define the intensity-dependent index of refraction as

$$n = n_0 + n_2 I, \tag{2.69}$$

where we have written n_2 without the bar on top to differentiate it from the previous definition, and I is the time-averaged intensity given by

$$I = 2n_0\epsilon_0 c|E(\omega)|^2. \tag{2.70}$$

Comparing our two definitions of n gives

$$2\bar{n}_2|E(\omega)| = n_2 I, \tag{2.71}$$

which shows n_2 is related to $\bar{n}_2$ by

$$n_2 = \frac{\bar{n}_2}{n_0\epsilon_0 c}. \tag{2.72}$$

Substitution of Eq. 2.65 gives the relationship between n_2 and $\chi^{(3)}$ as

$$n_2 = \frac{3}{4n_0^2\epsilon_0 c}\chi^{(3)}. \tag{2.73}$$

This change in the refractive index is called the optical Kerr effect, and the XPM variant is utilized as the core feature for ultrafast temporal measurements of single photons in the work presented in Chapter 5. Interestingly, this effect was named because of an analogy

with a different refractive index effect called the Kerr electrooptic effect. Instead of being caused by the electric field from an optical beam, the Kerr electrooptic effect describes a changing refractive index due to an applied static electric field, which also scales as the square of the field strength.

2.5.1 Optical Kerr Shutter

Cross-phase modulation from a strong pulsed laser can be used to perform a gated measurement of the temporal profile of a probe wave [94]. In this thesis, XPM occurs in a single mode fiber which is not birefringent [2] and is isotropic with no $\chi^{(2)}$ component to the nonlinear polarization, so for the discussion below we will consider a medium with these properties. The time-dependent index of refraction in the horizontal and vertical orientation of the fiber is given by

$$\begin{aligned} n_x(t) &= n_0 + 2n_2 I_p(t) \\ n_y(t) &= n_0 + 2n_2 b I_p(t), \end{aligned} \tag{2.74}$$

where $I_p(t)$ is the intensity of the pulsed laser which is horizontally polarized, and $b = 1/3$ for an isotropic material such as SMF [95, 96]. When $I_p(t) = 0$, we can see the material is not birefringent, $n_x = n_y$. When $I_p(t)$ is increased, the horizontal index of refraction increases three times faster relative to the vertical index of refraction which creates an induced birefringence. For a probe beam of wavelength λ_s in a SMF of length L, the induced index of refraction imparts a time dependent phase given in each spatial direction as

$$\begin{aligned} \Delta\phi_x(t) &= 2n_2 I_p(t) \left(\frac{2\pi L}{\lambda_s}\right) \\ \Delta\phi_y(t) &= \frac{2}{3} n_2 I_p(t) \left(\frac{2\pi L}{\lambda_s}\right). \end{aligned} \tag{2.75}$$

If the probe beam is parallel to one of these two axes, it will maintain its polarization and receive a phase shift. This has been utilized in previous experiments in a configuration

[2] Technically, SMF has a slight birefringence that is compensated for in experiments with quarter- and half-waveplates. Putting tension on fibers can also impart a birefringence, but for the remaining discussion it is sufficient to consider an SMF with no birefringence.

called a nonlinear optical loop mirror (NOLM) [97], where the phase shift (or lack of phase shift when no gating is intended), routes photons in the probe wave to a different output port of a beamsplitter.

Alternatively, if the probe beam is diagonally polarized relative to the horizontally-polarized pump, the probe experiences a time dependent polarization rotation. When this effect is followed by a waveplate and PBS to transmit rotated probe light and reflect unrotated probe light, the configuration is referred to as an optical Kerr shutter. The difference in the two phase shifts in Eq. 2.75 provides the time-dependent phase difference experienced by the components of the probe wave parallel and perpendicular to the pump and is given by

$$\Delta\phi(t) = \Delta\phi_x(t) - \Delta\phi_y(t) = \frac{8\pi n_2 L_{\text{eff}} I_p(t)}{3\lambda_s}. \tag{2.76}$$

For a pump and probe wave with different centre wavelengths, the two beams will travel with different group velocities in the SMF. In this case, the nonlinear phase shift can be modeled as an integral of the pump pulse intensity in the reference frame of the signal probe beam, given by

$$\Delta\phi(T) = \frac{8\pi n_2}{3\lambda_s} \int_0^L dz I_p(T - d_w z), \tag{2.77}$$

where z is propagation distance in the SMF, the temporal walkoff of the two pulses in the fiber is $d_w = v_{g_p}^{-1} - v_{g_s}^{-1}$, v_{g_p} and v_{g_s} are the group velocities of the pump and signal, respectively, and $T = t - z/v_{g_s}$ is the reference frame moving with the signal pulse. In the OKS configuration, a half-waveplate and PBS are placed after the Kerr medium and the transmission of signal field through the PBS is called the rotation efficiency, given by

$$\eta(T) = \sin^2(2\theta)\sin^2\left(\frac{\Delta\phi(T)}{2}\right), \tag{2.78}$$

where θ is the initial angle between pump and signal polarization incident on the SMF. This efficiency is maximized by $\theta = \pi/4$, when the pump is set to horizontal and the signal is set to diagonal.

2.6 Ultrafast Optics

Ultrafast laser pulses provide the ability to measure physical processes with incredible time resolution. The word ultrafast is held for the timing regime of events with a duration of picoseconds (10^{-12}s) or shorter [98]. For perspective, nanosecond resolution is approximately the limit of high speed electronics. When looking to route signals, measure fast phenomena, or interact with a system for only brief moments, femtosecond (10^{-15}s) lasers are commonly used as a source of ultrashort optical pulses.

Measurement of fast events typically requires gating from even faster processes, making ultrashort optical pulses difficult to measure. For example, the sports-mode feature in many cameras can help a photographer capture the moment a golf club strikes a ball. Gating the fast event of the strike with faster electronic events breaks up the moment into small pieces to map out the process. In contrast, an optical pulse with a sub-picosecond width cannot be gated by faster events simply because faster events are difficult and expensive to produce. Instead, the pulse is used to gate itself using a technique called autocorrelation.

An autocorrelator splits a pulse up with a beamsplitter in an unbalanced Mach-Zehnder interfermoter where one arm has a variable time delay. The pulses are then combined and input to a nonlinear crystal. A common method uses SHG and was proposed in 1967 [99]. The output second harmonic generation is recorded as a function of relative time delay between the two pulses. This is called the intensity autocorrelation, $A^{(2)}(\tau)$, and if the pulse is faster in time than the resolution of the photodetector (which it likely is if you need an autocorrelator in the first place), is given by

$$A^{(2)}(\tau) = \int_{-\infty}^{\infty} dt I(t) I(t-\tau). \tag{2.79}$$

The intensity autocorrelation provides an estimate of the pulse length because the SHG signal will be brighter when both beams overlap in time. However, it is an overestimate of the true pulse length. In 1993, Trebino et al. [100] showed that although the autocorrelation is insufficient to reconstruct the ultrafast input pulse, the spectrum of the autocorrelation, called the spectrogram of the pulse, could be measured to reconstruct the amplitude and phase of the pulse with phase reconstruction algorithms. This technique is called frequency resolved optical gating (FROG) and was a major breakthrough in the ultrafast optics community. Readers interested in a detailed description of the algorithms used in reconstruction and an in-depth description of phase retrieval are encouraged to read Trebino's textbook [78].

Originally developed for classical fields, FROG requires light with a high enough intensity to measure a spectrum of the upconverted signal. In past experiments, our group has shown that similar phase reconstruction algorithms can be used to reconstruct the amplitude and phase of the joint spectral amplitude to fully characterize energy-time entangled photons [101, 102]. This technique requires measurement of the joint temporal intensity and joint spectral intensity, in addition to the time-frequency and frequency-time joint correlations of the two photons. This thesis builds on this work in Chapter 5 by exploring an optical gating method which utilizes the $\chi^{(3)}$-enabled optical Kerr effect instead of the $\chi^{(2)}$ processes previously used.

2.6.1 Pulse Propagation in a Medium

An ultrafast pulse is made up of many different modes. It can have multiple spatial modes, polarization modes, and frequency modes in superposition. When it travels through a medium, each of the different modes can interact with dipoles in the medium in different ways which causes the modes to travel at different speeds. This is called dispersion and regardless of which modes are being dispersed by the medium, the pulse becomes stretched out in time as the modes walk off from each other. Each type of dispersion has a different name related to the associated degree of freedom of light, such as modal dispersion, polarization dispersion, and chromatic dispersion. The latter two are self explanatory but to clarify on the first, modal dispersion specifically refers to the spatial mode of light. Single mode fibers only allow one spatial mode and so are unaffected by modal dispersion, but multimode fibers couple in different spatial modes which can be separated in time in the fiber.

Chromatic dispersion has already been mentioned in Sec. 2.5.1, but it is treated more rigorously here because it is perhaps the most relevant type of dispersion when considering ultrafast pulses made of many frequencies, and chromatic dispersion affects energy-time correlations which are a primary focus of this thesis. The bandwidth and pulse width are related by the Fourier transform, so the shorter a laser pulse is in time, the larger its bandwidth and the more frequency modes are in superposition within the pulse. Note, for this reason, femtosecond lasers can also be referred to as broad band lasers.

Recall the form of the nonlinear driven wave equation from Sec. 2.2.1,

$$-\boldsymbol{\nabla}^2\mathbf{E}(t) + \frac{\epsilon^{(1)}}{c^2}\frac{\partial^2}{\partial t^2}\mathbf{E}(t) = -\frac{1}{\epsilon_0 c^2}\frac{\partial^2}{\partial t^2}\mathbf{P}^{\mathrm{NL}}(t). \tag{2.80}$$

Chromatic dispersion affects the frequency modes of the electric field, so we can rewrite the fields in terms of their frequency dependence using the Fourier transform,

$$\begin{aligned}\mathbf{E}(t) &= \frac{1}{\sqrt{2\pi}}\int d\omega \mathbf{E}(\omega)e^{i\omega t} \\ \mathbf{P}^{\mathrm{NL}}(t) &= \frac{1}{\sqrt{2\pi}}\int d\omega \mathbf{P}^{\mathrm{NL}}(\omega)e^{i\omega t}.\end{aligned} \tag{2.81}$$

substituting these into the driven wave equation, taking time derivatives of $e^{i\omega t}$, and replacing $\epsilon^{(1)}$ with $n^2(\omega)$ gives

$$-\boldsymbol{\nabla}^2\mathbf{E}(\omega) - \frac{n^2(\omega)\omega^2}{c^2}\mathbf{E}(\omega) = \frac{\omega^2}{\epsilon_0 c^2}\mathbf{P}^{\mathrm{NL}}(\omega). \tag{2.82}$$

In the absence of a driving nonlinear polarization field, $\mathbf{P}^{\mathrm{NL}}(\omega) = 0$, one possible solution is given by plane waves where the field does not depend on x or y, given by

$$E(\omega, z) = A(\omega - \omega_0)e^{-ik(\omega)z} + A^*(-\omega - \omega_0)e^{ik(\omega)z}, \tag{2.83}$$

where $k(\omega)$ is the wave vector in the linear medium given by

$$k(\omega) = \frac{n(\omega)\omega}{c}. \tag{2.84}$$

The terms in the complex exponent are often grouped together as

$$\phi(\omega, z) = k(\omega)z, \tag{2.85}$$

and referred to as the *spectral phase*. The dynamics of pulse propagation are described by the frequency dependent wave vector, and for this reason it is also commonly called the *propagation constant*. Expanding $k(\omega)$ about the central frequency of the pulse, ω_0, gives

$$k(\omega) = k(\omega_0) + \frac{dk}{d\omega}(\omega - \omega_0) + \frac{1}{2!}\frac{d^2k}{d\omega^2}(\omega - \omega_0)^2 + \frac{1}{3!}\frac{d^3k}{d\omega^3}(\omega - \omega_0)^3 + \ldots, \tag{2.86}$$

where the derivatives of $k(\omega)$ are evaluated at ω_0. Each of these derivatives have significant meaning for understanding pulse propagation, so we will label them as $k_n = \frac{d^n k}{d\omega^n}$ and write $k(\omega)$ as

$$k(\omega) = k_0 + k_1(\omega - \omega_0) + \frac{1}{2!}k_2(\omega - \omega_0)^2 + \frac{1}{3!}k_3(\omega - \omega_0)^3 + \dots. \tag{2.87}$$

Note, notation can change between sources giving a description of pulse dispersion. Some textbooks refer to the propagation constant as $\beta(\omega)$, and others describe dispersion by expanding the spectral phase, $\phi(\omega, z)$, and labelling its derivatives instead.

The phase velocity is given by the zeroth order term as

$$v_p = \frac{\omega_0}{k_0}, \tag{2.88}$$

while the group velocity of the pulse is a function of the first order term as

$$v_g = \frac{1}{k_1}. \tag{2.89}$$

The group velocity can be thought of as the velocity at which the medium transfers the energy of a pulse. It is equivalent to the speed of light when the pulse is in a vaccuum, and slows down as the index of refraction of the material increases. In media where higher order terms, k_2, $k_3 \dots k_n$ are negligible, the pulse does not experience chromatic dispersion. However, when these terms contribute to the propagation, each higher order derivative describes a higher order of dispersion where frequency components travel with a linear, quadratic, or higher order variation in ω. These terms modify the shape of the pulse in time and frequency.

For example, when k_2 is nonzero, each frequency component receives a time delay,

$$\tau(\omega) = \frac{d\phi}{d\omega} = \frac{d(k(\omega)z)}{d\omega} = k_1 z + k_2(\omega - \omega_0)z. \tag{2.90}$$

The first term, $k_1 z$ is the delay corresponding to the central frequency mode, while the relative delay of each frequency component is given by the coefficient of the second term, $k_2 z$. This is called linear chromatic dispersion because the difference in the velocity of spectral modes varies linearly.

Dispersed pulses are also known as chirped pulses. This stems from the fact that a dispersed pulse has increasing (or decreasing) frequency over time similar to a bird's chirp. The amount of chirp is often given by the chirp parameter,

$$A = \frac{1}{2}\frac{d^2\phi}{d\omega^2} = \frac{k_2 z}{2}, \tag{2.91}$$

which is also the coefficient of $(\omega - \omega_0)^2$ in the expansion of spectral phase about the centre frequency. For this reason, we say that a linear chirp corresponds to a quadratic spectral phase. Similarly, quadratic chirp corresponds to cubic spectral phase, and so on for higher orders of dispersion.

The sign of the chirp parameter indicates whether higher or lower frequencies travel faster. Most materials, such as fiber and nonlinear crystals described in this thesis, lead to a positve chirp, $|A| > 0$, where low frequencies travel faster than high frequencies. This is called normal dispersion. Negative chirp, $|A| < 0$, is called anomalous dispersion and is a property of some specifically engineered fibers where the high frequencies travel faster than the lower frequencies. In the next section, I'll show how anomalous dispersion can be introduced by gratings to counteract normal dispersion in fiber.

Optical materials manufacturers often report the index of refraction [3] instead of the propagation constant. To calculate the dispersion caused by a material, we need to rewrite the propagation constant terms as functions of the index of refraction. The first three terms are given by

$$\begin{aligned}
k_0 &= k(\omega)\Big|_{\omega=\omega_0} = \frac{n(\omega_0)\omega_0}{c} \\
k_1 &= \frac{dk(\omega)}{d\omega}\Big|_{\omega=\omega_0} = \frac{\omega_0}{c}\left(\frac{n(\omega_0)}{\omega_0} + \frac{dn(\omega)}{d\omega}\Big|_{\omega=\omega_0}\right) \\
k_2 &= \frac{d^2k(\omega)}{d\omega^2}\Big|_{\omega=\omega_0} = \frac{\omega_0}{c}\left(\frac{2}{\omega_0}\frac{dn(\omega)}{d\omega}\Big|_{\omega=\omega_0} + \frac{d^2n(\omega)}{d\omega^2}\Big|_{\omega=\omega_0}\right).
\end{aligned} \tag{2.92}$$

Therefore, to calculate propagation constant derivatives, we need the entire function, $n(\omega)$. In 1872, Wolfgang Sellmeier proposed equations that modeled the empirical relationship between the index of refraction of a material and optical wavelength [103] of the form

[3] Unfortunately the exact number is actually a trade secret because it can be used to figure out what dopants the company uses. Fortunately, many online libraries provide decent estimates of n for different materials.

$$n^2(\lambda) = 1 + \sum_k \frac{c_k \lambda^2}{\lambda^2 - \lambda_k^2}. \tag{2.93}$$

The constants c_k and λ_k are different for each material and a large table containing the constants for most relevant materials can be found at [104]. For example, fused silica (SiO_2) in fibers has the following Sellmeier equation in the near infrared (NIR), for λ given in micrometers (μm):

$$n^2(\lambda) = 1 + \frac{0.6962\lambda^2}{\lambda^2 - (0.06840)^2} + \frac{0.4079\lambda^2}{\lambda^2 - (0.1162)^2} + \frac{0.8975\lambda^2}{\lambda^2 - (9.896)^2}. \tag{2.94}$$

This relationship between n and λ isn't directly compatible with the frequency dependent equations we have derived. So, k_0, k_1, and k_2 can be written in terms of λ by using the relationship between λ and ω,

$$\lambda = \frac{2\pi c}{\omega}, \tag{2.95}$$

and the differentiation chain rule to get

$$\frac{d\lambda}{d\omega} = \frac{-2\pi c}{\omega^2}. \tag{2.96}$$

Substitution of Eq. 2.95 and Eq. 2.96 into Eq. 2.92 gives

$$\begin{aligned} k_0 &= k(\lambda)\Big|_{\lambda=\lambda_0} = \frac{2\pi n(\lambda_0)}{\lambda_0} \\ k_1 &= \frac{dk}{d\omega}\Big|_{\omega=\omega_0} = \frac{dk}{d\lambda}\frac{d\lambda}{d\omega}\Big|_{\lambda=\lambda_0} = \frac{\lambda_0}{c}\left(\frac{n(\lambda_0)}{\lambda_0} - \frac{dn(\lambda)}{d\lambda}\Big|_{\lambda=\lambda_0}\right) \\ k_2 &= \frac{d^2k}{d\omega^2}\Big|_{\omega=\omega_0} = \frac{d}{d\omega}\left(\frac{dk}{d\lambda}\frac{d\lambda}{d\omega}\right)\Big|_{\lambda=\lambda_0} = \frac{\lambda_0^3}{2\pi c^2}\frac{d^2n(\lambda)}{d\lambda^2}\Big|_{\lambda=\lambda_0}. \end{aligned} \tag{2.97}$$

2.6.2 Dispersion Manipulation

In many optics experiments, single photon sources are compartmentalized and separated from the experiment by fiber. This is done to filter the spatial modes of the generated

photons and to ensure that misalignment of the source doesn't lead to misalignment of the rest of the experiment. With sources pumped by monochromatic continuous wave (CW) lasers, polarization rotation in the fiber is all there is to be concerned about. With pulsed sources, however, normal dispersion in the fiber is also a concern. The frequency modes separate from each other in time and the pulse stretches out. Chapter 5 involves measuring the energy-time correlations of photon pairs, and ideally we would like a measurement of the original pulse structure without normal dispersion altering the correlations.

To combat the normal dispersion in fiber, optics which spread out a beam's frequency modes, such as prisms [105] or diffraction gratings [106], can be used to geometrically engineer an anomalous dispersion setup where low frequency light has a longer path length to travel. If a pulse has been normally dispersed and spread out by fiber, the act of applying anomalous dispersion is called pulse compression because the pulse goes back to being shorter in time. Prism compressors have low loss but can take up a lot of space, and diffraction grating compressors are more compact but result in higher losses.

A diffraction grating based pulse compressor is illustrated in Fig. 2.7 (a). A light pulse is guided into the compressor at an angle θ_i relative to the normal. The first grating reflects the incoming pulse at an angle proportional to frequency, with the centre frequency reflected at angle θ_d. The second grating collimates the frequency components which are directed to a mirror. The mirror reflects the pulse back along the path it entered which recombines the frequency components spatially. Throughout the two paths, higher frequency components travelled a shorter distance than lower frequency components, illustrated by red and blue lines, which results in anomalous dispersion. The dispersion can be tuned by increasing the distance between the two gratings. To separate the incoming and outgoing pulses, the mirror can be slightly tilted out of the plane of this diagram. This results in two beams of slightly different heights before and after the compressor.

In Fig. 2.7 (b) you can see the spread in colours as a function of time within the pulse, where the blue frequency components are on the leading edge of the pulse, and the red frequency components trail. This is what we expect for anomalous dispersion where $|A| < 0$. Fig. 2.7 (c) shows the process that gives the compressor its name. Normally dispersed light, such as a pulse that has travelled through a normally dispersive medium, has its frequency components compressed back to the centre. If tuned properly, it can cancel out the dispersion applied by the dispersive medium. A picture of the grating compressor built for the experiment in chapter 5 is shown in Fig. 5.8.

The dispersion angle, θ_d, is given by the grating equation as

$$\sin(\theta_d) = \sin(\theta_i) + m\lambda\Lambda, \tag{2.98}$$

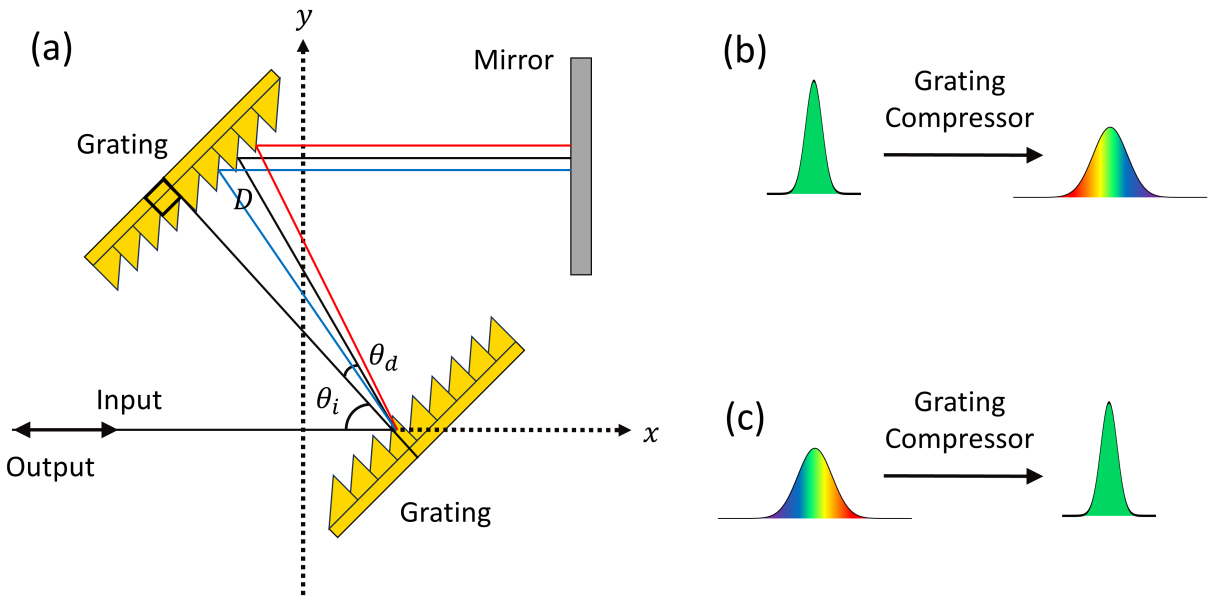

Figure 2.7: Schematic of a diffraction grating based pulse compressor. (a) A pair of gratings and a mirror make a pulse compressor which applies anomalous dispersion. A pulse comes in at angle θ_i relative to the gratings, the centre frequency of the pulse is reflected at angle θ_d relative to the gratings, and it travels a distance D to the second grating. The backwards path recombines the frequency components spatially. (b) An example of a short pulse having its frequency components spread out in time by a grating compressor. (c) An example of a normally dispersed pulse compressing back to its short duration by a grating compressor.

where m is the diffraction order and Λ is the grating frequency usually provided by the grating manufacturer in units of lines per mm. Taking the derivative of Eq. 2.98 gives,

$$\frac{d\theta_d}{d\lambda} = \frac{m\Lambda}{\cos(\theta_d)}. \tag{2.99}$$

Gratings are built to be most efficient when $\theta_i = \theta_d$, known as the *Littrow configuration*. After two passes and four grating reflections, a total transmission efficiency of 65% is possible [107, 108, 109]. If the gratings are far apart, it is sufficient to consider only the path between the two gratings as the wavelength dependent part of the path length, P,

given by

$$P = 2D\cos(\theta_d). \tag{2.100}$$

Note, for shorter path lengths, the path between the second grating and the mirror should also be considered to be wavelength dependent. A formal derivation of this case is given in Ref [89]. Differentiating Eq. 2.100 and substituting in Eq. 2.99 gives

$$\frac{d^2P}{d\lambda^2} = \frac{-2m^2\Lambda^2 D}{\cos^2(\theta_d)}, \tag{2.101}$$

which leads to a chirp given by [98],

$$A = \frac{1}{2}\frac{d^2\phi}{d\omega^2} = \frac{-m^2\lambda^3\Lambda^2}{2\pi c^2\cos^2(\theta_d)}D. \tag{2.102}$$

Note the negative sign corresponds to anomalous dispersion, and the distance between the two gratings can be tuned to change the chirp.

To give an example, gratings with $\Lambda = 1200\,\text{lines/mm}$, a centre wavelength of $\lambda = 847\,\text{nm}$, a dispersion angle of $\theta_d = 32°$, and a diffraction order of $m = 1$ provides a chirp value of $A = -2154.4\text{fs}^2/\text{mm}$ of grating separation, D. If you compare this to the normal dispersion in fiber of the same wavelength, $A = 21.82\text{fs}^2/\text{mm}$, the compressor comparatively applies two orders of magnitude more anomalous dispersion than a fiber applies normal dispersion. Therefore, a small grating compressor can compensate the dispersion from a long fiber.

Chapter 3

Talbot Effect of Orbital Angular Momentum Lattices with Single Photons

Notes and Acknowledgements

The contents of this chapter were published on April 13, 2020, as [110]:

S. Schwarz, C. Kapahi, R. Xu, A. R. Cameron, D. Sarenac, J. P. W. MacLean, K. B. Kuntz, D. G. Cory, T. Jennewein, K. J. Resch, and D. A. Pushin, Phys. Rev. A **101**, 043815 (2020).

Author Contributions

Kevin Resch, **Thomas Jennewein**, **Dmitry Pushin**, and **David Cory** conceived of the study.
Katanya Kuntz, **Jean-Philippe MacLean**, **Connor Kapahi**, and **Dusan Sarenac** helped implement the theory and general strategy.
Sacha Schwarz, **Ruoxuan Xu**, and **Andrew Cameron** built the experiment and took experimental results.
Sacha Schwarz wrote the first draft of the manuscript.
All authors contributed to the final version.

3.1 Chapter Overview

The self-imaging, or Talbot Effect, that occurs with the propagation of periodically structured waves has enabled several unique applications in optical metrology, image processing, data transmission, and matter-wave interferometry. In this work, we report on the first demonstration of a Talbot Effect with single photons prepared in a lattice of orbital angular momentum (OAM) states. We observe that upon propagation, the wavefronts of the single photons manifest self-imaging whereby the OAM lattice intensity profile is recovered. Furthermore, we show that the intensity at fractional Talbot distances is indicative of a periodic helical phase structure corresponding to a lattice of OAM states. This phenomenon is a powerful addition to the toolbox of orbital angular momentum and spin-orbit techniques that have already enabled many recent developments in quantum optics.

3.2 Context

The Talbot Effect [111] is a near-field diffraction phenomenon whereby periodic phase and amplitude modulations are self-imaged due to free-space propagation. In accordance with Fresnel diffraction [112], replicas of a periodic transverse intensity profile reappear after a specific propagation distance known as the Talbot length. The Talbot Effect has been demonstrated in numerous areas of research involving linear and nonlinear optical waves [113, 114, 115], single photons [116, 117, 118], x-rays [119], matter-waves [120, 121, 122, 123, 124, 125], exciton polaritons [126], and Bose-Einstein condensates [127]. The Talbot Effect has a diverse array of applications in optical metrology [128], imaging processing [129], and lithography [130, 131, 132], with potential in data transmission [133].

Here we consider the Talbot Effect manifested by lattices of orbital angular momentum (OAM) states. The OAM degree of freedom of light has garnered significant interest in various fields ranging from optical manipulation and high-bandwidth communication [134, 135, 136, 137] to quantum information processing [138, 2] and medical diagnostics [139, 140, 141]. In addition to the photonic applications, OAM beams have been extended to neutrons [142, 143, 144] and electrons [145, 146].

The Talbot Effect has been considered with classical light as well as OAM lattices [147, 148, 149, 5, 150, 151, 152]. In this chapter, we discuss our results of the first demonstration of the Talbot Effect with single photons prepared in a lattice of OAM states. The extension of the Talbot Effect to single photons and OAM techniques offers the possibility of utilizing quantum information processing protocols, such as remote state preparation,

to leverage quantum communication advantages [153]. Furthermore, self-imaging has potential applications in implementing quantum logic operations as qudits may be encoded in the transverse spatial profile of single photons [154, 155].

3.3 Concept and Theory

3.3.1 The Talbot Effect

The Talbot effect, also known as the self-imaging effect, is a classical optics phenomenon discovered by Talbot in 1836 [111]. Talbot observed that periodic structures of light will interfere in the near field, and reappear after a specific propagation distance.

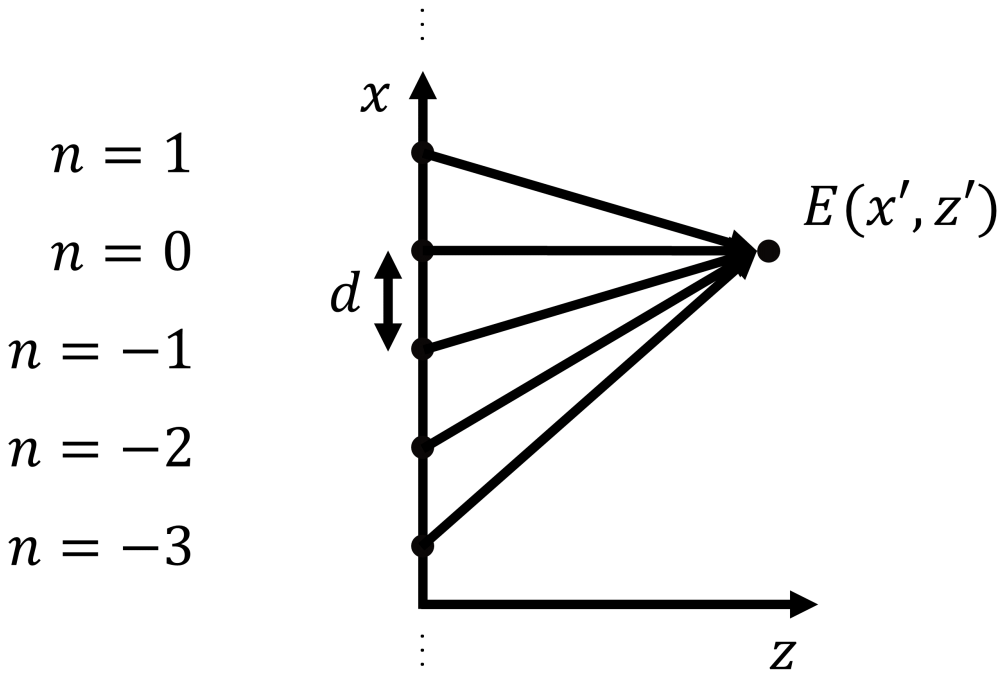

Figure 3.1: The setup for the derivation of the Talbot effect begins with multiple source emitters at $z = 0$ propagating along the z-axis and interfering in the near field to give $E(x, z)$.

Consider a superposition of plane waves in the XZ plane, coming from sources distributed along the x-axis. To calculate the electric field at a point x', z', denoted $E(x', z')$, we must add up all the contributions from different sources as displayed in Fig. 3.1. To model this, the electric field before propagation, $E(x, z = 0)$, will be derived and propagated forward in the z-direction using Fresnel diffraction [156]. The initial electric field is given by

$$E(x, 0) = \sum_{-\infty}^{\infty} E_n e^{-ink_d x}, \tag{3.1}$$

where

$$k_d = \frac{2\pi}{d}. \tag{3.2}$$

Fourier transforming into momentum space gives

$$\begin{aligned} E(k_x, 0) &= \int_{-\infty}^{\infty} dx E(x, 0) e^{ik_x x} \\ &= \int_{-\infty}^{\infty} dx \left[\sum_{-\infty}^{\infty} E_n e^{-ink_d x} \right] e^{ik_x x} \\ &= \sum_{-\infty}^{\infty} E_n \int_{-\infty}^{\infty} dx e^{i(k_x - nk_d)x} \\ &= \sum_{-\infty}^{\infty} E_n (2\pi\delta(k_x - nk_d)), \end{aligned} \tag{3.3}$$

where $\delta(x)$ is the Dirac delta function. In one dimension (ignoring y), the Fresnel diffraction approximation is given as, [157],

$$E(x, z) = \frac{e^{-ikz}}{2\pi} \int_{-\infty}^{\infty} dk_x E(k_x, 0) e^{\frac{ik_x^2 z}{2k}} e^{-ik_x x}, \tag{3.4}$$

where $k = \frac{2\pi}{\lambda}$ is the propagation wave vector. Substituting Eq. 3.3 into Eq. 3.4 gives

$$
\begin{aligned}
E(x,z) &= \frac{e^{-ikz}}{2\pi}\int_{-\infty}^{\infty} dk_x \left[\sum_{-\infty}^{\infty} E_n(2\pi\delta(k_x - nk_d))\right] e^{\frac{ik_x^2 z}{2k}} e^{-ik_x x} \\
&= e^{-ikz}\sum_{-\infty}^{\infty} E_n e^{\frac{i(nk_d)^2 z}{2k}} e^{-i(nk_d)x},
\end{aligned}
\tag{3.5}
$$

where the delta function handled the integral and subsequently set all terms where $k_x \neq nk_d$ to zero. Now, define the Talbot length as

$$
z_T = \frac{2d^2}{\lambda}, \tag{3.6}
$$

which enables writing $E(x,z)$ as

$$
E(x,z) = e^{-ikz}\sum_{-\infty}^{\infty} E_n e^{\frac{i2\pi n^2 z}{z_T}} e^{-2\pi i n x/d}. \tag{3.7}
$$

The Talbot effect emerges at propagation distance $z = z_T$, where

$$
e^{\frac{i2\pi n^2 z}{z_T}}\Big|_{z=z_T} = e^{\frac{i2\pi n^2 (z_T)}{z_T}} = e^{i2\pi n^2} = 1, \quad \text{for all } n. \tag{3.8}
$$

Therefore, the electric field at the Talbot length propagation distance, $z = z_T$, becomes

$$
E(x,z_T) = e^{-ikz_T}E(x,0) \Rightarrow |E(x,z_T)| = |E(x,0)|, \tag{3.9}
$$

which means the field reproduces itself. Fractional Talbot length distances are also interesting. At $z = z_T/2$, the exponential instead simplifies to

$$
e^{\frac{i2\pi n^2 z}{z_T}}\Big|_{z=z_T/2} = e^{\frac{i2\pi n^2 (z_T/2)}{z_T}} = e^{i\pi n^2} = e^{i\pi n}. \tag{3.10}
$$

The final equality holds because when n is even, $e^{i\pi n^2} = e^{i\pi n}$, and when n is odd, $n = 2m+1$, giving $e^{i\pi n^2} = e^{i\pi(2m+1)n} = e^{2\pi i n m}e^{i\pi n} = e^{i\pi n}$. This results in an electric field given by

$$E(x, z_T/2) = e^{-ikz_T/2} \sum_{-\infty}^{\infty} E_n e^{i\pi n} e^{-2\pi i n x/d} = e^{-ikz_T/2} \sum_{-\infty}^{\infty} E_n e^{-2\pi i n (x-d/2)/d}. \tag{3.11}$$

Similar to before, we can write the electric field at half the Talbot length in terms of the electric field before propagation as

$$E(x, z_T/2) = e^{-ikz_T/2} E(x - \frac{1}{2}d, 0). \tag{3.12}$$

From this, we can see that the field is also reproduced at half of the Talbot length, but with a lateral phase shift of $d/2$. Continuing in this way, one can calculate the electric field at even smaller fractional lengths, $z_T/4, z_T/8$, etc., to recover the electric field with phase shifts and increasing image frequency. Plotting out the intensity of the field as a function of z is referred to as the Talbot carpet. An example of this pattern is shown in Fig. 3.3.

As is demonstrated experimentally later on in Sec. 3.6, a periodic transverse field in two dimensions propagating in z also realizes reimaging at fractional Talbot length propagation distances.

3.3.2 LOV Prism Pairs Aside

In this section, a quick history of the optics that are used to create periodic OAM structures in this chapter and chapter 4 will be presented. Our group joined in to this collaboration when the "Lattice of Optical Vortices" (LOV) prisms had already been proposed and demonstrated by Dmitry Pushin and David Cory's group, and it will help bring context to briefly share the lead up to this collaboration.

In 2016, Nsofini et al. [158] proposed a way to create spin-orbit entangled states in neutrons. Spin-orbit coupling in this case refers to correlations between the spin of a neutron and the orbital angular momentum of a neutron. Entanglement of this type between different degrees of freedom of a physical system is sometimes referred to as hyperentanglement. They proposed applying a quadrupole magnetic field operator of the form

$$\begin{aligned} U_Q &= e^{i(\pi r/2r_c)[\cos(\phi)\hat{\sigma}_x + \sin(\phi)\hat{\sigma}_y]} \\ &= \cos\left(\frac{\pi r}{2r_c}\right) I + i\sin\left(\frac{\pi r}{2r_c}\right)(\hat{l}_+\hat{\sigma}_+ + \hat{l}_-\hat{\sigma}_-), \end{aligned} \tag{3.13}$$

to a spin-up polarized neutron, where r is the radial coordinate of the field, r_c is the radius at which the neutron spin flips its sign, I is the 2×2 identity matrix, $\hat{l}_{\pm} = e^{\pm i\phi}$ are raising/lowering OAM operators, and $\sigma_{\pm} = (\hat{\sigma}_x \pm i\hat{\sigma}_y)/2$ are superpositions of the Pauli operators. Once applied to a spin-up neutron, the polarization and OAM would become entangled. This operator could be realized by passing a spin-up neutron through the centre of a quadrupole magnetic field.

Next, in 2018, an analogy from neutron beams to laser beams was formed. Sarenac et al. [5] showed that the quadrupole operator could be approximated by the repeated application of two simpler unitary operators of the form

$$\hat{U}_Q = e^{i(\pi r/2r_c)[\cos(\phi)\hat{\sigma}_x + \sin(\phi)\hat{\sigma}_y]} \approx (\hat{U}_x \hat{U}_y)^N, \tag{3.14}$$

where

$$\hat{U}_x = e^{i\frac{\pi}{2r_c}(x-x_0)\hat{\sigma}_x}, \quad \hat{U}_y = e^{i\frac{\pi}{2r_c}(y-y_0)\hat{\sigma}_y}, \tag{3.15}$$

and (x, y) are the transverse coordinates of the neutron beam with center coordinate (x_0, y_0). Sarenac et al. implemented these unitaries physically with neutron beams and magnetic fields [144], as well as optically with classical laser light and birefringent prisms [5].

The analogy connecting neutrons and photons highlights the similarities of the two systems and the benefit of describing quantum systems with a common quantum information language. The spin of a neutron is referring to the physical property spin angular momentum. Photon's that are circularly polarized carry spin-angular momentum as well, and the two concepts can both be described by the Pauli matrices and a two-dimensional Hilbert space. Physically, neutron spin is affected by applied magnetic fields, while photon polarization is affected by birefringent materials. Both systems also have an orbital angular momentum component as well. Photon OAM has been discussed in detail in Sec. 1.3.2, and neutron OAM can be thought of in a similar manner where a neutron beam has a helical phase dependence.

The physical analogy enables the quadrupole approximating magnetic fields to be represented in the optics regime by birefringent gradients as seen in Fig. 3.2. Each wedge shaped optic refers to a single unitary U_x or U_y, where the radial constant has been changed to $a = 2r_c$. Pairs of these optical elements are referred to as LOV-prism pairs. After Sarenac et al. published their work in the classical optics regime [5], the LOV prism pairs were brought to our lab to work with single photons. The intensity pattern is periodic in two-dimensions, which enabled the first experiment described in the following sections where two dimensional single-photon Talbot carpets are observed.

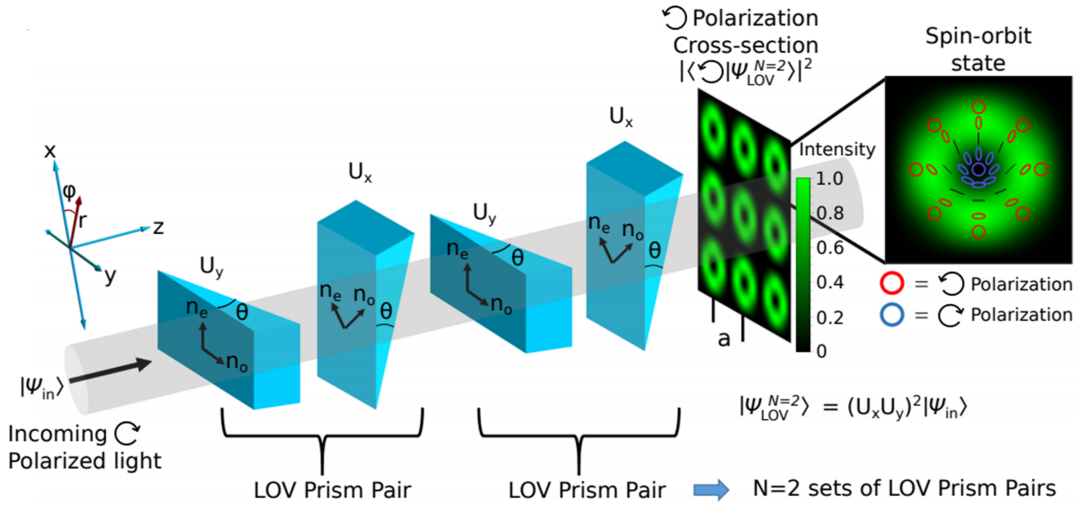

Figure 3.2: Circularly polarized light passes through four birefringent wedges called lattice of optical vortices (LOV) prism pairs. This creates an array of spin-orbit states which each have a polarization-dependent orbital angular momentum. The displayed intensity distribution can be seen by projecting the state on to left circularly polarized light and placing a CCD camera. © D. Sarenac et al., (2018) [5].

3.3.3 2D Talbot Carpet Realized by Spin-orbit Single Photons

We consider spin-orbit states described by the wavefunction

$$|\Psi\rangle = A(r,\phi)\left[\cos\left(\frac{\pi r}{d}\right)|R\rangle + ie^{i\ell\phi}\sin\left(\frac{\pi r}{d}\right)|L\rangle\right], \tag{3.16}$$

where (r,ϕ) are the cylindrical coordinates, ℓ specifies the OAM number, d is the distance in which the polarization state performs a full rotation on the Poincaré sphere, $|R\rangle$ and $|L\rangle$ denote the right and left circular polarization states, and $A(r,\phi)$ denotes the envelope. A lattice of spin-orbit states can be obtained by passing circularly polarized light through pairs of birefringent linear gradients whose optical axes are perpendicular to each other [5, 159]. This may be derived by considering the Suzuki-Trotter expansion of the operator $\hat{U}$ which generates the spin-orbit state in Eq. 3.16 when acting on an input state $|R\rangle$, where

$$\hat{U} = e^{i\frac{\pi}{d}[x\hat{\sigma}_x + y\hat{\sigma}_y]} = \lim_{N\to\infty}(e^{i\frac{\pi x}{Nd}\hat{\sigma}_x}e^{i\frac{\pi y}{Nd}\hat{\sigma}_y})^N. \tag{3.17}$$

Truncating the expansion to N terms, the operators in Eq. 3.17 can be realized by sets of perpendicular birefringent gradients with the general form

$$\hat{U}_x = e^{i\frac{\pi}{a}(x-x_0)\hat{\sigma}_x}, \quad \hat{U}_y = e^{i\frac{\pi}{a}(y-y_0)\hat{\sigma}_y}, \tag{3.18}$$

where the origin of the gradients is given by (x_0, y_0), $\hat{\sigma}_{x,y}$ are Pauli matrices, and where $a = Nd$. It was shown in Ref. [5] that linear gradients of Eq. 3.18 may be implemented via "Lattice of Optical Vorticies" (LOV) prism pairs. A LOV prism pair consists of two wedge-shaped birefringent prisms where the optical axis of the first prism is along the wedge incline direction and that of the second is offset by 45° [5]. By sending a photon in the right circular polarization state $|R\rangle$ through N sets of LOV prism pairs, we prepare the state

$$\left|\Psi^N_{\text{LOV}}\right\rangle = \alpha(x,y)(\hat{U}_x\hat{U}_y)^N \left|R\right\rangle, \tag{3.19}$$

where $\alpha(x, y)$ describes the incoming Gaussian beam envelope with beam waist w_0. The periodic nature of polarization rotations enables the linear gradients to prepare a two-dimensional lattice of spin-orbit states.

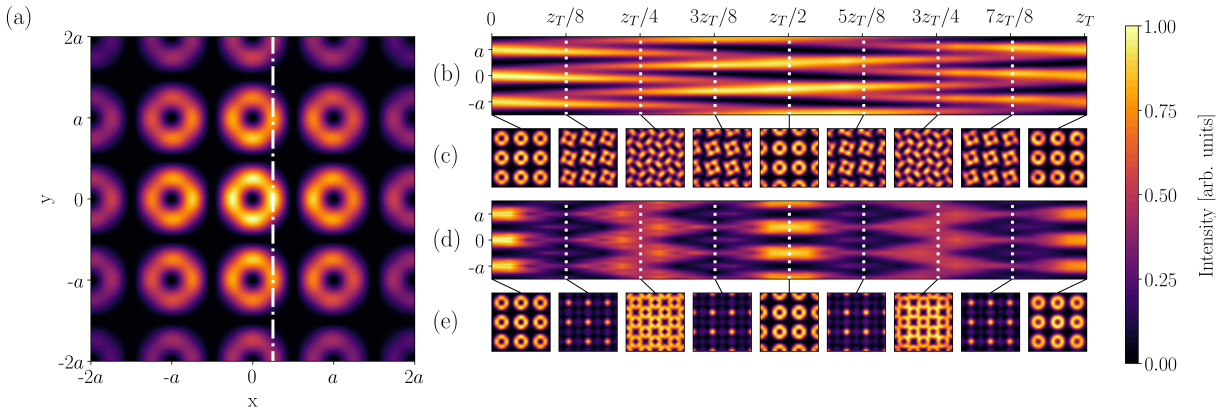

Figure 3.3: Simulated intensity distributions in both the xy and yz planes, where the beam propagates along z. (a) Right-handed circularly polarized light is sent through $N = 2$ sets of LOV prism pairs, which yields a lattice of ring-shaped intensity structures when filtered with respect to the left-handed circular polarization, i.e., $I(x, y) = |\langle L| \left|\Psi^{N=2}_{\text{LOV}}\right\rangle|^2$ at propagation distance $z = 0$. Note that here the Gaussian intensity envelope $\alpha(x, y)$ with beam waist $w_0 = 3a$ is added. (b) By plotting the yz intensity at $x = a/4$ (indicated in (a) with the dash dotted white line) we recover what is known as the Talbot carpet. (c) xy intensity patterns at specific propagation distances z. (d-e) The Talbot carpet and the xy intensity cross sections when the phase structure of the initial beam is removed. This demonstrates the effect of the OAM lattice phase structure on the intensity profile at the fractional Talbot distances.

Filtering on one circular polarization state prepares a periodically structured intensity distribution with a lattice spacing of $a = \lambda(\Delta n \tan(\theta))^{-1}$, where Δn and θ are the birefringence and the incline angle of the LOV prism pairs respectively, and λ is the wavelength. In our experiment we use $N = 2$ LOV prism pairs and we filter on $|L\rangle$ to obtain an initial intensity distribution of the form

$$\begin{aligned} I(x,y) &= |\langle L| \left|\Psi_{\mathrm{LOV}}^{N=2}\right\rangle|^2 \\ &= |\alpha(x,y)|^2 \cos^2\left[\frac{\pi x}{a}\right] \cos^2\left[\frac{\pi y}{a}\right] \\ &\quad \times (2 - \cos\left[\frac{2\pi(x+y)}{a}\right] - \cos\left[\frac{2\pi(x-y)}{a}\right]), \end{aligned} \tag{3.20}$$

which is depicted in Fig. 3.3(a).This periodic beam structure imprinted by the LOV prism pairs sets up conditions required for the Talbot Effect. The transmitted light interferes in such a way that after a distance $z_T = 2a^2/\lambda$, the initial periodic intensity pattern reappears. The same intensity distribution also appears at half the distance, $z_T/2$, but with spatial shifts $\Delta a = a/2$ along the x- and y-directions. Furthermore, the intensity distribution at propagation distances much larger than the Talbot distance results in the Fourier transform of the initial periodic pattern. The Fraunhofer distance (far-field) is given by $z_F = 8w_0^2/\lambda$, where w_0 is the beam waist. In our setup $z_F \approx 166$ m.

Theory predicts the same self-imaging phenomenon for single photons. We describe the free-space propagation of single photons by a complex-valued transverse field distribution $E(x,y)$ convoluted with the Fresnel propagator

$$K_F(x,y,z) = \frac{e^{ikz}}{i\lambda z} \exp\left[\frac{ik}{2z}(x^2+y^2)\right], \tag{3.21}$$

where k is the wavevector. The field $E(x,y)$ at position z is evaluated via

$$E(x,y,z) = \frac{e^{ikz}}{i\lambda z} \iint dx'dy'\, E(x',y',0)\, e^{\frac{ik}{2z}[(x-x')^2+(y-y')^2]}. \tag{3.22}$$

Fig. 3.3(a) shows the simulated transverse intensity distribution, $I(x,y) = |\langle L|\psi_{\mathrm{LOV}}^{N=2}\rangle|^2$, before beam propagation. Fig. 3.3(b) and Fig. 3.3(d) depict the intensity distribution in the yz-planes at $x = a/4$ for the initial states $\langle L|\psi_{\mathrm{LOV}}^{N=2}\rangle$ and $|\langle L|\psi_{\mathrm{LOV}}^{N=2}\rangle|$, respectively. Fig. 3.3(c) and Fig. 3.3(e) illustrate the intensity distribution in the xy-planes for specific

propagation distances. We observe that the initial phase profile defines the transverse intensity pattern at fractional Talbot distances. Furthermore, it can be observed that the OAM phase structure induces an asymmetry between the intensity distributions at propagation distances $\{z_T/8, z_T/4, 3z_T/8\}$ and $\{7z_T/8,\ 3z_T/4, 5z_T/8\}$.

3.4 Description of emICCD Operation for Single Photon Counting Experiments

The transverse beam profile of the signal photon is imaged with an electron-multiplying intensified CCD (emICCD) from Princeton Instruments with model number PI-Max4:1024 EM(B) as shown in Fig. 3.4. The camera has an active area of 1024 x 1024 pixels, which is slightly larger than a typical 1000 x 1000 megapixel. Each pixel is 13 μm x 13 μm in size, which makes an active area of around 1.3 cm x 1.3 cm. In photon counting experiments, each of the pixels on the camera acts as a single photon detector with multiple amplification steps. Measuring multiple copies of the same photonic state slowly builds up a 2D intensity pattern corresponding to the probability distribution of a single photon's transverse position. There are many parameters to select when operating the camera in single photon experiments, such as emICCD gain, electronic trigger delay, exposures per frame, number of frames, and trigger rate. Many different parameter combinations were tested as we aimed to boost the signal to noise ratio of the images. We built up a list of parameter heuristics that resulted in images that had a sharp contrast without taking too long to capture.

The first parameter that must be set is the trigger rate. In our experiment, we use the idler photon as an external trigger. Too many idler photons per second will overload the electronic camera trigger, but too few will result in images that take too long to build up. In our case, the maximum number of available idler photons from our single photon source (200 kHz) was much larger than the maximum trigger rate accepted by the camera (20 kHz). We adjusted the laser power pumping the SPDC crystal in order to lower the idler singles rate to a level that was acceptable for camera triggering, and found 15 kHz to work best. The idler photon singles rate fluctuates slightly, and a rate of 15kHz ensured we never crossed the boundary of 20 kHz which would cause electronic trigger errors.

The idler trigger can only effectively herald the arrival of the signal photon if the correct electronic delay is applied. We delayed the signal photon being imaged by a 30 m fiber ($\approx$ 144 ns delay) to ensure the idler photon trigger was received by the camera before the signal photon arrived at the camera. The electronic delay was chosen by first estimating

Figure 3.4: PI-MAX 4: 1024EM(B) Electron-Multiplied Charge-Coupled Device.

the expected delay due to the optical path differences, and then taking images of the signal photon with different electronic delays until a 2D Gaussian beam pattern emerged in the image. This process was trial-and-error based, and was sped up by starting with a large gate width (analogous to a coincidence window between two single photon detectors). First, a 100 ns window was used. Once we saw the 2D Gaussian image, we knew the electronic delay to within 100 ns. Next, the gate width was halved to 50 ns and the electronic delay was varied until we got the image back. This process was repeated until we reached the typical 3 ns coincidence window for single photon counting experiments.

For setting the correct gain, an understanding of exposures and frames is beneficial. An exposure is a single instance of data collection where the shutter of the camera opens, collects light, and closes [160]. A frame is collected when the camera digitizes the analog signal. Many exposures can gradually build up signal before it is digitized, which gives us the choice of how many exposures to include per frame. An exposure takes approximately 2 seconds, and the gate width of 3 ns ensures that only the light which arrived at the predetermined delay time relative to the idler photon will be intensified. In addition to choosing the number of exposures and frames to take, which affects the total counting time of an image, the amount of emICCD gain each exposure is boosted by can be set in the camera parameters section of the LightField software. When choosing a gain value, a balance between increasing contrast and saturated pixels must be considered. We have found that for our external trigger rate, 2000 exposures per frame with an emICCD gain of

9000 and 20 total frames produced images with the largest contrast. Each of the 20 frames were added together in postprocessing to create the single photon images in this thesis.

With all of the parameters locked in, background images were taken with the same parameters as the images while blocking the signal photons incident to the camera. If the single photon source varied in power over the course of an experiment and the number of trigger idler photons changed, a new background image was taken to ensure images and background images had the same external trigger rate. In post-processing, background subtraction was applied on a pixel-by-pixel basis. This was especially helpful for dealing with "hot" pixels that consistently lit up brighter.

Dark counts can build up false counts on the pixels across the active area. They are mainly caused by heat produced by the camera in the amplification steps, and are minimized by air-cooling the device to -20° C. We note that further cooling and dark count reduction could be added to the setup with the addition of a liquid cooling system. Similar to single photon detectors, cosmic rays can interact with the active area and be misinterpreted as single photon events. Once a photon is incident on a camera pixel, it is detected with a quantum efficiency of 25%.

3.5 Experimental Setup

The experimental setup is schematically depicted in Fig. 3.5. Degenerate photon pairs are prepared using type-II spontaneous parametric down-conversion in a Sagnac interferometer. We pump a 10 mm long periodically-poled KTP crystal (PPKTP) with a continuous wave diode laser (404.8 nm) to produce correlated photon pairs centered at $\lambda_{SP} = 810.8$ nm with a spectral bandwidth of 0.4 nm. With the pump horizontally polarized, we measure the second-order correlation function at zero time delay to be $g^{(2)}(0) = 0.0251 \pm 0.0011$, implying that two-photon events in any coincidence time window are around 1% [161]. Note that a diagonal polarized pump would offer the ability to generate a polarization entangled target state, however, here we herald the signal by means of measuring the idler (see Ref. [162] for further details). The outputs of the Sagnac interferometer are coupled into two single-mode fibers, which allow for a distinct separation of signal and idler. The signal photons are sent through a telescope to magnify the beam by a factor of 8.3, followed by $N = 2$ sets of LOV prism pairs. This configuration prepares a lattice of spin-orbit states where one of the polarization states is coupled to $\ell = 1$. Higher values of ℓ may be achieved by employing a setup with more LOV prism pairs, while negative values of ℓ may be achieved by changing the input polarization state [5].

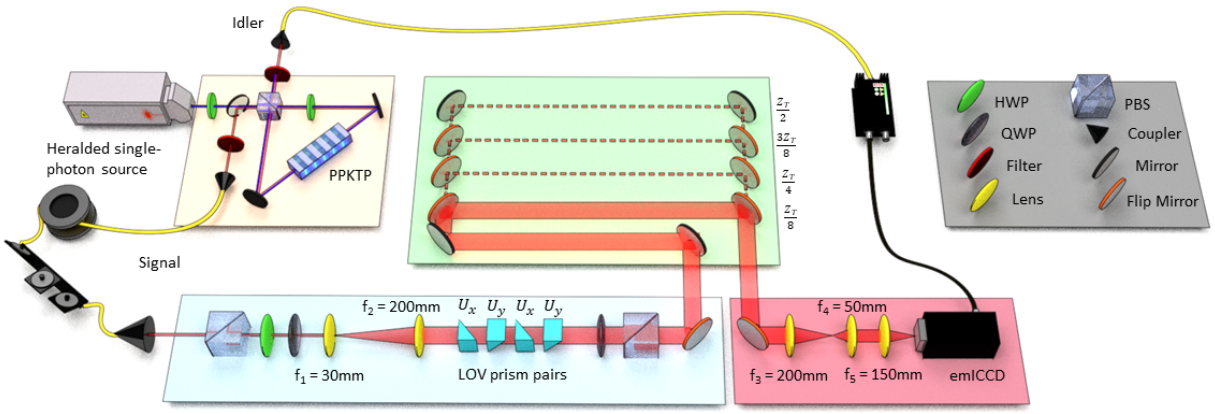

Figure 3.5: Schematic of the experimental setup. Correlated photon pairs are generated via type-II spontaneous parametric down-conversion in a Sagnac interferometer and coupled into single mode fibers (SMF). A singles rate of 18 kHz and a coincidence rate of 1.5 kHz are measured after the SMF. After propagating through a 30 m long fiber, the signal photon is sent through a telescope with 8.3x magnification, $N = 2$ sets of LOV prism pairs, and a polarization filter. The free-space propagation z, can be varied via different flip mirror combinations. The signal photons are then imaged onto an intensified electron-multiplying CCD (emICCD), triggered by the detection of the corresponding idler. The imaging arrangement in the detection unit consists of a telescope with 4x demagnification (f_3 and f_4 lenses) followed by a single-lens (f_5) that images the beam onto the detection plane of the emICCD.

The polarization state of the signal photon is prepared using a manual fiber polarization controller, polarizing beamsplitter (PBS), half wave plate (HWP) and quarter wave plate (QWP). After transmission through the LOV prism pairs, the signal is filtered with respect to left-handed or right-handed circulary polarized light using a QWP and PBS. The free-space propagation of the OAM lattice is then analyzed via an arrangement of flip mirrors that effectively change the propagation distance z before measurement. The single photon detection unit consists of a telescope to demagnify the beam by a factor of 4 (f_3 and f_4 lenses in Fig. 3.5) and a gated intensified electron-multiplying CCD (emICCD PI-Max4: 1024 EMB). The telescope is followed by a single lens (f_5 lens in Fig. 3.5) which images the plane immediately following the telescope.

The idler is detected by an avalanche photodiode with no polarization filtering, which acts as a trigger for the emICCD to herald the single photon state. We use a 30 m spool of single-mode fiber to delay the detection of the signal with respect to the idler to

accommodate for the delays from the triggering electronics. We set the delay time between the idler and signal photon for each propagation distance z and use the emICCD camera to align the coincidence window of 3 ns.

In addition to the single photon setup, we couple light from a linearly polarized laser diode (central wavelength $\lambda_{LD} = 813.4$ nm) into the signal channel in order to compare images generated by single photons versus laser diode light. We measure the intensity profile using a conventional CCD camera (Coherent LaserCam-HR II) at the same positions as the single photon images captured by the emICCD.

3.6 Experimental Results

Z_{theo}	Z_{exp}	Measured SNR	Post-processed SNR
0	0.71 m	0.584	240.377
$z_T/8$	2.86 m	0.547	181.988
$z_T/4$	4.85 m	0.113	102.514
$3z_T/8$	6.87 m	0.159	126.298
$z_T/2$	8.86 m	0.259	264.755

Table 3.1: Experimental propagation distances Z_{exp} which correspond to the fractional Talbot distances Z_{theo}, and single photon signal-to-noise ratio (SNR). The SNR is given by the ratio of the average signal to the standard deviation of the background. In the third (fourth) column, we list the SNR calculated from raw (post-processed) images.

In Fig. 3.6 we present simulated and measured beam profiles at fractional Talbot distances. Although the theoretical Talbot length is $z_T = 16$ m, the propagation distances in the experimental setup were increased by a constant offset of 0.85 m in order to account for the three lens system in the detection unit [163]. Table 3.1 lists the experimental distances, Z_{exp}, which effectively correspond to the theoretical distances, Z_{theo}. The diode images were also measured at distances $z \in Z_{\text{exp}}$. The central wavelength difference of $|\lambda_{LD} - \lambda_{SP}| = 2.6$ nm corresponds to a change in Talbot length z_T of only ~ 5 cm. The LOV prisms were realigned in the transverse plane to obtain the most pronounced doughnut structures with the diode laser.

The observed intensity profiles are measured with a total exposure time of about 1 hour and are processed using background subtraction and an adaptive two-dimensional Gaussian

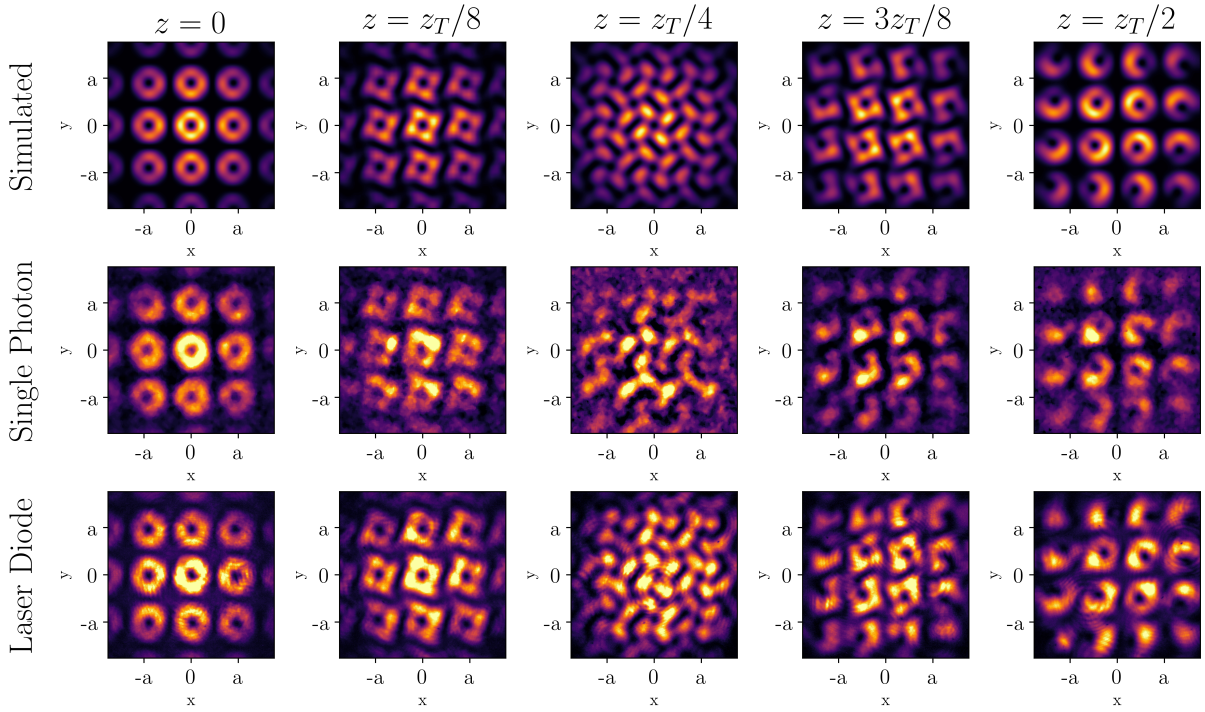

Figure 3.6: Simulated and experimental self-images at different fractional Talbot lengths. We measure the two-dimensional intensity profile $I(x, y) = |\langle L \left| \Psi_{\mathrm{LOV}}^{N=2} \right\rangle|^2$ at positions $z \in Z_{\mathrm{exp}}$. In the simulation, we multiply a Gaussian beam envelope with the same beam waist w_0 as in the experiment (i.e., $w_0 = (4.1 \pm 0.05)$ mm) to account for features occurring due to finite beam sizes when propagating along the z-axis. For comparison, we couple light from a laser diode into the signal channel, and measure corresponding self-images at the same positions. Good qualitative agreement is found between the simulated and observed profiles. We measure a lattice spacing of $a_{\mathrm{exp}} = (0.573 \pm 0.012)$ mm which corresponds to (2.229 ± 0.037) mm before the demagnification by the three lens system in the detection unit. From the simulation, we extract a lattice spacing of $a_{\mathrm{sim}} = (0.577 \pm 0.010)$ mm and (2.301 ± 0.031) mm, respectively.

image filter. Including the quadratic phase profiles of the imaging lenses in the simulation yields good agreement between theoretical and observed lattice spacing. For instance, in the case of single photons, we extract from the transverse intensity distribution at $z =$ 0.071 m a separation between two nearest-neighbor lattice sites of $a_{\mathrm{exp}} = (0.573 \pm 0.012)$ mm from experimental data and $a_{\mathrm{sim}} = (0.577 \pm 0.010)$ mm from the simulation. Additionally, at half Talbot distance $z_T/2$, the expected half period shift Δa can be evaluated by comparing

the effective pixel positions of the lattice sites at propagation distance $z = 0.071$ m with the pixel positions at $z = z_T/2$ yielding $\Delta a_{\text{exp}} = (0.273 \pm 0.015)$ mm and $\Delta a_{\text{sim}} = (0.279 \pm 0.014)$ mm, respectively.

The robustness of the Talbot Effect with a lattice of OAM states is demonstrated by the good qualitative agreement between simulation, single photon, and diode laser images in Fig. 3.6. The SNR decreases with larger distances, but is increased again depending on the intensity pattern complexity. In Table 3.1, we present the SNR before and after the imaging post-processing for different propagation distances. However, it can be noted that the self-imaging property of this beam can be seen clearly in the similarity between images taken at distances $z = \{0, z_T/2\}$, with the correct spatial shift. Images at $z = \{z_T/8, 3z_T/8\}$ show an orientation about each lattice site that appears counter-clockwise in $z_T/8$ and clockwise in $3z_T/8$. These features are indicative of the OAM state in each lattice site, as shown in Fig. 3.3(c). Furthermore, gaps in the outermost rings of the $z_T/2$ image can be mitigated by using a beam containing more lattice sites.

3.7 Conclusion

In this work we demonstrated and analyzed the Talbot Effect with single photons prepared in a lattice of OAM states. Heralded single photons are sent through $N = 2$ sets of LOV prism pairs and their transverse two-dimensional intensity distribution are measured at various fractional Talbot lengths. The propagation of structured wavefronts is calculated in the near-field and shows good agreement with experimental results. We observe that the initial phase profile defines the transverse intensity pattern at various propagation distances, and thus the Talbot carpet. Future work will scrutinize the connection between OAM and Talbot physics as a new characterization tool. Another avenue of exploration includes the addition of path entangled OAM lattices using the Talbot Effect and the OAM degree of freedom. Path entangled OAM lattices could also be used to preform quantum logic using the Talbot Effect and the OAM degree of freedom.

Chapter 4

Remote State Preparation of Single-Photon Orbital-Angular-Momentum Lattices

Notes and Acknowledgements

The contents of this chapter were published on November 22, 2021, as [164]:

Andrew R. Cameron, Sandra W. L. Cheng, Sacha Schwarz, Connor Kapahi, Dusan Sarenac, Michael Grabowecky, David G. Cory, Thomas Jennewein, Dmitry A. Pushin, and Kevin J. Resch, Phys. Rev. A **104**, L051701 (2021).

Author Contributions

Kevin Resch, **Thomas Jennewein**, **Dmitry Pushin**, and **David Cory** conceived of the study.
Connor Kapahi, **Dusan Sarenac**, and **Michael Grabowecky** helped implement the theory and general strategy.
Andrew Cameron, **Sandra Cheng**, and **Sacha Schwarz** built the experiment and took experimental results.
Andrew Cameron and **Sandra Cheng** lead the manuscript writing.
All authors contributed to the final version.

4.1 Chapter Overview

Optical beams with periodic lattice structures have broadened the study of structured waves. In the present work, we generate spin-orbit entangled photon states with a lattice structure and use them in a remote state preparation protocol. We sequentially measure spatially-dependent correlation rates with an electron-multiplying intensified CCD camera and verify the successful remote preparation of spin-orbit states by performing pixel-wise quantum state tomography. Control of these novel structured waves in the quantum regime provides a method for quantum sensing and manipulation of periodic structures.

4.2 Context

Advances in experimental methods have enabled the creation of structured beams of neutrons [165]. Matter-waves with structured phase fronts are formed with many different strategies ranging from spatially-dependent magnetic fields [166, 159, 167] to spiral phase plates made of thin graphite films [168]. The formalism of quantum information science is system agnostic, allowing translation of the physics of one system to that of another. In order to move from neutrons to photons, spin is replaced with polarization, and the magnetic field gradients are replaced with birefringent gradients shown in Fig. 3.2. Using this correspondence, a lattice of spin-orbit states originally developed for neutrons has been implemented with photons. Optical lattices have led to studies of optical Talbot physics of structured orbital angular momentum (OAM) light beams [169, 110], optical lattice structure shaping [170, 171], and direct detection of optical spin-orbit states by the human eye [140, 141]. By translating the physics of a periodic structure of spin-orbit states further in photonics, we can take advantage of additional capabilities such as multi-particle entanglement. This opens the possibility for *quantum* correlations in structured beams and the capabilities that come with them.

The periodicity of these structured waves are suited for quantum sensing or control of periodic structures [138, 134, 172]. The interference of OAM lattices has been used to build all-optical quantum memory devices [173], and the average deviation of atoms relative to their lattice sites has been measured continuously and nondestructively with optical lattices [174]. OAM provides access to a high-dimensional Hilbert space which can enhance the information capacity of a single particle [175, 176], while the more easily manipulated polarization degree of freedom can be used for enhanced control and measurement [177, 178, 179, 180, 2, 181, 182]. Working with the OAM and polarization degrees of freedom simultaneously combines the advantageous characteristics

of both [183, 184, 185, 186, 187, 188]. To characterize and verify spin-orbit entanglement, quantum state tomography has been done previously using OAM projective measurements with a spatial light modulator [189], and with spatially-dependent polarization measurements using an intensified CCD camera [190]. Structured waves have recently attracted attention in the quantum communication community specifically in turbulence studies [191, 192]. Correlations between polarization and OAM have shown preservation of the encoded state after propagation through scattering media [193].

In this work, we generate spin-orbit entanglement between the polarization of one photon and the transverse beam profile of the other. Polarization measurement enables production of distinctly different structured beams, and the correlations between these beams and the polarization can be used to verify entanglement. We confirm the entanglement using a quantum state tomography procedure between the polarization of one photon, and the position-dependent polarization of its entangled partner. With these correlations, we implement a remote state preparation (RSP) protocol to prepare structured single photon beams. RSP involves transferring a quantum state known by one party to another party via entanglement [194, 195, 196], and has applications in large-scale quantum communication networks [197, 198, 153, 199]. In our case, a RSP protocol is used to prepare signal photon spatial patterns conditioned on idler photon polarization measurements. The spin-orbit coupling method presented expands lattice structured light preparation and measurement further into the quantum regime.

4.3 Concept and Theory

We consider polarization-entangled photon pairs which are described by the Bell state $|\Phi^+\rangle = \frac{1}{\sqrt{2}}(|LR\rangle + |RL\rangle)$, where we denote right-handed circular and left-handed circular polarization states by $|R\rangle = \frac{1}{\sqrt{2}}(|H\rangle + i|V\rangle)$ and $|L\rangle = \frac{1}{\sqrt{2}}(|H\rangle - i|V\rangle)$. Polarization states $|H\rangle$ and $|V\rangle$ correspond to $|0\rangle$ and $|1\rangle$, respectively, in the computational basis. As described in Ref. [5] in more detail, a lattice of spin-orbit states is obtained by passing circularly polarized light through perpendicular pairs of birefringent linear gradients whose optical axes are relatively offset by 45°. The operators of the two perpendicular birefringent gradients are described by

$$\hat{U}_x = e^{i\frac{\pi}{a}(x-x_0)\hat{\sigma}_x}, \quad \hat{U}_y = e^{i\frac{\pi}{a}(y-y_0)\hat{\sigma}_z}, \tag{4.1}$$

where the origin of the gradients is given by (x_0, y_0), $\hat{\sigma}_{x,z}$ are Pauli matrices and $a = \lambda(\Delta n \tan(\theta))^{-1}$ is the spacing between neighboring lattice sites with wavelength λ, prism

birefringence Δn and prism incline angle θ. By sending one photon through $N = 2$ sets of *Lattice of Optical Vortices* (LOV) prism pairs, we prepare the spin-orbit entangled lattice state

$$|\Psi_{\text{LOV}}^{N=2}\rangle(x, y) = \frac{\alpha(x, y)}{\sqrt{2}} \left[(\hat{U}_x \hat{U}_y)^2 \otimes \mathbb{I}_2\right] |\Phi^+\rangle, \tag{4.2}$$

where $\alpha(x, y)$ describes the incoming Gaussian beam envelope, and $\mathbb{I}_2$ is the two-dimensional identity matrix.

Applying the operators in Eq. 4.1 on the polarization state $|R\rangle$ yields

$$(\hat{U}_x \hat{U}_y)^2 |R\rangle = A(x, y)|R\rangle + B(x, y)|L\rangle, \tag{4.3}$$

where $A(x, y)$ and $B(x, y)$ are complex-valued amplitudes. The LOV prism pairs are thus represented by unitary matrices that couple the polarization of a photon to its spatial mode. Different polarization projections on the spin-orbit lattice state lead to different intensity patterns. To simulate these intensity patterns, polarization projections were applied to Eq. 4.2. Furthermore, we applied a Gaussian beam profile to the theoretical images in order to account for the beam intensity envelope.

The two-photon density matrix is recovered via maximum likelihood quantum state tomography. The information of interest is encoded in the complex two-dimensional spatial functions as seen in Eq. 4.3, and a single photon camera captures intensity measurements of the entire pattern simultaneously. Each of the camera's pixels are treated like individual detectors when computing tomography. A pixel-wise algorithm loops through them and uses the maximum likelihood tomography approach specified in Ref. [71]. By recovering the density matrix at every pixel, we can witness entanglement between polarization and each transverse position in the beam and verify remote state preparation.

4.3.1 Remote State Preparation

Remote state preparation is a quantum communication protocol that requires shared entanglement between two parties. Like quantum teleportation, the goal is to transmit one instance of a quantum state by forwarding classical information to the receiver [195]. Remote state preparation and quantum teleportation differ by whether or not the instance of the quantum state being transmitted is known by the sender. In a teleportation experiment, the sender may transmit an instance of a quantum state without knowledge of which state is being "teleported", while in remote state preparation, the sender is specifically targeting a particular quantum state.

In our experiment, the quantum information being transmitted is stored in the polarization of the photons. A polarization measurement is made on the idler photon to specifically prepare a known polarization state on the entangled signal photon. The outcome of this measurement is forwarded to an emICCD camera to gate the measurement in time and schedule the camera to take a picture. Different polarization measurements on the idler photon remotely prepare different states on the signal photon. The resultant spatial mode of the signal photon after propagation through the LOV prism pairs is polarization dependent, so the spatial mode of the signal photon is therefore remotely prepared by polarization measurements on the idler photon. The complex spatial modes prepared by different polarization measurements are presented in Sec. 4.5.

4.4 Experimental Setup

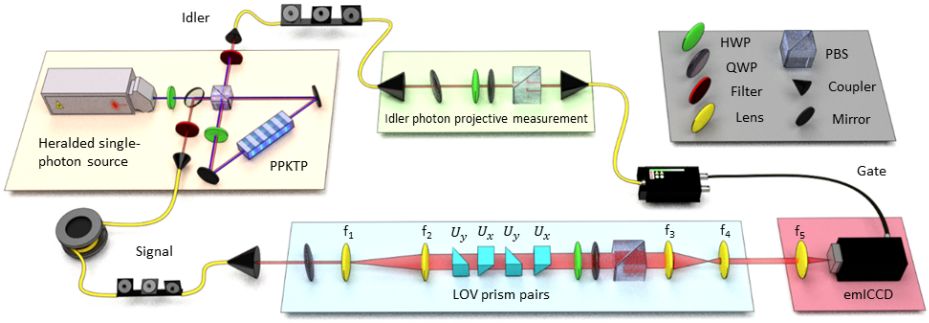

Figure 4.1: Schematic of the experimental setup. Polarization-entangled photon pairs are generated via type-II spontaneous parametric down-conversion in a Sagnac interferometer and coupled into single mode fibers. After propagating through a 30 m fiber, the signal photon is sent through a telescope with 8.3× magnification (f_1 and f_2 lenses), two sets of "Lattice of Optical Vortices" (LOV) prism pairs and polarization analyzing optics. The signal photons are then gated to an electron-multiplying intensified CCD (emICCD) camera, triggered by the detection of the corresponding polarization-filtered idler. The imaging arrangement in the detection unit consists of a telescope with 4× demagnification (f_3 and f_4 lenses) followed by a lens (f_5) that images the beam onto the detection plane of the emICCD camera.

A schematic of our experimental setup is depicted in Fig. 4.1. We generate entangled photon pairs using type-II spontaneous parametric down-conversion in a Sagnac interfer-

ometer [110]. We pump a 10 mm long periodically-poled potassium titanyl phosphate crystal (ppKTP) with a 404 nm continuous wave diode laser to produce signal and idler photon pairs, both centered at 808 nm with a spectral bandwidth (FWHM) of approximately 0.4 nm. The outputs of the interferometer are coupled into single-mode fibers. Immediately following the polarization-entangled source, we measured a $|\Phi^+\rangle$ polarization state fidelity of 96%. The signal photons are first sent through an optical telescope to be magnified by a factor of 8.3, followed by two sets of LOV prism pairs. The magnification controls the number of lattice periods in the emerging intensity pattern by illuminating a larger portion of the prisms.

The modified signal photons are sent through polarization analyzing optics which consist of a half-wave plate (HWP), a quarter-wave plate (QWP) and a polarizing beam splitter (PBS). Finally, we demagnify the beam by a factor of 4 by means of a second optical telescope and send the signal photons to an emICCD camera (PI-Max4: 1024 EMB). The idler photons are directly sent to polarization analyzing optics and detected by an avalanche photodiode which triggers the emICCD. Signal photons pass through a 30 m spool of single-mode fiber in order to compensate for electronic delay. Once the idler photon triggers the camera, an electronic gate in the emICCD collects data for 3 ns. We measure all 16 combinations of the tomographically complete set $|H\rangle$, $|V\rangle$, $|D\rangle$, and $|R\rangle$ on the signal and idler photons. For each polarization measurement, we accumulate signal photons for 2000 exposures and trigger the camera at a rate of 15 kHz. Every exposure takes about 2.35 sec to record. We focus on a 140×140 pixel area on the camera, where each pixel is 13 μm $\times$13 μm.

4.5 Experimental Results

In Fig. 4.2, we show a comparison of theoretically calculated and experimentally measured two-dimensional intensity patterns for all 16 measurement configurations. The theoretical predictions in Fig. 4.2(a) and the experimental data in Fig. 4.2(b) are in qualitative agreement. LOV prism pair alignment challenges associated with setting and maintaining the phase leads to slight pattern distortion as compared with theory. In both cases, we used a grid of 140×140 points. In the image plane of the emICCD, the simulated lattice spacing in Fig. 4.2(a) is 0.519 ± 0.015 mm, while the measured lattice spacing in Fig. 4.2(b) is 0.522 ± 0.013 mm. For the purpose of computing the density matrices, the raw counts from the sum of exposures are used. However, when viewing the intensity distributions, the raw intensity profiles are post-processed using background subtraction and an adaptive two-dimensional Gaussian image filter.

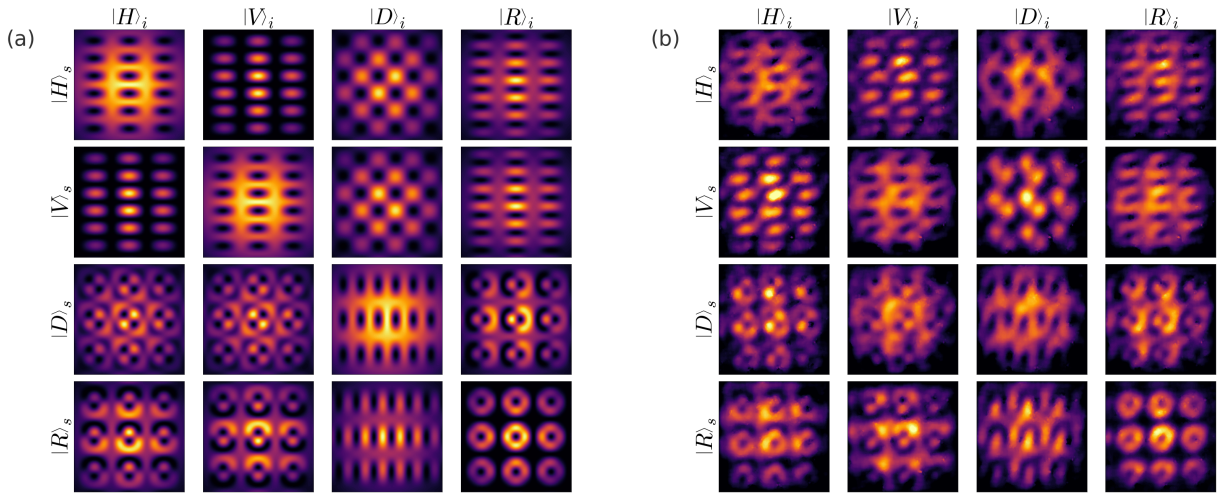

Figure 4.2: Theoretical predictions and experimental results. Rows (columns) are organized by signal (idler) projective measurements labeled by the corresponding polarization. (a) Theoretical evaluation of the 16 measurement configurations over a 140×140 grid. (b) Experimental results of the 16 measurement configurations over a 140×140 pixel area. All theoretical intensity patterns are normalized and all experimental intensity patterns are normalized and post-processed using background subtraction and an adaptive two-dimensional Gaussian image filter. The emICCD camera records photon counts, and an artificial color scheme representing intensity was used for visual clarity.

We take the theoretical (Fig. 4.3(a)) and experimental (Fig. 4.3(b)) density matrices calculated at each position and present the fidelity with each of the four Bell states. For example, the top left image in Fig. 4.3(a) shows how similar the theoretical density matrices, $\rho(x, y)$, are to the $|\Phi^+\rangle$ Bell state by plotting the fidelity, $F(x, y) = \mathrm{Tr}(\rho(x, y)|\Phi^+\rangle\langle\Phi^+|)$, at every pixel position (x, y). The input to the LOV prism pairs is the $|\Phi^+\rangle$ Bell state as shown in Eq. 4.2, and you can see from the top left images in Fig. 4.3(a) and Fig. 4.3(b) that the areas around the ring-shaped regions, along with the centre of these regions, have had a phase rotation of a multiple of 2π from the starting $|\Phi^+\rangle$ Bell state. Looking at the four quadrants of Fig. 4.3(a) and Fig. 4.3(b), it is apparent that at different pixel positions, the input state has been rotated to other Bell states. Pixel-wise quantum state tomography therefore enables a visualization technique to show how the spin-orbit lattice state evolves across the transverse beam profile. The theoretical and experimental Bell state fidelities plotted in Fig. 4.3 are in qualitative agreement, and there is a reduced experimental fidelity across all pixels.

A histogram presenting the highest Bell state fidelity at each pixel position is presented

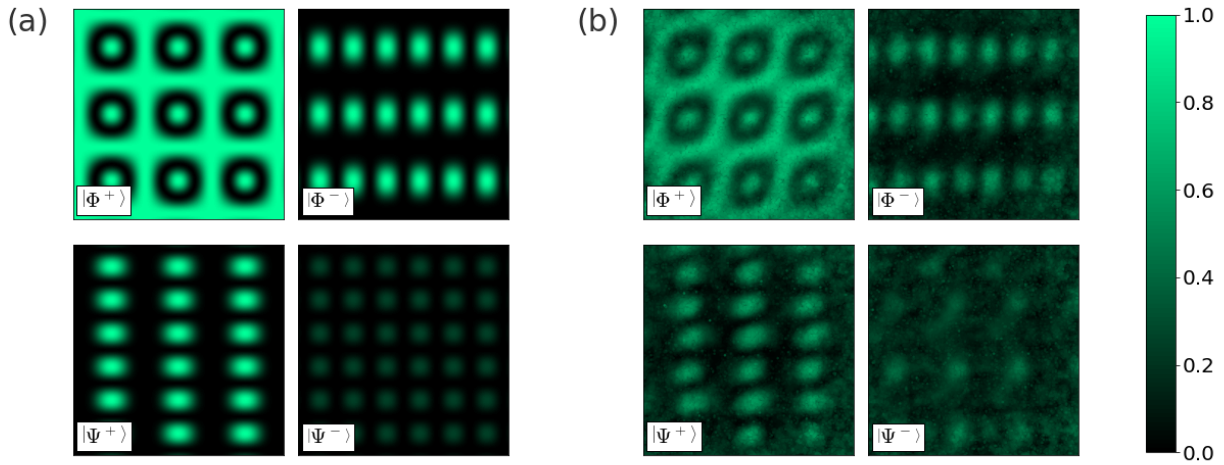

Figure 4.3: Plots of pixel-wise maximum likelihood tomography by means of the fidelity of all four Bell states. (a) Tomography seeded with simulated intensity distributions shown in Fig. 4.2(a). (b) Tomography seeded with experimental intensity distributions shown in Fig. 4.2(b). In both cases, $|\Phi^+\rangle$, $|\Phi^-\rangle$, $|\Psi^+\rangle$, and $|\Psi^-\rangle$ Bell state fidelities are shown. There is good qualitative agreement between experiment and theory, with a reduced experimental fidelity overall.

in Fig. 4.4. In the experimental case, 42.5% of pixel locations have a fidelity of more than 0.5 with one of the four Bell states. This is a witness of entanglement between the signal photons measured at the pixel locations and the idler photons that trigger the camera because qubit separable states cannot achieve a Bell state fidelity of more than 0.5 [200]. In the theoretical case, 85.7% of pixel locations are a witness of entanglement in this way, so even with perfect image contrast and quantum state preparation, not all positions of this pattern significantly overlap with one of the four Bell states. However, plotting Bell state fidelities helps to illustrate the spatially-dependent rotation of the two-photon spin-orbit lattice state. White noise of the form $\rho_{\text{noise}} = \Lambda\rho_{\text{theory}} + \frac{1}{4}(1-\Lambda)\mathbb{I}_4$ can be introduced to model the discrepancies between the total number of entangled pixels in the theoretical and experimental density matrix reconstructions. When $\Lambda = 0.4$, the percent of pixel locations exhibiting entanglement drops to the experimentally realized 42.5%. We attribute the difference to be a consequence of prism alignment, detection noise, and imperfect input polarization entanglement.

Another common measure of entanglement used for experimental bipartite systems is concurrence, $\mathcal{C}$. It can be calculated as $\mathcal{C} = \max\{\lambda_1 - \lambda_2 - \lambda_3 - \lambda_4, 0\}$, where λ_i are the

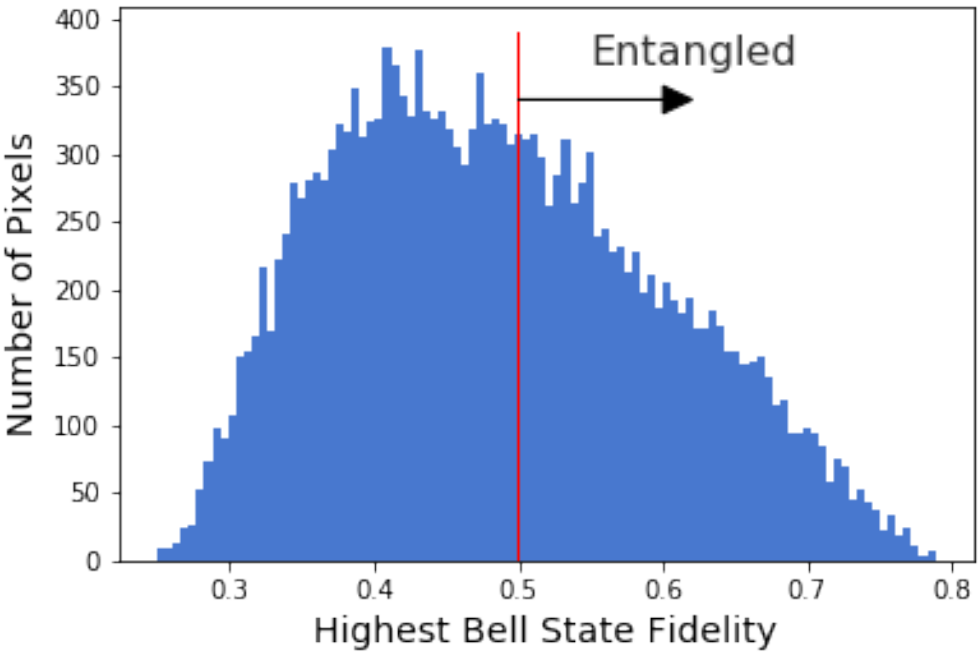

Figure 4.4: Histogram of the highest Bell state fidelity over all pixel positions. A red line is overlaid at 0.5 fidelity. All pixels with a fidelity greater than 0.5 with one of the four Bell states are definitely entangled. Using this metric, 42.5% of all pixels in the camera's region of interest are entangled.

square roots of the eigenvalues of the matrix $\rho\tilde{\rho}$, $\tilde{\rho} = (\sigma_y \otimes \sigma_y)\rho^*(\sigma_y \otimes \sigma_y)$, and ρ is the two photon density matrix [201]. Concurrence was calculated at every pixel location which resulted in an average value of 0.272 in the experimental data. This is further proof of entanglement because a concurrence greater than zero is not possible for a separable state, and verifies successful remote state preparation.

4.6 Conclusion

In this work, we report on the implementation of a remotely prepared optical lattice of spin-orbit states by means of polarization-entangled photon pairs. We experimentally verify the successful remote preparation of this spin-orbit entangled state with an emICCD camera using a pixel-wise maximum likelihood quantum state tomography algorithm. We observe that the entanglement present in the joint two-photon quantum state transforms such

that there are overlaps with different Bell states depending on which portion of the LOV prism pairs the signal photon travels through. Furthermore, we have shown that pixel-wise tomography on images acquired by an emICCD camera provides a useful method for observing spatially-dependent two-photon states.

In future work, we plan to study lattices with a higher number of LOV prism pairs to access higher radial quantum numbers and thus a larger alphabet to encode spin-orbit states for quantum communication protocols. Our work advances the study of quantum correlations of structured beams with lattice frameworks, as well as quantum sensing and control of periodic structures where we can take advantage of the novel lattice patterns of our spin-orbit states.

Chapter 5

Ultrafast Measurement of Energy-Time Entanglement with an Optical Kerr Shutter

Notes and Acknowledgements

The contents of this chapter were submitted for publication on May 23, 2023, as [202]:

Andrew R. Cameron, Kate L. Fenwick, Sandra W. L. Cheng, Sacha Schwarz, Benjamin MacLellan, Philip J. Bustard, Duncan England, Benjamin Sussman, and Kevin J. Resch, arXiv:2305.14498 [quant-ph] (2023).

Author Contributions

Kevin Resch and **Benjamin Sussman** conceived of the study.
Philip Bustard, **Duncan England**, **Benjamin MacLellan**, and **Sacha Schwarz** helped implement the theory and general strategy.
Andrew Cameron, **Kate Fenwick**, and **Sandra Cheng** built the experiment and took experimental results.
Andrew Cameron and **Kate Fenwick** wrote the first draft of the manuscript.
All authors contributed to the final version.

5.1 Chapter Overview

Recent experimental progress in quantum optics has enabled measurement of single photons on ultrafast timescales, beyond the resolution limit of single photon detectors. The energy-time degree of freedom has emerged as a promising avenue for quantum technologies, as entanglement between the frequency and temporal properties of two photons can be fully explored and utilized. Here, we implement optical Kerr shutters in single mode fibers to map out the sub-picosecond correlations of energy-time entangled photon pairs. These measurements, in addition to joint spectral measurements of the photon pair state, are used to verify entanglement by means of the violation of a time-bandwidth inequality.

5.2 Context

The energy-time degree of freedom is important for many quantum technologies, including quantum networks [203, 204], optical quantum computers [205], and quantum sensing [206]. This degree of freedom is useful due to its intrinsic robustness against decoherence for long-distance transmission of quantum information [207], increasing imaging resolution via interferometric techniques [208], and for realizing high-dimensional entangled quantum states [209]. Energy-time entangled pairs of ultrafast photons (femtosecond-picosecond duration) are challenging to control and measure with sufficient resolution. Measuring in the sub-picosecond regime is particularly important because there has yet to be a single photon detector with comparable resolution. The highest detector resolution to date has been demonstrated with superconducting nanowire single-photon detectors (SNSPD), which have seen timing resolution on the order of a few picoseconds to tens of picoseconds, depending on the photon's frequency [210, 211].

Fast gating of optical signals is commonly performed electronically by micromechanical switches [212, 213] or electro-optic modulators [214] on nanosecond timescales. Optical gating has been used to surpass these timing restrictions, with resolutions of 450 ps in ring resonators [215], 10 ps in nonlinear optical loop mirrors [97], and sub-picosecond with sum-frequency generation (SFG) [216]. Optical gating is paramount in the detection and control of sub-picosecond energy-time-entangled photon pairs [101]. SFG optical gating has been used for time-resolved detection of energy-time entangled photon pairs [217], which can exhibit correlations in time on the order of a few femtoseconds. SFG temporal measurements have been taken alongside spectral measurements to completely reconstruct a two-photon joint spectral amplitude [102].

A promising alternative method for ultrafast optical gating is to use an optical Kerr shutter (OKS) [94]. This method relies on the optical Kerr effect which, unlike $\chi^{(2)}$ effects as shown in Sec. 2.3.2, can occur in any material, including those which are centrosymmetric. This makes it suitable for integration in standard single-mode fiber (SMF), where spatial overlap between the signal and pump is easy to achieve. In an OKS, the transient birefringence induced by a strong laser pulse will rotate the polarization of a photon pulse only where the two pulses temporally overlap in the Kerr medium. Picosecond and sub-picosecond Kerr gating has been shown for classical applications, such as optical communications [218, 219, 220]. Previous demonstrations for quantum applications have shown near-unit efficiency operation of the Kerr shutter in YAG crystal [221] and short (10 cm) pieces of SMF on picosecond timescales [222, 223, 224, 225]. In these cases, the group velocity walk-off between the signal and pump in the SMF was exploited to fully switch the polarization qubit of a single photon for quantum communication and information applications. Operation with a photon and pump pulse close in wavelength reduces walk-off and has been used to demonstrate Kerr shutter resolution as low as 305 fs [226]; however, this operation regime introduces noise from pump self-phase modulation and cannot easily be operated above 30% efficiency. Walk-off reduction has also been implemented using photonic crystal fiber (PCF) as the $\chi^{(3)}$ medium to match the group velocities of both pulses [227].

In this work, we implement an OKS for each entangled photon and demonstrate fast gated measurements with 320 ± 30 fs and 290 ± 30 fs resolution for the signal and idler photons, respectively. We characterize photon-pair correlations in time without the need for an interferometric setup. Unlike previous experiments using SFG for optical gating, no frequency conversion of the photons is required and the only difference between switched and unswitched photons is their polarization. Here, we use this polarization rotation to measure time correlations; however, polarizing optics after an OKS could easily be used to reroute photons with sub-picosecond resolution for use in other quantum information protocols.

5.3 Concept and Theory

In the following sections, the uncertainty relations between frequency and time-of-arrival are presented. First, a classical treatment of electromagnetic pulses and the limits placed on their uncertainties in time and frequency are analysed, followed by a description of similar uncertainty relations between separable single photons. This motivates the use of uncertainty relations, specifically the time-bandwidth inequality, as a metric for verifying

energy-time entanglement.

5.3.1 Time-Bandwidth Inequality for classical pulses

If light is exactly monochromatic, the time it reaches a detector is totally uncertain. On the other hand, if light's time of arrival is known with infinite precision, its frequency is totally uncertain. In realistic experimental scenarios, neither of these cases are exactly realized. Instead, light is usually described by a coherence time, Δt, and this necessarily imparts an uncertainty of its frequency. These two variables are conjugates and linked together by the Fourier transform. Similar uncertainty relationships are seen in other areas of physics where two properties are conjugate to each other, such as position and momentum. To quantify the uncertainty relationships, a definition of distribution width is required. There are many [1] common widths to choose from [78], including the full-width at half maximum (FWHM), the half-width-$1/e$, and the root-mean-squared width, to name a few. For the following derivation, we'll consider the root-mean-squared width. This quantity is the second-order moment of the mean arrival time, and is also called standard deviation. The standard deviation of the temporal distribution of a classical pulse is

$$\begin{aligned}\Delta t_{\text{std}} = \sigma_t &\equiv \sqrt{\langle t - \langle t\rangle\rangle^2} \\ &= \sqrt{\langle t^2\rangle - 2\langle t\rangle^2 + \langle t\rangle^2} \\ &= \sqrt{\langle t^2\rangle - \langle t\rangle^2},\end{aligned} \tag{5.1}$$

where the expected value is carried out via the integral

$$\langle t^n\rangle \equiv \int_{-\infty}^{\infty} dt (t^n) |E(t)|^2, \tag{5.2}$$

and $|E(t)|^2$ is normalized. Similarly, the standard deviation definition of spectral width is given by

$$\sigma_\omega = \sqrt{\langle \omega^2\rangle - \langle \omega\rangle^2}, \tag{5.3}$$

[1] Rick Trebino notes this in the "Frequency Resolved Optical Gating" textbook and it stuck with me. He muses that even the names haven't been standardized. Pulse length, pulse width, spectral width (but never spectral length for some reason), are measured with different definitions.

where

$$\langle \omega^n \rangle \equiv \frac{1}{2\pi} \int_{-\infty}^{\infty} d\omega (\omega^n) |E(\omega)|^2, \tag{5.4}$$

and $E(\omega)$ is the Fourier transform of $E(t)$. The bandwidth theorem, commonly studied in signal processing and electrical engineering, says that a classical pulse has a minimum bandwidth product of 1/2. Mathematically, this theorem is stated as

$$\Delta\omega \Delta t \geq \frac{1}{2}. \tag{5.5}$$

The proof of the bandwidth theorem follows. Assume $E(t)$ is differentiable and $\lim_{t\to\pm\infty} t|E(t)|^2 = 0$. Without loss of generality, take $t_0 = 0$ and $\omega_0 = 0$. Parseval's theorem states that

$$\int_{-\infty}^{\infty} |E(t)|^2 dt = \frac{1}{2\pi} \int_{-\infty}^{\infty} |E(\omega)|^2 d\omega, \tag{5.6}$$

where $E(\omega)$ is the Fourier transform of $E(t)$. Differentiation in the time domain corresponds to multiplication of $i\omega$ in the frequency domain, written as

$$\mathcal{F}\left(\frac{dE(t)}{dt}\right) = i\omega E(\omega). \tag{5.7}$$

Applying Parseval's theorem to this new Fourier pair gives

$$\int_{-\infty}^{\infty} \left|\frac{d}{dt} E(t)\right|^2 dt = \frac{1}{2\pi} \int_{-\infty}^{\infty} \omega^2 |E(\omega)|^2 d\omega. \tag{5.8}$$

We can now evaluate the product

$$\begin{aligned} \Delta t^2 \Delta\omega^2 &= (\langle t^2 \rangle - \langle t \rangle^2)(\langle \omega^2 \rangle - \langle \omega \rangle^2) \\ &= \langle t^2 \rangle \langle \omega^2 \rangle \\ &= \int_{-\infty}^{\infty} t^2 |E(t)|^2 dt \frac{1}{2\pi} \int_{-\infty}^{\infty} \omega^2 |E(\omega)|^2 dt. \end{aligned} \tag{5.9}$$

Substituting Eq. 5.8 to Eq. 5.9 gives

$$\begin{aligned}\Delta t^2 \Delta\omega^2 &= \int_{-\infty}^{\infty} t^2 |E(t)|^2 dt \int_{-\infty}^{\infty} \left| \frac{d}{dt} E(t) \right|^2 dt \\ &\geq \left| \int_{-\infty}^{\infty} tE^*(t) \frac{d}{dt} E(t) dt \right|^2\end{aligned} \tag{5.10}$$

where the inequality was introduced via the *Cauchy-Schwarz inequality* for complex valued functions, which states that

$$\left| \int_{-\infty}^{\infty} f^*(x) g(x) dx \right|^2 \geq \int_{-\infty}^{\infty} |f(x)|^2 \int_{-\infty}^{\infty} |g(x)|^2. \tag{5.11}$$

The integral in Eq. 5.10 can be solved via integration by parts as

$$\begin{aligned}\Delta t^2 \Delta\omega^2 &\geq \left| \int_{-\infty}^{\infty} tE^*(t) \frac{d}{dt} E(t) dt \right|^2 \\ &= \left| \frac{1}{2} \int_{-\infty}^{\infty} t \frac{d}{dt} |E(t)|^2 dt \right|^2 \\ &= \left| \frac{1}{2} \left(t|E(t)|^2 \Big|_{-\infty}^{\infty} - \int_{\infty}^{\infty} |E(t)|^2 dt \right) \right|^2 \\ &= \left| \frac{-1}{2} \right|^2 \\ &= \frac{1}{4}.\end{aligned} \tag{5.12}$$

The proof is finished by taking the square root of both sides,

$$\Delta t \Delta\omega \geq \frac{1}{2}. \tag{5.13}$$

In addition to optical pulses, the bandwidth inequality is true of all signals related by the Fourier transform [228]. The minimum value of this uncertainty relation is achieved when the electric fields in frequency and time are represented by Gaussian functions. A Gaussian pulse amplitude and intensity has the form

$$E(\omega) = e^{\frac{-(\omega-\omega_0)^2}{4\sigma_\omega^2}} \qquad |E(\omega)|^2 = e^{\frac{-(\omega-\omega_0)^2}{2\sigma_\omega^2}}, \tag{5.14}$$

where $\Delta\omega = \sigma_\omega$ is the standard deviation width. Fourier transforming to represent the pulse in time results in a Gaussian with width

$$\Delta t = \frac{1}{2\sigma_\omega}. \tag{5.15}$$

Together, substituting these widths into the bandwidth product gives $\Delta t \Delta\omega = 1/2$. Note, different definitions of width provide different bandwidth product bounds [2].

Pulses that achieve the minimum value of the bandwidth product are called transform limited pulses. Ti:Sapph lasers produce pulses that are very close to transform limited, but as soon as chromatic dispersion is applied to a Gaussian function, the pulse starts to spread out in frequency. Pulse compressors, as described in Sec. 2.6.2, are often used to keep a pulse transform limited.

5.3.2 Time-Bandwidth Inequality for separable photon-pairs

Energy-time entangled photon pairs are not described by an electric field in the same way as a classical pulse as discussed in Sec. 1.2. However, we have seen that the spectral and temporal correlations of entangled photon pairs in a pure state can be described by $F(\omega_s, \omega_i)$ and $F(t_s, t_i)$ in Sec. 2.4.5. These quantities are Fourier transforms of each other, and we will see that measurements of the widths of these functions can serve as an entanglement witness.

To setup this entanglement witness, the derivation outlined in Ref. [229] for a sufficient criterion for inseparability will be followed. A great description of this criteria is also presented in Ref. [88]. Instead of frequency and time-of-arrival, we consider the position and momentum operators of a quantum state defined by

$$\hat{u} = |a|\hat{x}_1 + \frac{1}{a}\hat{x}_2 \tag{5.16}$$

$$\hat{v} = |a|\hat{p}_1 - \frac{1}{a}\hat{p}_2 \tag{5.17}$$

[2] It is important to note that these widths correspond to the *intensity*, not the field amplitude. For standard deviation, intensity and field widths differ by a factor of $\sqrt{2}$

where $\hat{x}_1$ and $\hat{x}_2$ are the positions of two different particles, $\hat{p}_1$ and $\hat{p}_2$ are the momenta of the same two particles, a is an arbitrary nonzero real number, and the operators obey the Heisenberg uncertainty principle, $[\hat{x}_j, \hat{p}_{j'}] = i\delta_{jj'}$. Two separable particles may be represented by a separable density matrix of the form

$$\rho = \sum_i p_i \rho_{i1} \otimes \rho_{i2}. \tag{5.18}$$

Duan et al. present the following theorem for a sufficient criterion for inseparability. Separable quantum states satisfy the inequality

$$\langle (\Delta \hat{u})^2 \rangle_\rho + \langle (\Delta \hat{v})^2 \rangle_\rho \geq a^2 + \frac{1}{a^2}. \tag{5.19}$$

The proof begins by calculating the LHS and carrying out expectation values for the separable state. The first term on the LHS is given by

$$\begin{aligned}
\langle (\Delta \hat{u})^2 \rangle_\rho &= \langle \langle \hat{u}^2 \rangle - \langle \hat{u} \rangle^2 \rangle_\rho \\
&= \sum_i p_i \langle \hat{u}^2 \rangle_i - \left(\sum_i p_i \langle \hat{u} \rangle_i \right)^2 \\
&= \sum_i p_i \langle (|a| \hat{x}_1 + \frac{1}{a} \hat{x}_2)^2 \rangle_i - \left(\sum_i p_i \langle \hat{u} \rangle_i \right)^2 \\
&= \sum_i p_i \left[a^2 \langle \hat{x}_1^2 \rangle_i + \frac{a}{|a|} \langle \hat{x}_1 \hat{x}_2 \rangle + \frac{a}{|a|} \langle \hat{x}_2 \hat{x}_1 \rangle + \frac{1}{a^2} \langle \hat{x}_2^2 \rangle \right] - \left(\sum_i p_i \langle \hat{u} \rangle_i \right)^2,
\end{aligned} \tag{5.20}$$

where $\langle \dots \rangle$ represents the average over the tensor product of the separable density operator $\rho_{i1} \otimes \rho_{i2}$. Note, due to the separability of the two particles, the operators $\hat{x}_1$ and $\hat{x}_2$ commute and we can rewrite the terms involving both operators as

$$\langle \hat{x}_1 \hat{x}_2 \rangle = \langle \hat{x}_2 \hat{x}_1 \rangle = \langle \hat{x}_1 \rangle \langle \hat{x}_2 \rangle. \tag{5.21}$$

This relation is used to simplify Eq. 5.20 by

$$
\begin{aligned}
\langle(\Delta\hat{u})^2\rangle_\rho &= \sum_i p_i \left[a^2\langle\hat{x}_1^2\rangle_i + 2\frac{a}{|a|}\langle\hat{x}_1\rangle\langle\hat{x}_2\rangle + \frac{1}{a^2}\langle\hat{x}_2^2\rangle\right] - \left(\sum_i p_i\langle\hat{u}\rangle_i\right)^2 \\
&= \sum_i p_i \left[a^2\left(\langle(\Delta\hat{x}_1)^2\rangle_i + \langle\hat{x}_1\rangle_i^2\right) + 2\frac{a}{|a|}\langle\hat{x}_1\rangle\langle\hat{x}_2\rangle + \frac{1}{a^2}\left(\langle(\Delta\hat{x}_2)^2\rangle_i + \langle\hat{x}_2\rangle_i^2\right)\right] \\
&\quad - \left(\sum_i p_i\langle\hat{u}\rangle_i\right)^2 \\
&= \sum_i p_i \left[a^2\langle(\Delta\hat{x}_1)^2\rangle_i + \frac{1}{a^2}\langle(\Delta\hat{x}_2)^2\rangle_i + \langle\hat{u}\rangle^2\right] - \left(\sum_i p_i\langle\hat{u}\rangle_i\right)^2 .
\end{aligned}
\tag{5.22}
$$

The Cauchy-Schwarz inequality simplifies the terms involving $\hat{u}$ as

$$
\begin{aligned}
\langle(\Delta\hat{u})^2\rangle_\rho &= \sum_i p_i \left[a^2\langle(\Delta\hat{x}_1)^2\rangle_i + \frac{1}{a^2}\langle(\Delta\hat{x}_2)^2\rangle_i\right] + \left(\sum_i p_i\langle\hat{u}\rangle^2\right) - \left(\sum_i p_i\langle\hat{u}\rangle_i\right)^2 \\
&\geq \sum_i p_i \left[a^2\langle(\Delta\hat{x}_1)^2\rangle_i + \frac{1}{a^2}\langle(\Delta\hat{x}_2)^2\rangle_i\right] + \left(\left|\sum_i p_i\langle\hat{u}\rangle\right|^2\right) - \left(\sum_i p_i\langle\hat{u}\rangle_i\right)^2 \\
&= \sum_i p_i \left[a^2\langle(\Delta\hat{x}_1)^2\rangle_i + \frac{1}{a^2}\langle(\Delta\hat{x}_2)^2\rangle_i\right] .
\end{aligned}
\tag{5.23}
$$

Similarly, $\langle(\Delta\hat{v})^2\rangle_\rho$ is given by

$$
\langle(\Delta\hat{v})^2\rangle_\rho \geq \sum_i p_i \left[a^2\langle(\Delta\hat{p}_1)^2\rangle_i + \frac{1}{a^2}\langle(\Delta\hat{p}_2)^2\rangle_i\right] . \tag{5.24}
$$

Adding Eq. 5.23 and Eq. 5.24 gives

$$
\langle(\Delta\hat{u})^2\rangle_\rho + \langle(\Delta\hat{v})^2\rangle_\rho \geq \sum_i p_i \left[a^2(\langle(\Delta\hat{x}_1)^2\rangle_i + \langle(\Delta\hat{p}_1)^2\rangle_i) + \frac{1}{a^2}(\langle(\Delta\hat{x}_2)^2\rangle_i + \langle(\Delta\hat{p}_2)^2\rangle_i)\right] . \tag{5.25}
$$

The terms multiplied by a^2 depend only on particle one, while the terms multiplied by $1/a^2$ only depend on particle 2. Each can be simplified using the uncertainty relation

$$\langle(\Delta\hat{x}_j)^2\rangle_i + \langle(\Delta\hat{p}_j)^2\rangle_i \geq |[\hat{x}_j, \hat{p}_j]| = 1, \tag{5.26}$$

to get

$$\begin{aligned}\langle(\Delta\hat{u})^2\rangle_\rho + \langle(\Delta\hat{v})^2\rangle_\rho &\geq \sum_i p_i \left[a^2 + \frac{1}{a^2}\right] \\ &= a^2 + \frac{1}{a^2},\end{aligned} \tag{5.27}$$

which completes the proof. The RHS is minimized by $a = 1$, which gives

$$\Delta(x_1 + x_2)_\rho^2 + \Delta(p_1 - p_2)_\rho^2 \geq 2. \tag{5.28}$$

This uncertainty relation can be converted to a product instead of a sum, following the work in ref [230]. The uncertainty relation derived above depends on x_j and p_j following the uncertainty relation $|[\hat{x}_j, \hat{p}_j]|$. Therefore, it also holds for scaled observables defined by $x'_k = sx_k$ and $p'_k = p_k/s$. Dropping the $'$ notation for convenience, this gives a new scaled uncertainty relation

$$s\Delta(x_1 + x_2)_\rho^2 + \frac{1}{s}\Delta(p_1 - p_2)_\rho^2 \geq 2. \tag{5.29}$$

The LHS is minimized for $s = \Delta(p_1 - p_2)_\rho/\Delta(x_1 + x_2)_\rho$, giving

$$\begin{gathered}\left(\frac{\Delta(p_1 - p_2)_\rho}{\Delta(x_1 + x_2)_\rho}\right)\Delta(x_1 + x_2)_\rho^2 + \left(\frac{\Delta(x_1 + x_2)_\rho}{\Delta(p_1 - p_2)_\rho}\right)\Delta(p_1 - p_2)_\rho^2 \geq 2 \\ 2\Delta(x_1 + x_2)_\rho\Delta(p_1 - p_2)_\rho \geq 2.\end{gathered} \tag{5.30}$$

This simplifies to the position-momentum uncertainty product

$$\Delta(x_1 + x_2)_\rho\Delta(p_1 - p_2)_\rho \geq 1. \tag{5.31}$$

Note, every step in the derivation follows exactly the same if $\hat{u}$ is defined with a negative sign instead of $\hat{v}$, as in

$$\hat{u}' = |a|\hat{x}_1 - \frac{1}{a}\hat{x}_2 \tag{5.32}$$

$$\hat{v}' = |a|\hat{p}_1 + \frac{1}{a}\hat{p}_2. \tag{5.33}$$

Therefore, the position-momentum uncertainty product can also be written as

$$\Delta(x_1 - x_2)_\rho \Delta(p_1 + p_2)_\rho \geq 1. \tag{5.34}$$

In either case, measuring a product below 1 indicates the two particles are entangled. The derivation was carried out with unit free x and p observables by setting $\hbar = 1$, but can be rewritten with units using the uncertainty relation $[\hat{x}_j, \hat{p}_{j'}] = i\hbar\delta_{j,j'}$.

Energy-time entangled photons exhibit correlations in their frequency and time-of-arrival, but these quantities can be mapped to momentum and position. Photons travel at the speed of light, c, which provides a mapping of longitudinal position, x, to the time of arrival, $t = x/c$, and a mapping of longitudinal momentum, p, to the light frequency $\hbar\omega = cp$ [230, 231].

Uncertainty relations can be used to detect energy-time entanglement through temporal and spectral measurements. Two separable photons labeled signal (s) and idler (i) must satisfy the inequality [229, 232]

$$\Delta(\omega_s + \omega_i)\Delta(t_s - t_i) \geq 1, \tag{5.35}$$

where ω corresponds to frequency, t corresponds to time of arrival, and $\Delta(\omega_s+\omega_i)(\Delta(t_s-t_i))$ signifies standard deviation in the sum of their frequencies (difference of their detection times) [230]. The quantities in Eq. 5.35 can be determined experimentally by measuring the joint spectral intensity (JSI) and joint temporal intensity (JTI) of a two-photon system. Therefore, violating this inequality is a sufficient condition for witnessing entanglement.

5.3.3 Modeling the Expected Spectral Correlations

Following the model outlined in section 2.4.5, we model the joint spectral amplitude as the pump bandwidth multiplied by the crystal phase-matching function as

$$F(\omega_s, \omega_i) = \alpha(\omega_s + \omega_i)\Phi(\omega_s, \omega_i, \omega_s + \omega_i). \tag{5.36}$$

The pump bandwidth amplitude will be approximated by a Gaussian function, and we'll assume energy conservation, $\omega_p = \omega_s + \omega_i$, giving

$$\alpha(\omega_s + \omega_i) = \exp\left(\frac{-((\omega_s + \omega_i) - \omega_{p0})^2}{4\Delta\omega_p^2}\right), \tag{5.37}$$

where $\Delta\omega_p$ is the pump bandwidth and ω_{p0} is the pump center frequency. The phase-matching function for SPDC is given by Eq. 2.45 as derived in Sec. 2.4.2 and depends on the phase mismatch, $\Delta k = k_p - k_s - k_i$, as

$$\Phi(\omega_s, \omega_i, \omega_s + \omega_i) = e^{\frac{i\Delta kL}{2}} \text{sinc}\left(\frac{\Delta kL}{2}\right), \tag{5.38}$$

where L is crystal length. We model each of the wave vectors, k_p, k_s, and k_i as a second order taylor expansion about each wave's center frequency, yielding

$$\begin{aligned}\Delta k \approx\ & k(\omega_{p0}) - k(\omega_{s0}) - k(\omega_{i0}) \\ & + \frac{dk}{d\omega}(\omega_p - \omega_{p0}) - \frac{dk}{d\omega}(\omega_s - \omega_{s0}) - \frac{dk}{d\omega}(\omega_i - \omega_{i0}) \\ & + \frac{1}{2}\frac{d^2k}{d\omega^2}(\omega_p - \omega_{p0})^2 - \frac{1}{2}\frac{d^2k}{d\omega^2}(\omega_s - \omega_{s0})^2 - \frac{1}{2}\frac{d^2k}{d\omega^2}(\omega_i - \omega_{i0})^2.\end{aligned} \tag{5.39}$$

The wavevector derivatives depend on the index of refraction as shown in Eq. 2.92. In the BiBO crystals used for SPDC in this experiment, crystal birefringence leads to a different index of refraction for the ordinary and extraordinary spatial axes. The pump wave is polarized along the ordinary axis while the signal and idler waves travel along the extraordinary axis.

BiBO is a bi-axial crystal with three different Sellmeier equations for each geometric axis, each of which can be found at [104]. Note, this reference refers to the x, y, and z crystal axes as $n(\alpha)$, $n(\beta)$, and $n(\gamma)$, respectively. The ordinary axis is lined up with the crystal's x-axis, while the effective extraordinary index of refraction, $n_e(\theta)$, depends on angle tuning and the crystal's z and y index of refractions given by

$$\frac{1}{n_e(\theta)^2} = \frac{\sin^2\theta}{n_z^2} + \frac{\cos^2\theta}{n_y^2}. \tag{5.40}$$

The calculation is simplified by approximating the sinc term of the phase-matching function by a Gaussian function with the same bandwidth. This has the effect of removing the lobes of the sinc pulse, but when adding tunable edge spectral filters $S_s(\omega_s)$ and $S_i(\omega_i)$ to each photon we cut off the photon frequencies corresponding to the side lobes anyway. The spectral filters are approximated by Gaussian functions with bandwidths that match the 6 nm FWHM filtering measured in the lab. The spectral intensity correlations are given by

$$\text{JSI} = |\alpha(\omega_s + \omega_i)\Phi(\omega_s, \omega_i, \omega_s + \omega_i)S_s(\omega_s)S_i(\omega_i)|^2. \tag{5.41}$$

The modeled JSI is normalized and presented in Fig. 5.1. Double Fourier transforming the amplitude function before taking the absolute value squared reveals the correlations in time. Squaring the temporal correlations provides the JTI which is also presented in Fig. 5.1.

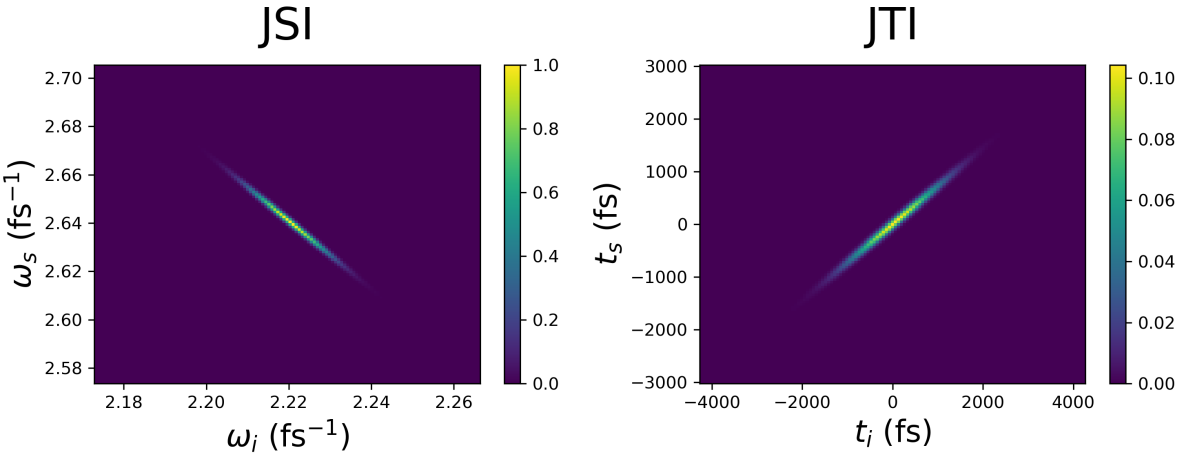

Figure 5.1: Simulation of the intrinsic joint spectral intensity (JSI) and joint temporal intensity (JTI) of photon pairs produced from SPDC in 2 mm of β-BiBO.

Our detection methods have a finite resolution which means measurements of these joint intensity distributions will inevitably widen. The simulation therefore provides insight

into the intrinsic widths of these functions before they are increased by finite measurement device resolution. Many cross sectional slices of the JSI about the $\omega_s = \omega_i$ axis and JTI about the $t_s = -t_i$ axis are averaged to retrieve the intrinsic widths, $\Delta(\omega_s + \omega_i)_{\text{Int}}$ and $\Delta(t_s - t_i)_{\text{Int}}$. The simulation intrinsic widths can also be used to demonstrate energy-time entanglement and provide an approximate lower bound on the largest possible time-bandwidth inequality violation.

$$\begin{aligned}\Delta(\omega_s + \omega_i)_{\text{Int}}\Delta(t_s - t_i)_{\text{Int}} &= (0.000836\text{fs}^{-1})(122\text{fs}) \\ &= 0.102 < 1.\end{aligned} \tag{5.42}$$

5.3.4 Modeling the Expected Temporal Correlations Measured by an OKS

The overall two-photon temporal measurement resolution can be estimated by the quadrature sum of the pump pulse at each shutter, τ_{p}, the walk-off between the pump and signal (idler) photon, $\Delta\tau_{s(i)}$, and the intrinsic width of the JTI about the $t_s = -t_i$ axis, $\Delta(t_s - t_i)_{\text{Int}}$, as

$$\Delta(t_s - t_i) = \sqrt{\Delta\tau_s^2 + \Delta\tau_i^2 + 2\tau_{\text{p}}^2 + \Delta(t_s - t_i)_{\text{Int}}^2}, \tag{5.43}$$

where $\Delta\tau_{s(i)} = L(v_{g_{s(i)}}^{-1} - v_{g_{\text{p}}}^{-1})$, L is the length of the Kerr medium, $v_{g_{s(i)}}$ is the group velocity of the signal (idler) photon, and $v_{g_{\text{p}}}$ is the group velocity of the pump pulse. Note that the factor of two in front of the τ_p^2 term accounts for the pump pulse width at each of the two shutters. Photons from spontaneous parametric downconversion (SPDC) have strong correlations in time of arrival and exhibit an intrinsic width $\Delta(t_s - t_i)_{\text{Int}}$. This width is modelled by first considering the spectral correlations and then using a double Fourier transform to the time domain as shown in Sec. 5.3.3. The walk-off terms in Eq. 5.43, arising from the difference in group velocity between the pump and photons, further increase the width of the JTI. The effect of walk-off on temporal resolution is visualized in 5.2. This figure also illustrates the photon's temporal distribution, consisting of short photon pulses with different possible arrival times.

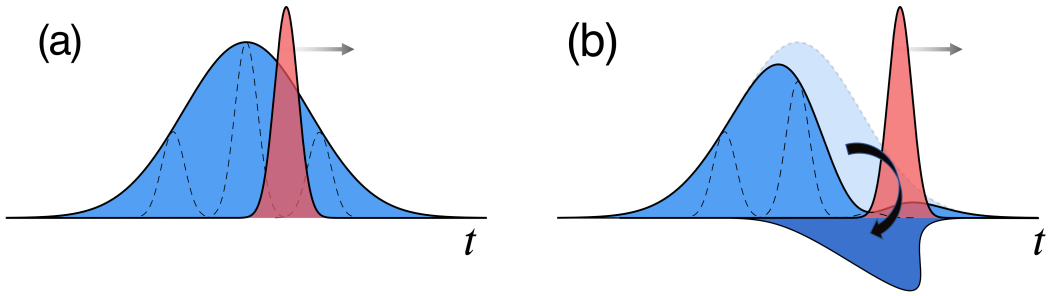

Figure 5.2: Visualization of the main operating principle of an OKS. A 775 nm pump pulse walk-off in a 35 mm fiber in the reference frame of a 714 nm photon (a) Initial temporal representations of the pump pulse relative to the photon. The broader photon distribution, shown in blue, is a combination of shorter photons created at varying times in the crystal, depicted with dotted lines. The pump pulse is shown in red. (b) Final temporal representation after the pump has swept through a section of the photon pulse, rotating its polarization. Delaying the pump pulse relative to the photon allows for gated measurement of different temporal segments of the photon.

5.4 Experimental Setup

An illustration of the experiment is shown in 5.3. Optical pulses with 148 fs full-width at half maximum (FWHM) from a titanium sapphire laser with an 80 MHz repetition rate are guided to three parts of the experiment: an energy-time entangled photon source and two Kerr shutters. The pulsed light is first upconverted by a 2 mm β-bismuth borate (BiBO) crystal to 387.5 nm, spectrally filtered by a 0.1 nm FWHM bandpass filter, and then downconverted in a 5 mm BiBO crystal to produce energy-time entangled photon pairs with wavelengths 714 nm and 847 nm which we refer to as the signal and idler, respectively. Each photon is spectrally narrowed to a bandwidth of 6 nm FWHM, after which we measure a signal count rate of $3.6 \times 10^6 s^{-1}$, an idler count rate of $2.6 \times 10^6 s^{-1}$, and a signal-idler coincidence count rate of $4 \times 10^5 s^{-1}$ using a 3 ns coincidence window. Both photons are fiber-coupled and directed to (a) an OKS, or (b) a scanning monochromator.

The two photons travel through different lengths of fiber to reach their respective OKS. Ideally, our final measurement of the temporal profile of each photon would reveal the true transform-limited widths in time; however, dispersion in each fiber stretches the temporal profile of each photon. The signal photon passes through 50 cm of fiber which applies 10,910 fs^2 of dispersion. The idler photon passes through 21.2 m of fiber which applies

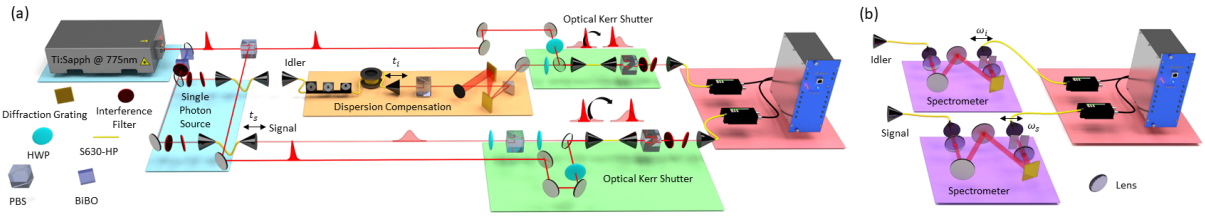

Figure 5.3: Schematic of experimental setup. (a) A titanium-sapphire (Ti:Sapph) laser produces 775 nm pulsed light with a repetition rate of 80 MHz. The light is upconverted in a 2 mm β-BiBO crystal to 387.5 nm to pump the single photon source. Energy-time entangled photon pairs are generated by Type-I SPDC in a 5 mm BiBO crystal. The 847 nm idler photon is sent through a 21.2 m fiber and a grating compressor for dispersion control of the idler photon and non-local dispersion compensation of the 714 nm signal photon. Each photon is Kerr-gated by a strong pulse, picked-off from the output of the Ti:Sapph laser, within a 35 mm piece of SMF (Thorlabs S630-HP). Coincidence detection of the output of each OKS enables measurement of the JTI of the two-photon entangled state. (b) Each photon from the source can alternatively be directed to a scanning monochromator for measurement of the JSI. In this configuration, a grating is used to spread the single photon's optical frequency components spatially, after which a single photon detector can be spatially scanned to detect a given frequency component.

344,064 fs^2 of dispersion. One way to compensate for the dispersion in each path would be to build a grating compressor after each fiber to apply negative dispersion to each photon. Optimal gratings with a near-Littrow configuration provide a total compressor transmission efficiency of around 65% which drops further for shorter wavelength light [107, 108, 109], so to avoid unnecessary loss in the experiment we build a single grating compressor in the idler path. Due to the photon pair time-of-arrival correlations, the gratings can locally cancel the dispersion of the idler and non-locally cancel the dispersion of its partner signal photon [233] by applying second order dispersion of $-(344,064 + 10910)$ fs^2 on the idler photon. Experimentally, we adjust the grating position to minimize the temporal width of the JTI.

Both the signal and idler photon polarizations are prepared along the horizontal axis, while the pump polarization is prepared at 45° relative to the photons to maximize Kerr-rotation along the interaction region [222]. Each photon is combined with a pump pulse on a dichroic mirror and directed into a 35 mm SMF (Thorlabs S630-HP). Both devices have

an equal input pump power of 800mW. Unlike bulk media nonlinear optical crystals, SMF has the advantage that two modes are confined to a small core on the order of 5 μm in diameter which maintains high intensity to increase the nonlinear effect and also facilitates alignment. Pump and photon pulses were coupled into their respective SMFs, each with 40% coupling efficiency. In each OKS, only the part of the photon pulse that overlaps with the pump pulse in the Kerr medium will have its polarization rotated. This portion of the photon pulse will transmit through the Glan-Taylor polarizing beamsplitter (PBS) at the output of each 35 mm SMF. The pump pulse and photon are then separated by interference filters angle-tuned to pass the 6 nm bandwidth of the gated photons. The pump is 61 nm and 72 nm away from the signal and idler photons in wavelength, respectively, which is an equal 32 THz on either side of the pump; however, unwanted noise processes, such as self-phase modulation and Raman scattering, can generate pump noise in the spectral region of the single photons. As a result, tight spectral filtering is required for lowering background counts.

The light that transmits through the PBS and spectral filters, consisting of pump noise and Kerr-gated light from the single photons, is fiber-coupled and detected by avalanche photodiodes. Counts registered by each detector are time-tagged and analyzed with coincidence logic using a 3 ns coincidence window. The relative time of arrival between each photon and its corresponding pump pulse is varied by stepper-motors on the output fiber couplers before each OKS and denoted t_s and t_i in 5.3(a). Sweeping both motors in a raster scan pattern and counting coincidences at each position fully maps out the JTI of the two-photon system. As shown in 5.3(b), spectral measurements are made directly after the source with each photon fiber-coupled and routed directly to scanning monochromators, as in previous experiments [101, 102]. Similarly, raster scanning the motors through frequency measurements on each photon builds up the JSI. We note that it would be possible to work with the energy-time degree of freedom on slower timescales than the requirements of this experimental setup, but only at the cost of requiring higher frequency resolution in the scanning monochromators instead of high temporal resolution.

5.4.1 Determining Relative Path Delay with Spectral Interference

Each of the photons arrives at their respective OKS at the same time as a strong pump pulse. If the photon path and pump path have a length difference of more than 1 mm, then the two pulses have no overlap in time which makes path alignment difficult in the early stages of the experiment. For this reason, a Ti:Sapph was tuned to the frequency of the

photons and sent through both the pump and photon paths. Crucially, both paths have strong laser light of the same frequency. When combined on a beamsplitter, resolving the resultant spectrum gives a classical signal of temporal overlap. Two copies of the same pulse arriving at a beamsplitter will interfere with each other, and the fringes can be viewed on a spectrometer.

A spectrometer receives the signal

$$|E(\omega) + E(\omega)e^{ikL}|^2 \tag{5.44}$$

where $k = \frac{\omega}{c}$ is the wavevector and L is the difference in path length. The e^{ikL} phase difference will be picked up when the two pulses arrive at the beamsplitter at different times. Simplifying this expression gives

$$\begin{aligned} |E(\omega) + E(\omega)e^{i\frac{\omega}{c}L}|^2 &= |E(\omega)|^2 + e^{i\frac{\omega}{c}L}|E(\omega)|^2 + e^{-i\frac{\omega}{c}L}|E(\omega)|^2 + |E(\omega)|^2 \\ &= |E(\omega)|^2(e^{i\frac{\omega}{c}L} + 2 + e^{-i\frac{\omega}{c}L}) \\ &= 2|E(\omega)|^2(1 + \cos\left(\frac{\omega}{c}L\right)). \end{aligned} \tag{5.45}$$

The fringe pattern in the spectrum arises from the $\cos\left(\frac{\omega}{c}L\right)$ term. Fringe peaks occur when this term is maximized which happens at multiples of 2π,

$$\frac{\omega}{c}L = 2\pi n, \quad n \in \mathbb{Z}. \tag{5.46}$$

The difference between neighbouring peaks on a spectrometer is given by

$$\frac{\Delta\omega}{c}L = 2\pi((n+1) - n) = 2\pi. \tag{5.47}$$

Some spectrometers display the signal as a function of wavelength, λ, instead of angular frequency, $\omega = \frac{2\pi c}{\lambda}$. Differentiating with respect to λ relates the change in these variables as

$$\Delta\omega = -\frac{2\pi c}{\lambda^2}\Delta\lambda. \tag{5.48}$$

Substituting Eq. 5.48 into Eq. 5.47 yields

$$L = -\frac{\lambda^2}{\Delta\lambda}, \tag{5.49}$$

Where the sign indicates which of the two paths is longer and can be dropped for absolute path length difference. This equation relates the fringe spacing on the spectrometer to the path length difference and was used to find initial alignment of paths for each OKS. For example, 800 nm light with fringe spacing of $\Delta\lambda = 0.5$ nm indicates the photon path and pump path have a difference of $L = 1.2$ mm.

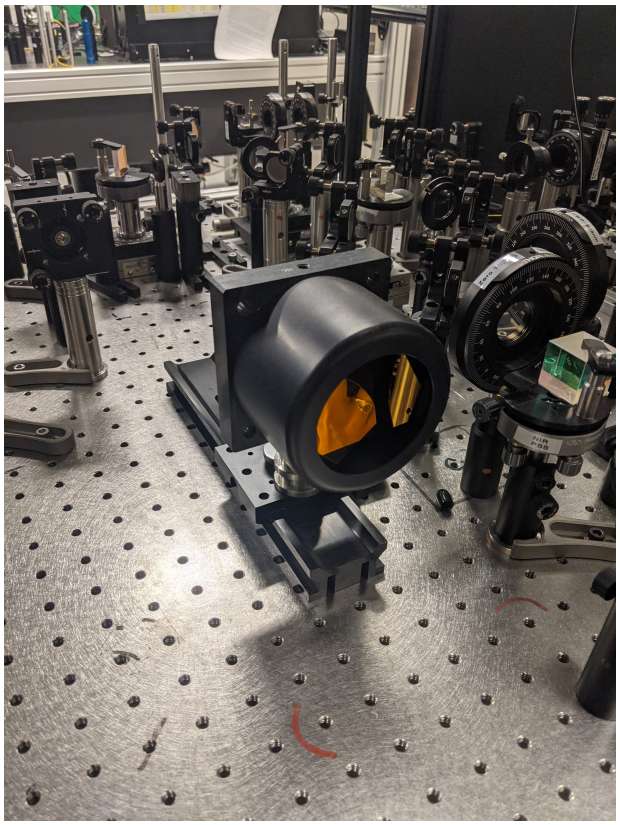

Figure 5.4: Image of the retro reflector mirror used to roughly change optical path length. The mirror reflects light back along the incident path shifted by 1-4 cm depending on the difference between the incident light and the centre of the mirror. Moving the retro reflector by hand along its mounting rail enables a path length range of 50 cm.

When each OKS was built, the original plan was to work with photons at wavelengths 732 nm and 823 nm. At that point, spectral interference was used to align the pump

and photon path, and a large path length varying retro-reflector, pictured in Fig. 5.4, was moved by hand until interference was visible on the spectrometer. Once a temporal overlap was close, the spectrometer changed from a near-Gaussian spectrum to a fringe pattern as showed in Fig. 5.5 for the 732 nm photon.

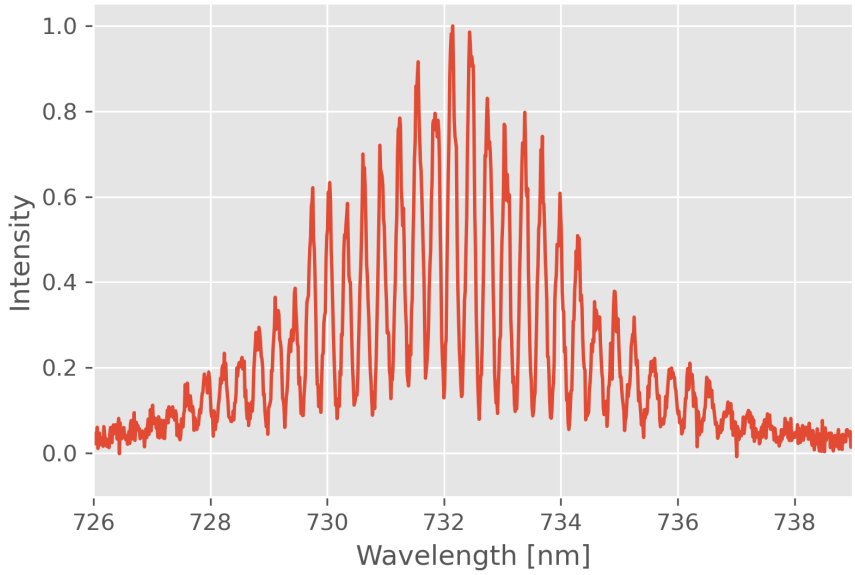

Figure 5.5: Spectral interference of two copies of a 732 nm pulse

When the retro reflector was set to a near-perfect temporal overlap position, the instantaneous spectrum oscillated between a flat signal and a signal of twice the height, indicating perfect destructive and constructive interference, respectfully, in what could best be described as a trampoline animation. At this position, the retro reflector was fixed and fiber-couplers on motorized translation stages were used for a finer resolution path length scan. All joint temporal intensity scans were conducted by these motorized stages.

5.4.2 Grating Compressor Calibration - Spectral Interference

In the previous section, the difference between peaks in the spectral interference of two copies of the same pulse was used to infer relative path delay. Spectral interference can also be used to estimate the relative chirp of the two pulses. The output of the Ti:Sapph

is a transform limited pulse, and the photon path applies normal dispersion in fiber and anomalous dispersion with a grating compressor as discussed in Sec. 2.6.2. When the grating compressor does not perfectly cancel the dispersion due to fiber, chirp can be inferred in the spectral interference as seen in Fig. 5.6(a).

In Fig. 5.6(a), the peaks are further apart in the short wavelength regime and closer together in the long wavelength regime. Chirp can be directly calculated from these decreasing fringe spacings by extracting the phase as a function of wavelength, converting wavelength to frequency, and fitting the phase with a polynomial. The second order coefficient of this polynomial corresponds to the chirp, A, defined in Eq. 2.91.

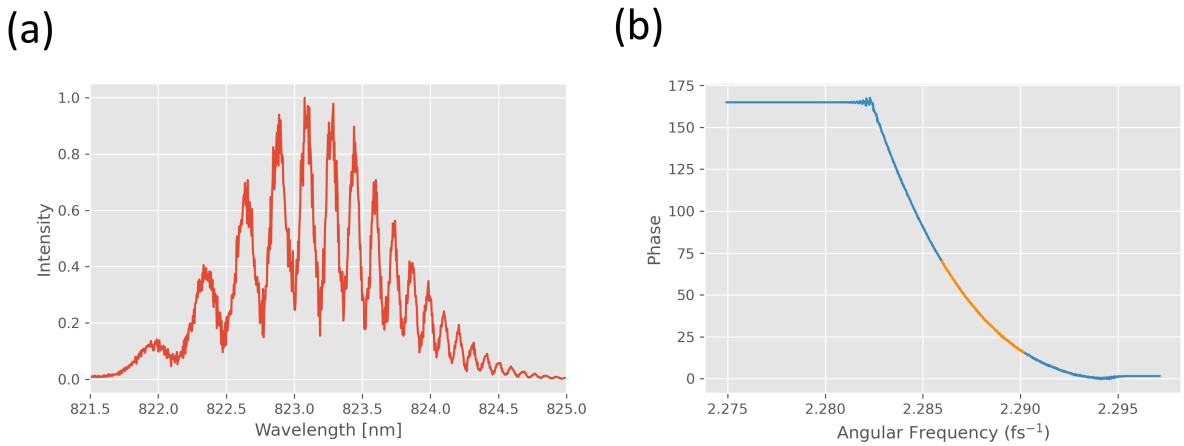

Figure 5.6: Spectral interference of two copies of a 823 nm pulse where quadratic dispersion has been applied to one of the pulses. (a) Spectrometer signal, $I(\lambda)$ (b) Extracted spectral phase.

For example, the phase can be extracted from the spectrum in Fig. 5.6(a) by first obtaining the analytic signal, $I_a(\lambda)$, of the spectrum intensity $I(\lambda)$, given by

$$I_a(t) = \mathcal{F}^{-1}(\mathcal{F}(I(\lambda)2U) = I(\lambda) + iH(I(\lambda)) \tag{5.50}$$

where $\mathcal{F}$ is the Fourier transform, $\mathcal{F}^{-1}$ is the inverse Fourier transform, U is the unit step function, also called the heaviside function, given by

$$U(x) = \begin{cases} 0 & x < 0 \\ 1 & x > 0, \end{cases} \tag{5.51}$$

and H is the Hilbert transform [228] given by

$$H(I)(\lambda) = \frac{2}{\pi} \lim_{\epsilon \to 0} \int_{\epsilon}^{\infty} \frac{I(\lambda - \lambda') - I(\lambda + \lambda')}{2\lambda'} d\lambda'. \tag{5.52}$$

In python, the analytic function can be simply calculated using the scipy.signal.hilbert() function. The spectral phase of interest is the complex argument of the analytic function, which can be obtained with numpy.angle() and unwrapped with numpy.unwrap() to avoid resetting the phase to zero every 2π. The spectral phase as a function of wavelength was converted to angular frequency by the relation $\lambda = 2\pi c/\omega$. This resulted in the spectral phase of the chirped pulse and is shown in Fig 5.6(b).

Visually, the positive curvature in Fig 5.6(b) is apparent indicating a high relative chirp between the pulses in each path. In the ideal case where the dispersion is cancelled completely by the compressor, we expect a relative chirp of zero and a linear spectral phase. This process was completed several times, each time moving the distance, D, between the two gratings in the grating compressor to tune the relative chirp. A calibration curve of the chirp as a function of grating distance is presented in Fig. 5.7. As predicted in Eq. 2.102, A has a linear relationship to D. Eq. 2.102 predicts a compressor sensitivity of $-1962 \pm 50\,\mathrm{fs}^2/\,\mathrm{mm}$, and the slope of the calibration curve in Fig. 5.7 gives a similar experimental sensitivity of $-2040 \pm 50\,\mathrm{fs}^2/\,\mathrm{mm}$.

The calibration curve was used for the initial coarse alignment of the grating compressor. Ultimately, the antidiagonal width of the JTI needs to be as small as possible to minimize $\Delta(t_s - t_i)$ and verify energy-time entanglement through the time-bandwidth inequality. A finer calibration of the grating compressors was conducted by minimizing this width as shown in the following section.

5.4.3 Grating Compressor Calibration - Joint Temporal Intensity

Spectral interference enables characterization of the relative path delay and grating compressor as seen in the previous sections. It required the Ti:Sapph to be tuned to the wavelength of the photons and a beamsplitter to combine the two paths. This simulates the experiment to a good approximation, but falls short in two ways. First, the frequency and bandwidth of the photons produced by downconversion may be slightly different than the classical pulse used for calibration. Second, the beamsplitter that combines the two pulses is taken out and replaced with a dichroic mirror in the experiment because the pump

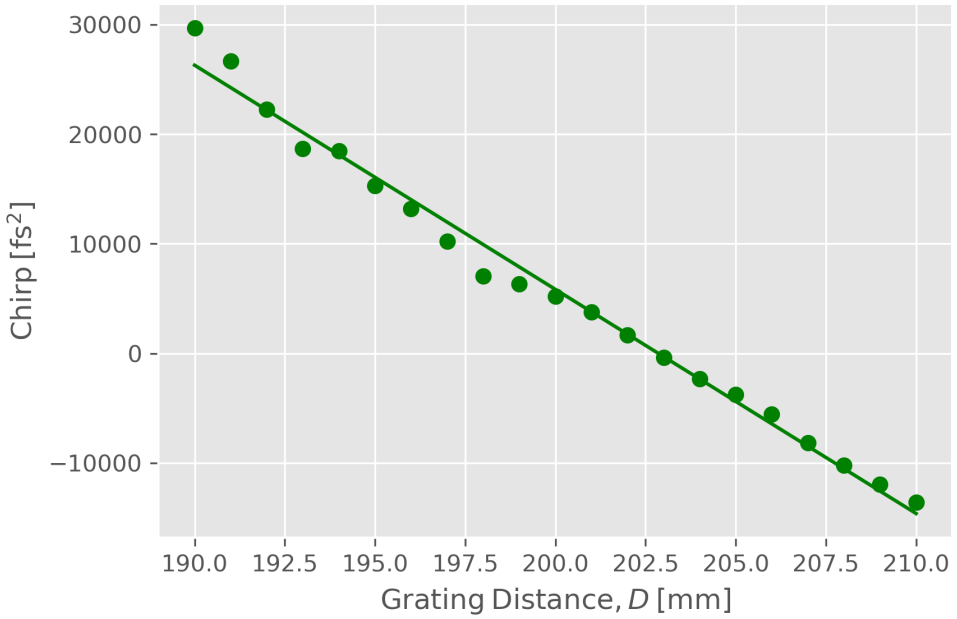

Figure 5.7: Calibration curve of grating compressor. Quadratic dispersion at different grating separation distances with slope $-2040 \pm 50\,\mathrm{fs}^2/\,\mathrm{mm}$

pulse and photons entering the OKS have different centre wavelengths. When the dichroic mirror is installed, the path lengths may be slightly different.

The joint temporal intensity is built up in a raster scan pattern by scanning the fiber-couplers labeled t_s and t_i in Fig. 5.3. When there is a nonzero chirp present in one of the photons, the JTI will present a longer antidiagonal width, $\Delta(t_s - t_i)$. The grating compressor can be tuned to minimize this width. JTI measurements take around 36 hours each, which is much longer than the spectral interference method, so fewer data points were taken for calibration.

Table 5.1 shows the JTI width for four different grating positions. An optimal position is found at position $D = 180\,\mathrm{mm}$. Note, this is different than the optimal $D = 203\,\mathrm{mm}$ presented in the spectral interference calibration. There are two main reasons for the difference. First, between the two calibrations, the source was realigned to produce photon-pairs at different wavelengths. The first setup was for 732 nm and 823 nm signal and idler, respectively, and the second setup moved to 714 nm and 847 nm. This was done to minimize Raman scattering to the red of the 775 nm pump creeping into the frequency band of the idler photon. Second, the first calibration only accounted for the dispersion of the idler

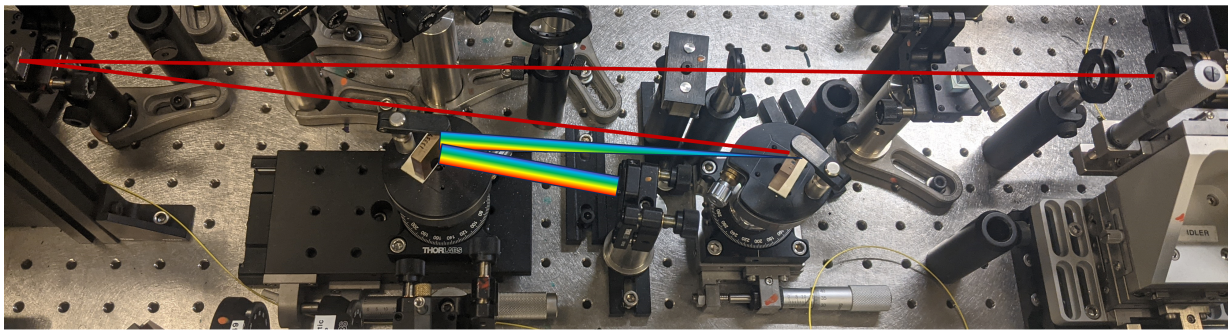

Figure 5.8: Image of the grating compressor used to cancel the dispersion on the idler photon locally and cancel the dispersion on the signal photon non-locally. Red lines have been added on top of the image to indicate light entering the compressor, and a rainbow spread of colors has been added to illustrate the spread and collimation of the different frequency components by the gratings. The second grating's position can be tuned by the translation stage its mounted on.

Grating Distance, D [mm]	$\Delta(t_s - t_i)$ [fs]
177	413 ± 30
180	340 ± 30
182	417 ± 30
187	472 ± 30

Table 5.1: Grating compressor separation, D, and corresponding JTI widths, $\Delta(t_s - t_i)$. Each JTI took around 36 hours to measure. $D = 180\,\text{mm}$ minimizes relative quadratic spectral phase between the two photons and therefore minimizes $\Delta(t_s - t_i)$.

photon path from the fiber and grating compressor. The second calibration was also done to nonlocally cancel the dispersion in the short fiber in the signal photon path [233]. Correlations between signal and idler are required for nonlocal dispersion cancellation, so this could not be factored in to the classical signal from the spectral interference calibration.

5.4.4 Stimulated Raman Scattering

The optical Kerr effect used for gated measurement relies on the $\chi^{(3)}$ susceptibility in SMF. With an average incident laser power of 800 mW in this experiment, other undesirable $\chi^{(3)}$ processes such as self-phase modulation and stimulated Raman scattering occur in the

SMF. The photons created in these processes will be spectrally filtered after the SMF as long as they are outside of the signal and idler photon bandwidth. Self-phase modulation does not produce unwanted photons in the 714 ± 3 nm or 847 ± 3 nm bands of the signal and idler at this pump power with a laser center frequency of 775 nm. However, stimulated Raman scattering does produce noise photons in the idler band. This process will be discussed in more detail here.

Stimulated Raman scattering is a $\chi^{(3)}$ nonlinear optical process where light is absorbed by a material and emitted at a lower energy, called the Stokes frequency. For conservation of energy to hold, the excess energy is absorbed by the atoms in the material leaving the atoms in an excited stated with energy $\hbar\omega_v$, usually corresponding to a vibrational excited state. The intensity of light produced in stimulated Raman scattering is proportional to the pump power [4, 234]. This process can be as efficient as 10% of incident laser power converting to the Stokes frequency. While it is undesirable in our case, Raman scattering has been exploited to learn about the atomic composition and structure of molecules in a process referred to as Raman spectroscopy [235].

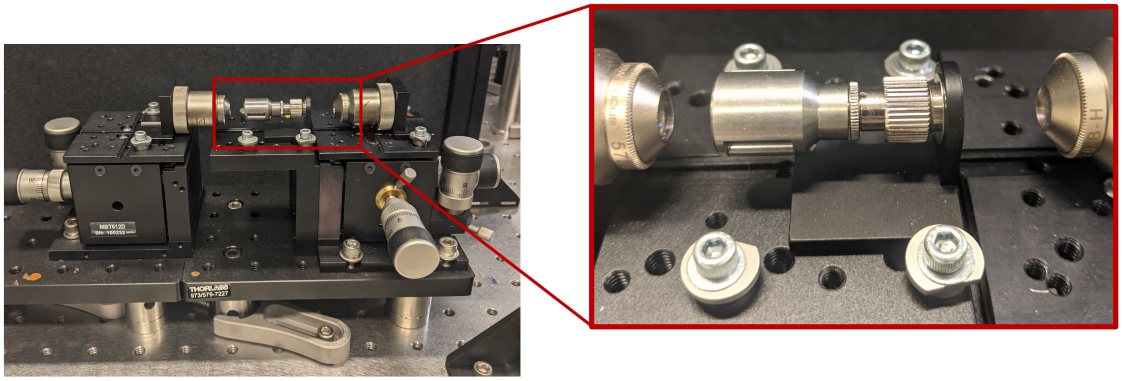

Figure 5.9: Image of 3.5 mm SMF holder mounted between two lenses in an optical Kerr shutter.

Raman scattering was minimized in this experiment by implementing a short Kerr medium and choosing a single photon source wavelength regime sufficiently far from the pump frequency. In Fig. 5.9, a 3.5 mm SMF is mounted in a holder of the same length with lenses coupling light in and out of the fiber. This was the shortest fiber we could

cleave and mount effectively in a stable setup. Short fibers have the advantage of higher OKS temporal resolution and lower noise from Raman scattering.

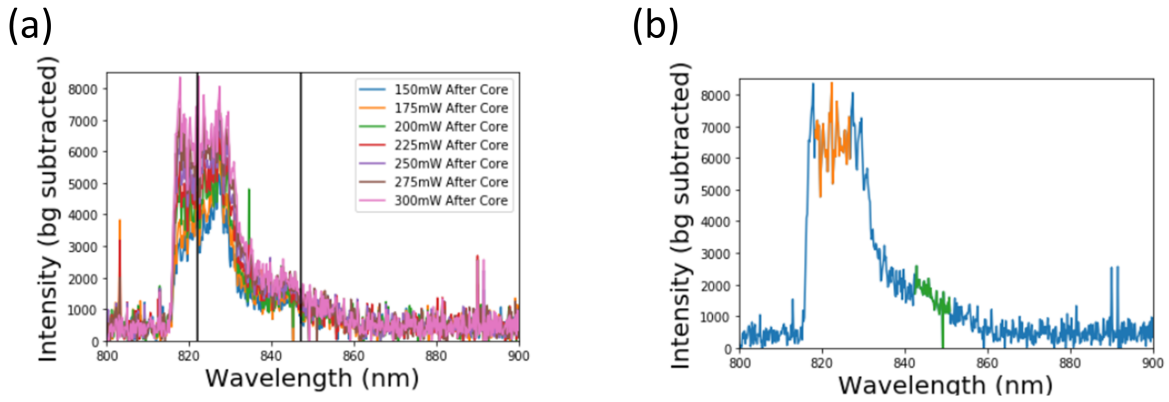

Figure 5.10: Raman scattering of a 775 nm strong pump pulse in the frequency band of the idler photon. (a) An 815 nm low-pass spectral filter blocks the 775 nm pump pulse which is varied between 150 mW and 300mW average power as measured at the output of the Kerr medium. Black lines indicate the center frequency of the original idler frequency, 823 nm, and the modified idler frequency, 847 nm. (b) An orange overlay highlights the frequency band of the original idler photon, and a green overlay highlights the band of the modified idler photon. Noise reduction of about 70% is achieved by moving to the 847 nm band.

In the first version of the experiment, we chose a source wavelength regime tighter to the 775 nm pump pulse with signal and idler wavelengths 732 nm and 823 nm, respectively. Stimulated Raman scattering was the main reason for eventually moving to wavelengths further away from the pump. A Raman scattering measurement was made before changing the source, with results plotted in Fig. 5.10. For this measurement, an 815 nm low pass spectral filter was placed after the idler OKS. An Ocean Optics USB4000-VIS-NIR spectrometer was placed after the filter to examine which frequencies were generated in the SMF by stimulated Raman scattering.

Fig. 5.10(a) shows the Raman noise spectrum at different pump powers as measured after the SMF core. The linear scaling of noise with pump power is characteristic of Raman scattering, and wavelengths further away from the 775 nm pump pulse exhibit less noise. Black lines indicate the original idler wavelength at 823 nm, and the adjusted idler wavelength at 847 nm. Fig. 5.10(b) shows the original and modified idler photon bandwidth in orange and green, respectively. A reduction of Raman scattering noise of about 70% is

achieved by moving out of the 823 nm band. Avalanche photodiode (APD) single photon detectors used in this experiment have lower quantum efficiencies at wavelengths longer than 847 nm, which limited how far we could move the idler frequency away from the Raman noise.

5.5 Experimental Results

We define the maximum achieved gating efficiency to be the fraction of photons gated out of all possible photons, acknowledging that the pump samples a short window in time and photons have varying arrival times related to the width of the downconversion crystal and the probabilistic pair-generation. The maximum achieved gating efficiency is estimated to be approximately 16% at the peak of the JTI. The total efficiency of the entire temporal coincidence measurement which combines coupling losses from the grating compressor, both OKS coupling losses, both final SMF coupling losses, and gating efficiency is approximately 0.01%.

We present both the raw data and noise from the OKS temporal measurement in 5.11. Each pixel of the images in (a) and (b) is a coincidence measurement between the signal OKS and idler OKS with relative delays t_s and t_i. 5.11(a) shows the raw data which includes the two-photon correlations as well as the unwanted background consisting of accidental coincidences and constant pump leakage, while 5.11(b) is an estimate of background. The coincidence rates between the gated signal and idler photons are a function of electronic delay between the two detectors. Accidental coincidence peaks occur every 12.5 ns from the relative zero delay, corresponding to the repetition rate of the laser. The peak directly following the relative zero delay is used to estimate accidental coincidences plus the constant pump leakage. The background profile in 5.11(b) reveals a horizontal "stripe" pattern in the accidental coincidences. The relative noise difference of the signal and idler OKS is apparent in 5.11(c). The idler noise rate is 480 kHz counts compared to the 200 kHz counts for the signal channel. This is because Raman scattering is higher on the low-frequency (Stokes) side of the pump pulse.

Both temporal and spectral correlations are presented in 5.12. The JTI in 5.12(a) is obtained by pixel-wise subtraction of the raw data and background estimation from 5.11(a) and (b). Note, there are two timescales of importance: A cross-sectional slice of the JTI corresponds to the temporal width of an individual photon with 320 ± 30 fs for the signal, and 290 ± 30 fs for the idler, while the marginals of the JTI correspond to the uncertainty in arrival time which we measure to be 470 ± 30 fs for signal and 520 ± 30 fs for idler. This can be visualized in 5.2 where the blue photon pulse has a much wider envelope than any

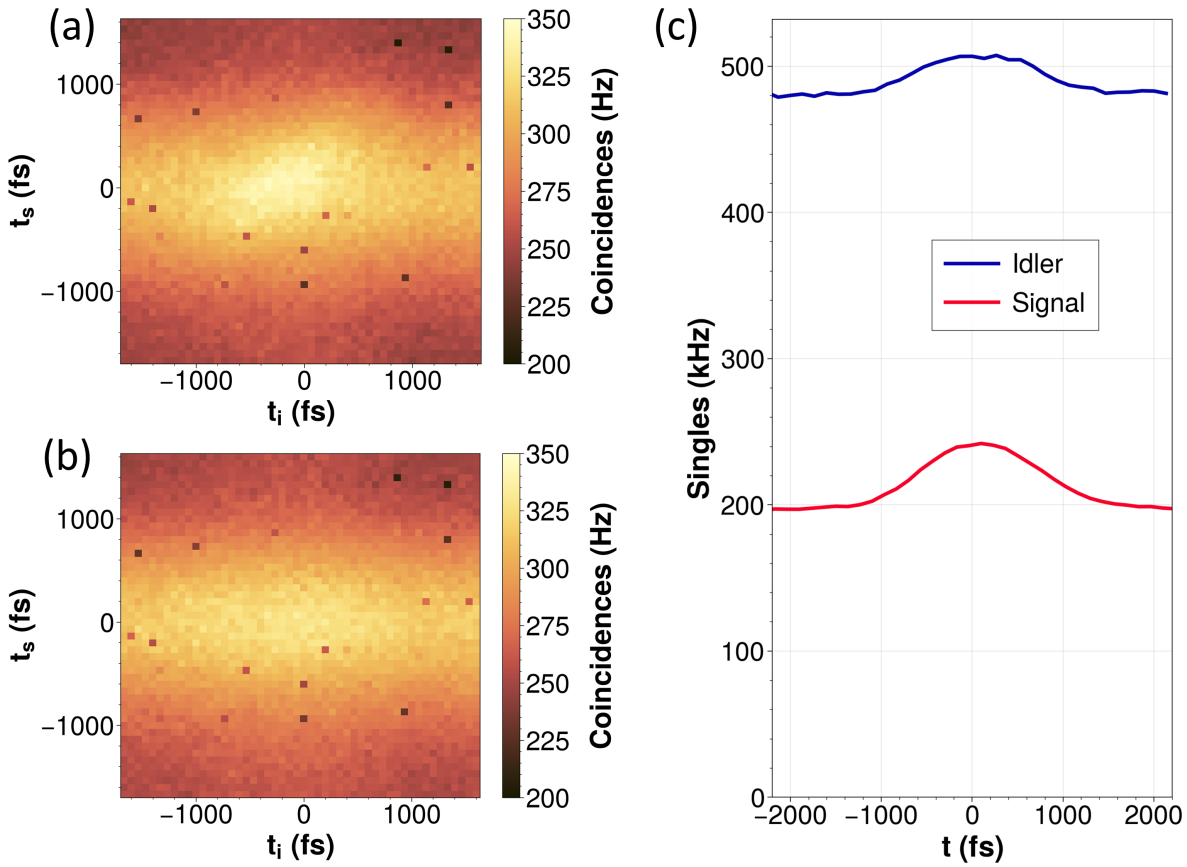

Figure 5.11: Background subtraction in post processing. (a) Measured coincidences between two Kerr shutters at different relative gate delays t_s and t_i. (b) Estimation of accidental coincidences and constant pump background, measured by adding 12.5ns of electronic delay between the two photon counting signals (corresponding to the repetition rate of the laser). The small number of artifacts that make a speckle pattern across the image are the result of a momentary fault in time tagging electronics. (c) Single counts at detectors after each OKS.

given photon, shown as dotted lines, in the temporal distribution. Spectral measurements taken with single photon scanning monochromators exhibit low noise and therefore do not require the background subtraction procedure discussed for the temporal measurements.

Measurement uncertainty takes into account the Poissonian statistics of the photon counting as well as the effect of background subtraction. The JTI is measured by subtracting the estimated background 5.11(b) from the raw data 5.11(a). Because the data and

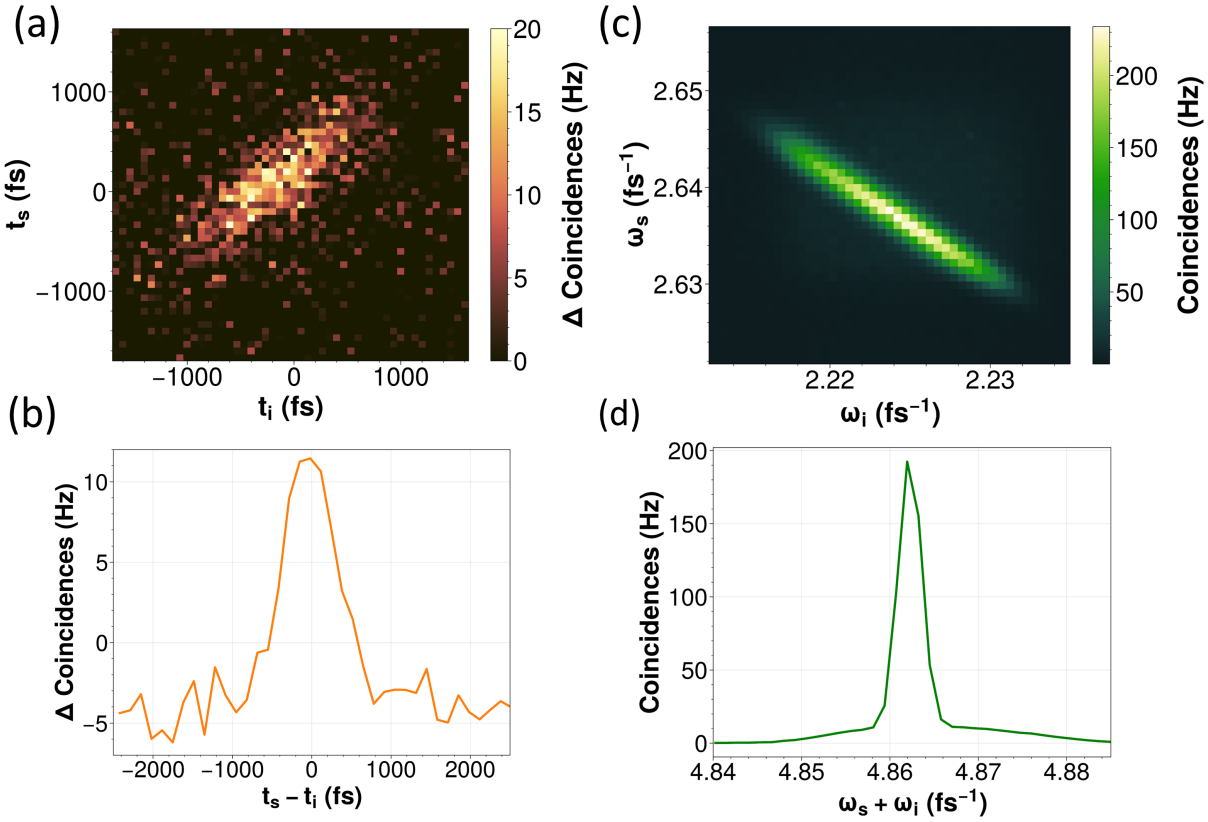

Figure 5.12: Experimental characterization of the photon-pair temporal and spectral correlations. (a) Joint temporal intensity, (b) joint spectral intensity, (c) Cross-sectional slices of (a) about the $t_s = -t_i$ axis, and (d) Cross-sectional slices of (b) about the $\omega_s = \omega_i$ axis. For both (b) and (d), multiple slices were taken through the distributions and averaged together. The time-of-arrival of the two photons are positively correlated, while their frequencies are anticorrelated. Negative coincidence values in (c) are possible only because of the JTI background subtraction demonstrated in 5.11. Gaussian fitting to plots (c) and (d) yields $\Delta(t_s - t_i) = (340 \pm 30)$ fs and $\Delta(\omega_s + \omega_i) = (0.00141 \pm 0.00002)\,\mathrm{fs}^{-1}$. Together, these quantities demonstrate entanglement with $\Delta(t_s - t_i)\Delta(\omega_s + \omega_i) = (0.48 \pm 0.04)$ which is less than one by 13 standard deviations.

background are very similar in magnitude, the JTI measurement is highly sensitive to the estimated background. To quantify this effect, we multiply the estimated background by a variable scaling factor to determine the dependence of $\Delta(t_s - t_i)$ on the background level.

This variation is included in the reported measurement uncertainty.

The estimate in Eq.5.43 gives $\Delta(t_s - t_i) = (430 \pm 30)\,\text{fs}$. Experimental data reveals a somewhat smaller width of $\Delta(t_s - t_i) = (340 \pm 30)\,\text{fs}$. Many cross-sectional slices of the JTI about the $t_s = -t_i$ axis and JSI about the $\omega_s = \omega_i$ axis are averaged and shown in 5.12(c),(d). Gaussian fits to these curves show an entanglement witness value of $\Delta(t_s - t_i)\Delta(\omega_s + \omega_i) = (340 \pm 30)\,\text{fs}\ (0.00141 \pm 0.00002)\,\text{fs}^{-1} = 0.48 \pm 0.04$. This demonstrates a violation of Eq. 5.35 by 13 standard deviations indicating entanglement in the energy-time degree of freedom.

Our experimental parameters were based on a compromise of the various factors that influence efficiency, noise, and temporal resolution in an OKS. The OKS efficiency increases with pump intensity and fiber length; however, increasing these parameters also increases the generation rate of noise photons by self-phase modulation and spontaneous Raman scattering. In general, a large frequency difference between the pump and photon pulses will limit the generation of these noise photons at the signal and idler frequencies. In our normally dispersive SMF, an increased frequency difference increases the pump-photon group velocity walk-off and thus reduces the temporal resolution. We operated our experiment with a frequency difference $\Delta\omega = 32\,\text{THz}$, fiber length $L = 35\,\text{mm}$, and pump power $P = 800\,\text{mW}$, yielding sufficient efficiency, signal-to-noise ratio, and temporal resolution, to measure energy-time entanglement. Future OKS pulse metrology experiments might operate with lower Raman scattering noise levels by using a pump pulse frequency lower than both the signal and idler pulses. The use of dispersion-engineered photonic crystal fibers for pump-photon group velocity matching [227] would enable the use of longer fibers for increased efficiency, while retaining optimal temporal resolution.

As an example of an experiment which could benefit from ultrafast measurement of photons higher in frequency than the pump, in Ref. [236], spectral correlations of energy-time entangled photons are engineered to be positively correlated instead of negatively correlated as is typical of energy conservation in SPDC. This was done with a time lens using sum frequency generation and resulted in photons of higher frequency than the pump used to create them. The temporal correlations of the upconverted signal were modelled, but the experimenters did not temporally resolve the signal to verify energy-time entanglement experimentally. An OKS would be a good fit this experiment, where low noise could be achieved due to the photons being higher frequency than the pump and therefore outside of the stimulated Raman scattering noise regime.

In reference [102], the JSI and JTI of energy-time entangled photons, as well as the correlations between the frequency of one photon and the time-of-arrival of the other, were used to reconstruct the entire two-photon amplitude and phase, $F(\omega_s, \omega_i)$. The temporal

measurement technique was limited by tight phase-matching constraints of sum frequency generation in a 1 mm BiBO crystal, and by the optical gating efficiency of this nonlinear process. The methods outlined in this chapter, along with the potential high-efficiency increase provided by dispersion-engineered photonic crystal fibers, could be implemented in a similar phase reconstruction procedure to realize high efficiency energy-time entanglement phase estimation, and thus, quantum state reconstruction.

5.6 Conclusion

In this work, we used optical Kerr shutters to directly measure the JTI of two energy-time entangled photons. Correlations were measured with a temporal resolution of 320 ± 30 fs and 290 ± 30 fs for signal and idler photons, respectively, which provided a sufficient gating resolution to violate a time-bandwidth inequality and therefore witness energy-time entanglement. With the capability of distinguishing events less than one picosecond apart, and therefore outside the temporal resolution of current detector speeds, the optical Kerr shutter is a valuable addition to the available methods in ultrafast quantum optics control and metrology.

Chapter 6

Outlook

Throughout this thesis, generation and measurement of entanglement across multiple degrees of freedom was demonstrated. First, in the experiments in chapter 3 and 4, unique structured waves of light where quantum information was entangled across the polarization and spatial mode of photons were produced and measured with a gated emICCD camera. Next, the experiment presented in chapter 5 measured frequency and temporal correlations of energy-time entangled states using a fast optical-gating method which took advantage of the optical Kerr effect.

Generally, both the spatial mode experiments and the energy-time experiment were motivated by high-dimensional Hilbert spaces. With perfect preparation, control, and measurement methods, a photonic degree of freedom that has access to a high dimensional Hilbert space would be a very important advancement for optical quantum technologies. Of these possible technologies, quantum networks stand the most to gain due to the clear advantage that photons have over other quantum information systems in their speed-of-light distribution and their high robustness against decoherence. Any successful distributed quantum computation task or quantum communication protocol we come up with in the future will likely involve high dimensional photons. There are ways both the spatial modes and energy-time modes generated in this thesis could be improved and potentially used in future quantum technologies.

For structured waves, free space channels will likely be the focus of research moving forward as the quantum states are not maintained in fiber. However, there have been experiments looking at underwater channels as well [237, 238]. The LOV prism-pair setup used in this thesis to generate structured waves requires improvements in order to be considered for future structured wave applications. The remote state preparation experiment

showed that although entanglement verification is possible, the strength of entanglement across the pixels was lower than theoretically expected by a significant margin. Further study is required to fully understand the drop in entanglement, but we suspect the two major contributions to be beam deflection in the prisms and detection error in the camera. For example, if a photon is accidentally detected by an emICCD pixel's neighbour rather than the intended pixel, a common camera issue referred to as cross talk, then the pixel-wise quantum state tomography procedure for detecting entanglement will measure density matrices not indicative of the true quantum state. There are techniques being developed to reduce cross talk which could help further demonstrate the use of the LOV prism pairs for quantum communication protocols [239]. If a higher entanglement measurement was demonstrated, the next step to building out LOV prism pairs for high dimensional applications would be series of many prisms. A device that could move series of prisms and beamsplitters in and out of an optical beam would be capable of encoding spatial modes with different radial and azimuthal quantum numbers [5].

Photonic states encoded in frequency and time, on the other hand, have a high likelihood of being implemented in fiber-based architectures. Whether future quantum networks use time-bin, frequency-bin, or temporal mode states, fast temporal resolution will be required to maximize high-dimensional state multiplexing. The optical Kerr measurement technique explored in this thesis demonstrated a new time-regime for entangled photon pair measurements. There are further signal-to-noise ratio improvements possible with the operation of two time-locked lasers each operating at a lower frequency than the photon it is gating. Avoiding Raman scattering with this relative frequency regime is a promising path forward for ultrafast optical gating of single photons. A clear next step involves building on past phase-reconstruction techniques which relied on joint spectral and temporal measurements as taken in this thesis, as well as time-frequency and frequency-time joint measurements [102]. This would further demonstrate the utility of the optical Kerr shutter for quantum optical technologies.

There has been a significant push in laboratory experiments showing high-dimensional photons are a promising candidate for quantum information science [118]. As investment in quantum technologies grows, experiments are being built on a larger scale and we are seeing a move from academia to industry. This trend indicates the future of quantum information will continue to be an exciting story to follow. The experiments in this thesis have aimed to play an impactful role in the utility of the photon in this journey.

References

[1] Ludovico Carbone, Paul Fulda, Clive Bond, Frank Brueckner, Daniel Brown, Mengyao Wang, Deepali Lodhia, Rebecca Palmer, and Andreas Freise. The generation of higher-order laguerre-gauss optical beams for high-precision interferometry. *Journal of visualized experiments : JoVE*, 08 2013. xiii, 14, 18

[2] Manuel Erhard, Robert Fickler, Mario Krenn, and Anton Zeilinger. Twisted photons: new quantum perspectives in high dimensions. *Light: Science & Applications*, 7(3):17146, March 2018. xiii, 15, 19, 71, 88

[3] Robert Fickler, Mario Krenn, Radek Lapkiewicz, Sven Ramelow, and Anton Zeilinger. Real-Time Imaging of Quantum Entanglement. *Scientific Reports*, 3(1):1914, May 2013. xiii, 19

[4] Robert W. Boyd. *Nonlinear Optics, Third Edition*. Academic Press, Inc., USA, 3rd edition, 2008. xiv, 35, 37, 44, 51, 56, 57, 121

[5] D. Sarenac, D. G. Cory, J. Nsofini, I. Hincks, P. Miguel, M. Arif, Charles W. Clark, M. G. Huber, and D. A. Pushin. Generation of a lattice of spin-orbit beams via coherent averaging. *Phys. Rev. Lett.*, 121:183602, Oct 2018. xiv, 71, 76, 77, 78, 82, 89, 129

[6] Rodney Loudon. *The Quantum Theory of Light*. Clarendon Press, Oxford, 1973. 1, 35

[7] Christopher Gerry and Peter Knight. *Introductory Quantum Optics*. Cambridge University Press, Cambridge, 2004. 1, 4

[8] Ulf Leonhardt. *Essential Quantum Optics: From Quantum Measurements to Black Holes*. Cambridge University Press, Cambridge, 2010. 1

[9] K. J. Blow, Rodney Loudon, Simon J. D. Phoenix, and T. J. Shepherd. Continuum fields in quantum optics. *Phys. Rev. A*, 42:4102–4114, Oct 1990. 5

[10] B. Brecht, Dileep V. Reddy, C. Silberhorn, and M. G. Raymer. Photon temporal modes: A complete framework for quantum information science. *Phys. Rev. X*, 5:041017, Oct 2015. 7, 22

[11] B. Cabrera, R. M. Clarke, P. Colling, A. J. Miller, S. Nam, and R. W. Romani. Detection of single infrared, optical, and ultraviolet photons using superconducting transition edge sensors. *Applied Physics Letters*, 73(6):735–737, 08 1998. 7

[12] Damask N. Jay. *Polarization Optics in Telecommunications*, volume 101. Springer New York, NY, 2004. 10

[13] Michael J. Grabowecky, Christopher A. J. Pollack, Andrew R. Cameron, Robert W. Spekkens, and Kevin J. Resch. Experimentally bounding deviations from quantum theory for a photonic three-level system using theory-agnostic tomography. *Phys. Rev. A*, 105:032204, Mar 2022. 11

[14] Jeremy L. O'Brien, Akira Furusawa, and Jelena Vučković. Photonic quantum technologies. *Nature Photonics*, 3(12):687–695, December 2009. 11

[15] Halina Rubinsztein-Dunlop, Andrew Forbes, M V Berry, M R Dennis, David L Andrews, Masud Mansuripur, Cornelia Denz, Christina Alpmann, Peter Banzer, Thomas Bauer, Ebrahim Karimi, Lorenzo Marrucci, Miles Padgett, Monika Ritsch-Marte, Natalia M Litchinitser, Nicholas P Bigelow, C Rosales-Guzmán, A Belmonte, J P Torres, Tyler W Neely, Mark Baker, Reuven Gordon, Alexander B Stilgoe, Jacquiline Romero, Andrew G White, Robert Fickler, Alan E Willner, Guodong Xie, Benjamin McMorran, and Andrew M Weiner. Roadmap on structured light. *Journal of Optics*, 19(1):013001, nov 2016. 15

[16] John Nye and Francis J. Wright. Natural Focusing and Fine Structure of Light: Caustics and Wave Dislocations. *American Journal of Physics*, 68(8):776–776, 08 2000. 15

[17] David S. Bradshaw, Jamie M. Leeder, Matt M. Coles, and David L. Andrews. Signatures of material and optical chirality: Origins and measures. *Chemical Physics Letters*, 626:106–110, 2015. 15

[18] Nicolas J. Cerf, Mohamed Bourennane, Anders Karlsson, and Nicolas Gisin. Security of quantum key distribution using d-level systems. *Phys. Rev. Lett.*, 88:127902, Mar 2002. 15

[19] Toshihiko Sasaki, Yoshihisa Yamamoto, and Masato Koashi. Practical quantum key distribution protocol without monitoring signal disturbance. *Nature*, 509(7501):475–478, May 2014. 15

[20] Earl T. Campbell, Hussain Anwar, and Dan E. Browne. Magic-state distillation in all prime dimensions using quantum reed-muller codes. *Phys. Rev. X*, 2:041021, Dec 2012. 15

[21] Alessio D'Errico, Raffaele D'Amelio, Bruno Piccirillo, Filippo Cardano, and Lorenzo Marrucci. Measuring the complex orbital angular momentum spectrum and spatial mode decomposition of structured light beams. *Optica*, 4(11):1350–1357, Nov 2017. 16, 17

[22] Jörg Enderlein and Francesco Pampaloni. Unified operator approach for deriving hermite–gaussian and laguerre–gaussian laser modes. *J. Opt. Soc. Am. A*, 21(8):1553–1558, Aug 2004. 16

[23] Victor V. Kotlyar, Anton A. Almazov, Svetlana N. Khonina, Victor A. Soifer, Henna Elfstrom, and Jari Turunen. Generation of phase singularity through diffracting a plane or gaussian beam by a spiral phase plate. *J. Opt. Soc. Am. A*, 22(5):849–861, May 2005. 18

[24] L. Marrucci, C. Manzo, and D. Paparo. Optical spin-to-orbital angular momentum conversion in inhomogeneous anisotropic media. *Phys. Rev. Lett.*, 96:163905, Apr 2006. 18

[25] Richard A. Beth. Mechanical detection and measurement of the angular momentum of light. *Phys. Rev.*, 50:115–125, Jul 1936. 19

[26] M. F. Andersen, C. Ryu, Pierre Cladé, Vasant Natarajan, A. Vaziri, K. Helmerson, and W. D. Phillips. Quantized rotation of atoms from photons with orbital angular momentum. *Phys. Rev. Lett.*, 97:170406, Oct 2006. 19

[27] H. He, M. E. J. Friese, N. R. Heckenberg, and H. Rubinsztein-Dunlop. Direct observation of transfer of angular momentum to absorptive particles from a laser beam with a phase singularity. *Phys. Rev. Lett.*, 75:826–829, Jul 1995. 19

[28] Miles Padgett and Richard Bowman. Tweezers with a twist. *Nature Photonics*, 5(6):343–348, June 2011. 19

[29] V. Bazhenov, Mikhail Vasnetsov, and Marat Soskin. Laser beams with screw dislocations in their wavefronts. *JETP. Lett*, 52:429–431, 01 1990. 19

[30] N. R. Heckenberg, R. McDuff, C. P. Smith, H. Rubinsztein-Dunlop, and M. J. Wegener. Laser beams with phase singularities. *Optical and Quantum Electronics*, 24(9):S951–S962, September 1992. 19

[31] Graham Gibson, Johannes Courtial, Miles J. Padgett, Mikhail Vasnetsov, Valeriy Pas'ko, Stephen M. Barnett, and Sonja Franke-Arnold. Free-space information transfer using light beams carrying orbital angular momentum. *Opt. Express*, 12(22):5448–5456, Nov 2004. 19

[32] Xudong Bai, Fanwei Kong, Yuntao Sun, Guanfu Wang, Jingyi Qian, Xianbin Li, Anjie Cao, Chong He, Xianling Liang, Ronghong Jin, and Weiren Zhu. High-efficiency transmissive programmable metasurface for multimode oam generation. *Advanced Optical Materials*, 8(17):2000570, 2020. 20

[33] Fan Qin, Lulan Wan, Lihong Li, Hailin Zhang, Gao Wei, and Steven Gao. A transmission metasurface for generating oam beams. *IEEE Antennas and Wireless Propagation Letters*, 17(10):1793–1796, 2018. 20

[34] Muhammad Rizwan Akram, Xudong Bai, Ronghong Jin, Guy A. E. Vandenbosch, Malin Premaratne, and Weiren Zhu. Photon spin hall effect-based ultra-thin transmissive metasurface for efficient generation of oam waves. *IEEE Transactions on Antennas and Propagation*, 67(7):4650–4658, 2019. 20

[35] Alaaeddine Rjeb, Habib Fathallah, and Mohsen Machhout. *OAM Modes in Optical Fibers for Next Generation Space Division Multiplexing (SDM) Systems*. IntechOpen, Rijeka, 2021. 20

[36] Manish K. Gupta and Jonathan P. Dowling. Dephasing of single-photon orbital angular momentum qudit states in fiber: Limits to correction via dynamical decoupling. *Phys. Rev. Appl.*, 5:064013, Jun 2016. 20

[37] T. Honjo, H. Takesue, H. Kamada, Y. Nishida, O. Tadanaga, M. Asobe, and K. Inoue. Long-distance distribution of time-bin entangled photon pairs over 100 km using frequency up-conversion detectors. *Opt. Express*, 15(21):13957–13964, Oct 2007. 20

[38] I. Marcikic, H. de Riedmatten, W. Tittel, H. Zbinden, M. Legré, and N. Gisin. Distribution of time-bin entangled qubits over 50 km of optical fiber. *Phys. Rev. Lett.*, 93:180502, Oct 2004. 20

[39] Jin-Hun Kim, Jin-Woo Chae, Youn-Chang Jeong, and Yoon-Ho Kim. Long-range distribution of high-quality time-bin entangled photons for quantum communication. *Journal of the Korean Physical Society*, 80(3):203–213, February 2022. 20

[40] S. Kawanishi. Ultrahigh-speed optical time-division-multiplexed transmission technology based on optical signal processing. *IEEE Journal of Quantum Electronics*, 34(11):2064–2079, 1998. 20

[41] Takuya Ikuta and Hiroki Takesue. Implementation of quantum state tomography for time-bin qudits. *New Journal of Physics*, 19(1):013039, January 2017. Publisher: IOP Publishing. 21

[42] Jun Chen, Zachary H. Levine, Jingyun Fan, and Alan L. Migdall. Frequency-bin entangled comb of photon pairs from a silicon-on-insulator micro-resonator. *Opt. Express*, 19(2):1470–1483, Jan 2011. 21

[43] Marco Clementi, Federico Andrea Sabattoli, Massimo Borghi, Linda Gianini, Noemi Tagliavacche, Houssein El Dirani, Laurene Youssef, Nicola Bergamasco, Camille Petit-Etienne, Erwine Pargon, J. E. Sipe, Marco Liscidini, Corrado Sciancalepore, Matteo Galli, and Daniele Bajoni. Programmable frequency-bin quantum states in a nano-engineered silicon device. *Nature Communications*, 14(1):176, January 2023. 21

[44] Andrew M. Weiner. Ultrafast optical pulse shaping: A tutorial review. *Special Issue on Optical Pulse Shaping, Arbitrary Waveform Generation, and Pulse Characterization*, 284(15):3669–3692, July 2011. 21

[45] Andreas Eckstein, Benjamin Brecht, and Christine Silberhorn. A quantum pulse gate based on spectrally engineered sum frequency generation. *Opt. Express*, 19(15):13770–13778, Jul 2011. 22

[46] Vahid Ansari, John M. Donohue, Benjamin Brecht, and Christine Silberhorn. Remotely projecting states of photonic temporal modes. *Opt. Express*, 28(19):28295–28305, Sep 2020. 22

[47] A. Einstein, B. Podolsky, and N. Rosen. Can quantum-mechanical description of physical reality be considered complete? *Phys. Rev.*, 47:777–780, May 1935. 22

[48] J. S. Bell. On the einstein podolsky rosen paradox. *Physics Physique Fizika*, 1:195–200, Nov 1964. 22

[49] John F. Clauser, Michael A. Horne, Abner Shimony, and Richard A. Holt. Proposed experiment to test local hidden-variable theories. *Phys. Rev. Lett.*, 23:880–884, Oct 1969. 22

[50] Alain Aspect, Philippe Grangier, and Gérard Roger. Experimental tests of realistic local theories via bell's theorem. *Phys. Rev. Lett.*, 47:460–463, Aug 1981. 22

[51] Charles H. Bennett and Stephen J. Wiesner. Communication via one- and two-particle operators on einstein-podolsky-rosen states. *Phys. Rev. Lett.*, 69:2881–2884, Nov 1992. 22

[52] Klaus Mattle, Harald Weinfurter, Paul G. Kwiat, and Anton Zeilinger. Dense coding in experimental quantum communication. *Phys. Rev. Lett.*, 76:4656–4659, Jun 1996. 22

[53] Charles H. Bennett, Gilles Brassard, Claude Crépeau, Richard Jozsa, Asher Peres, and William K. Wootters. Teleporting an unknown quantum state via dual classical and einstein-podolsky-rosen channels. *Phys. Rev. Lett.*, 70:1895–1899, Mar 1993. 23

[54] Dik Bouwmeester, Jian-Wei Pan, Klaus Mattle, Manfred Eibl, Harald Weinfurter, and Anton Zeilinger. Experimental quantum teleportation. *Nature*, 390(6660):575–579, December 1997. 23

[55] Jan Åke Larsson. Loopholes in bell inequality tests of local realism. *Journal of Physics A: Mathematical and Theoretical*, 47(42):424003, oct 2014. 23

[56] Michael A. Nielsen and Isaac L. Chuang. *Quantum Computation and Quantum Information*. Cambridge, 2000. 23, 31

[57] Yoshiaki Tsujimoto, Motoki Tanaka, Nobuo Iwasaki, Rikizo Ikuta, Shigehito Miki, Taro Yamashita, Hirotaka Terai, Takashi Yamamoto, Masato Koashi, and Nobuyuki Imoto. High-fidelity entanglement swapping and generation of three-qubit GHZ state using asynchronous telecom photon pair sources. *Scientific Reports*, 8(1):1446, January 2018. 27

[58] Hannes Hübel, Deny R. Hamel, Alessandro Fedrizzi, Sven Ramelow, Kevin J. Resch, and Thomas Jennewein. Direct generation of photon triplets using cascaded photon-pair sources. *Nature*, 466(7306):601–603, July 2010. 27

[59] Chao-Yang Lu, Tao Yang, and Jian-Wei Pan. Experimental multiparticle entanglement swapping for quantum networking. *Phys. Rev. Lett.*, 103:020501, Jul 2009. 27

[60] Mihir Pant, Don Towsley, Dirk Englund, and Saikat Guha. Percolation thresholds for photonic quantum computing. *Nature Communications*, 10(1):1070, March 2019. 27

[61] Mercedes Gimeno-Segovia, Pete Shadbolt, Dan E. Browne, and Terry Rudolph. From three-photon greenberger-horne-zeilinger states to ballistic universal quantum computation. *Phys. Rev. Lett.*, 115:020502, Jul 2015. 27

[62] Michel Le Bellac. *Quantum Physics*. Cambridge, 2006. 27

[63] Richard Jozsa. Fidelity for mixed quantum states. *Journal of Modern Optics*, 41(12):2315–2323, 1994. 28

[64] Ryszard Horodecki, Paweł Horodecki, Michał Horodecki, and Karol Horodecki. Quantum entanglement. *Rev. Mod. Phys.*, 81:865–942, Jun 2009. 28

[65] Martin B. Plbnio and Shashank Virmani. An introduction to entanglement measures. *Quantum Info. Comput.*, 7(1):1–51, jan 2007. 29

[66] Michał Horodecki, Paweł Horodecki, and Ryszard Horodecki. Limits for entanglement measures. *Phys. Rev. Lett.*, 84:2014–2017, Feb 2000. 30

[67] Christopher J. Wood, Mohamed O. Abutaleb, Michael G. Huber, Muhammad Arif, David G. Cory, and Dmitry A. Pushin. Quantum correlations in a noisy neutron interferometer. *Phys. Rev. A*, 90:032315, Sep 2014. 30

[68] Valerie Coffman, Joydip Kundu, and William K. Wootters. Distributed entanglement. *Phys. Rev. A*, 61:052306, Apr 2000. 30

[69] Otfried Gühne and Géza Tóth. Entanglement detection. *Physics Reports*, 474(1):1–75, 2009. 30

[70] Miroslav Ježek, Jaromír Fiurášek, and Zden ěk Hradil. Quantum inference of states and processes. *Phys. Rev. A*, 68:012305, Jul 2003. 32

[71] Daniel F. V. James, Paul G. Kwiat, William J. Munro, and Andrew G. White. Measurement of qubits. *Phys. Rev. A*, 64:052312, Oct 2001. 32, 90

[72] R. G. Newton. Causality and dispersion relations (h. m. nussenzveig). *SIAM Review*, 16(4):570–571, 1974. 35

[73] David J Griffiths. *Introduction to electrodynamics*. Pearson, 2013. 35

[74] P. A. Franken, A. E. Hill, C. W. Peters, and G. Weinreich. Generation of optical harmonics. *Phys. Rev. Lett.*, 7:118–119, Aug 1961. 38

[75] A. McPherson, G. Gibson, H. Jara, U. Johann, T. S. Luk, I. A. McIntyre, K. Boyer, and C. K. Rhodes. Studies of multiphoton production of vacuum-ultraviolet radiation in the rare gases. *J. Opt. Soc. Am. B*, 4(4):595–601, Apr 1987. 41

[76] Xiyi Chen, Oleg Nadiarynkh, Sergey Plotnikov, and Paul J Campagnola. Second harmonic generation microscopy for quantitative analysis of collagen fibrillar structure. *Nature Protocols*, 7(4):654–669, April 2012. 41

[77] Florent Simon, Simon Clevers, Valérie Dupray, and Gérard Coquerel. Relevance of the second harmonic generation to characterize crystalline samples. *Chemical Engineering & Technology*, 38(6):971–983, 2015. 41

[78] Rick Trebino. *Frequency-Resolved Optical Gating: The Measurement of Ultrashort Laser Pulses*. Kluwer Academic Publishers, USA, 2000. 41, 61, 100

[79] Rick Trebino, Kenneth W. DeLong, David N. Fittinghoff, John N. Sweetser, Marco A. Krumbügel, Bruce A. Richman, and Daniel J. Kane. Measuring ultrashort laser pulses in the time-frequency domain using frequency-resolved optical gating. *Review of Scientific Instruments*, 68(9):3277–3295, 09 1997. 41

[80] S. E. Harris, M. K. Oshman, and R. L. Byer. Observation of tunable optical parametric fluorescence. *Phys. Rev. Lett.*, 18:732–734, May 1967. 45

[81] David C. Burnham and Donald L. Weinberg. Observation of simultaneity in parametric production of optical photon pairs. *Phys. Rev. Lett.*, 25:84–87, Jul 1970. 45

[82] A. Kiraz, M. Atatüre, and A. Imamoğlu. Quantum-dot single-photon sources: Prospects for applications in linear optics quantum-information processing. *Phys. Rev. A*, 69:032305, Mar 2004. 45

[83] J. McKeever, A. Boca, A. D. Boozer, R. Miller, J. R. Buck, A. Kuzmich, and H. J. Kimble. Deterministic generation of single photons from one atom trapped in a cavity. *Science*, 303(5666):1992–1994, 2004. 45

[84] A. Gruber, A. Dräbenstedt, C. Tietz, L. Fleury, J. Wrachtrup, and C. von Borczyskowski. Scanning confocal optical microscopy and magnetic resonance on single defect centers. *Science*, 276(5321):2012–2014, 1997. 45

[85] Timothy E. Keller and Morton H. Rubin. Theory of two-photon entanglement for spontaneous parametric down-conversion driven by a narrow pump pulse. *Phys. Rev. A*, 56:1534–1541, Aug 1997. 46

[86] Christophe Couteau. Spontaneous parametric down-conversion. *Contemporary Physics*, 59(3):291–304, 2018. 46

[87] K. Resch. Quantum optics course notes, 2016. 46

[88] J.-P.W. MacLean. *Ultrafast Metrology in the Quantum Domain*. PhD thesis, University of Waterloo, Waterloo, Ontario, Canada, 2019. 46, 103

[89] J.M. Donohue. *Ultrafast manipulation of single photons using dispersion and sum-frequency generation*. PhD thesis, University of Waterloo, Waterloo, Ontario, Canada, 2016. 46, 69

[90] Max Born and Emil Wolf. *Principles of Optics: Electromagnetic Theory of Propagation, Interference and Diffraction of Light (7th Edition)*. Cambridge University Press, 1999. 51

[91] J-L. Tambasco, A. Boes, L. G. Helt, M. J. Steel, and A. Mitchell. Domain engineering algorithm for practical and effective photon sources. *Opt. Express*, 24(17):19616–19626, Aug 2016. 52

[92] Francesco Graffitti, Dmytro Kundys, Derryck T Reid, Agata M Brańczyk, and Alessandro Fedrizzi. Pure down-conversion photons through sub-coherence-length domain engineering. *Quantum Science and Technology*, 2(3):035001, jul 2017. 52, 54

[93] Andreas Christ and Christine Silberhorn. Limits on the deterministic creation of pure single-photon states using parametric down-conversion. *Phys. Rev. A*, 85:023829, Feb 2012. 54

[94] Duncan England, Frédéric Bouchard, Kate Fenwick, Kent Bonsma-Fisher, Yingwen Zhang, et al. Perspectives on all-optical Kerr switching for quantum optical applications. *Applied Physics Letters*, 119(16):160501, October 2021. 59, 99

[95] G.P. Agrawal. *Nonlinear Fiber Optics, 6th Edition*. Academic Press, 2019. 59

[96] G.P. Agrawal. *Applications of Nonlinear Fiber Optics*. Elsevier Science, 2020. 59

[97] Matthew A. Hall, Joseph B. Altepeter, and Prem Kumar. Ultrafast switching of photonic entanglement. *Phys. Rev. Lett.*, 106:053901, Feb 2011. 60, 98

[98] A.M. Weiner. *Ultrafast Optics*. Wiley, 2011. 61, 69

[99] H. P. Weber. Method for Pulsewidth Measurement of Ultrashort Light Pulses Generated by Phase-Locked Lasers using Nonlinear Optics. *Journal of Applied Physics*, 38(5):2231–2234, 06 2004. 61

[100] Rick Trebino and Daniel J. Kane. Using phase retrieval to measure the intensity and phase of ultrashort pulses: frequency-resolved optical gating. *J. Opt. Soc. Am. A*, 10(5):1101–1111, May 1993. 61

[101] Jean-Philippe W. MacLean, John M. Donohue, and Kevin J. Resch. Direct characterization of ultrafast energy-time entangled photon pairs. *Phys. Rev. Lett.*, 120:053601, Jan 2018. 62, 98, 113

[102] Jean-Philippe W. MacLean, Sacha Schwarz, and Kevin J. Resch. Reconstructing ultrafast energy-time-entangled two-photon pulses. *Phys. Rev. A*, 100:033834, Sep 2019. 62, 98, 113, 126, 129

[103] W. Sellmeier. Ueber die durch die Aetherschwingungen erregten Mitschwingungen der Körpertheilchen und deren Rückwirkung auf die ersteren, besonders zur Erklärung der Dispersion und ihrer Anomalien, January 1872. 65

[104] Mikhail N. Polyanskiy. Refractive index database. https://refractiveindex.info. Accessed on 2023-06-14. 66, 108

[105] R. L. Fork, O. E. Martinez, and J. P. Gordon. Negative dispersion using pairs of prisms. *Opt. Lett.*, 9(5):150–152, May 1984. 67

[106] E. Treacy. Optical pulse compression with diffraction gratings. *IEEE Journal of Quantum Electronics*, 5(9):454–458, 1969. 67

[107] J. Lavoie, J. M. Donohue, L. G. Wright, A. Fedrizzi, and K. J. Resch. Spectral compression of single photons. *Nature Photonics*, 7(5):363–366, May 2013. 68, 112

[108] E. Treacy. Optical pulse compression with diffraction gratings. *IEEE Journal of Quantum Electronics*, 5(9):454–458, 1969. 68, 112

[109] Ian Walmsley, Leon Waxer, and Christophe Dorrer. The role of dispersion in ultrafast optics. *Review of Scientific Instruments*, 72(1):1–29, 2001. 68, 112

[110] S. Schwarz, C. Kapahi, R. Xu, A. R. Cameron, D. Sarenac, J. P. W. MacLean, K. B. Kuntz, D. G. Cory, T. Jennewein, K. J. Resch, and D. A. Pushin. Talbot effect of orbital angular momentum lattices with single photons. *Phys. Rev. A*, 101:043815, Apr 2020. 70, 88, 92

[111] H.F. Talbot Esq. F.R.S. Lxxvi. facts relating to optical science. no. iv. *The London, Edinburgh, and Dublin Philosophical Magazine and Journal of Science*, 9(56):401–407, 1836. 71, 72

[112] Jianming Wen, Yong Zhang, and Min Xiao. The talbot effect: recent advances in classical optics, nonlinear optics, and quantum optics. *Adv. Opt. Photon.*, 5(1):83–130, Mar 2013. 71

[113] Robert Iwanow, Daniel A. May-Arrioja, Demetrios N. Christodoulides, George I. Stegeman, Yoohong Min, and Wolfgang Sohler. Discrete talbot effect in waveguide arrays. *Phys. Rev. Lett.*, 95:053902, Jul 2005. 71

[114] William B. Case, Mathias Tomandl, Sarayut Deachapunya, and Markus Arndt. Realization of optical carpets in the talbot and talbot-lau configurations. *Optics Express*, 17(23):20966–20974, 2009. 71

[115] Yong Zhang, Jianming Wen, S. N. Zhu, and Min Xiao. Nonlinear talbot effect. *Phys. Rev. Lett.*, 104:183901, May 2010. 71

[116] Xin-Bing Song, Hai-Bo Wang, Jun Xiong, Kaige Wang, Xiangdong Zhang, Kai-Hong Luo, and Ling-An Wu. Experimental observation of quantum talbot effects. *Phys. Rev. Lett.*, 107:033902, Jul 2011. 71

[117] Sarayut Deachapunya, Sorakrai Srisuphaphon, Pituk Panthong, Thanarwut Photia, Kitisak Boonkham, and Surasak Chiangga. Realization of the single photon talbot effect with a spatial light modulator. *Opt. Express*, 24(18):20029–20035, Sep 2016. 71

[118] Konstantin Yu Bliokh, Ebrahim Karimi, Miles J Padgett, Miguel Angel Alonso, Mark R Dennis, Angela Dudley, Andrew Forbes, Sina Zahedpour, Scott W. Hancock, Howard M Milchberg, Stefan Rotter, Franco Nori, Sahin Kaya Ozdemir, Nicholas Bender, Hui Cao, Paul B Corkum, Carlos Hernandez Garcia, Haoran Ren, Yuri S. Kivshar, Mario G Silveirinha, Nader Engheta, A. Rauschenbeutel,

Philipp Schneeweiss, Juergen Volz, Daniel Leykam, Daria A. Smirnova, Kexiu Rong, Bo Wang, Erez Hasman, Michela Florinda Picardi, Anatoly V Zayats, Francisco J Rodriguez-Fortuño, Chenwen Yang, Jie Ren, Alexander B. Khanikaev, Andrea Alu, Etienne Brasselet, Michael Shats, Johan Verbeeck, Peter Schattschneider, Dusan Sarenac, David G Cory, Dmitry Pushin, Michael Birk, Alexey Gorlach, Ido Kaminer, Filippo Cardano, Lorenzo Marrucci, Mario Krenn, and Florian Marquardt. Roadmap on structured waves. *Journal of Optics*, 2023. 71, 129

[119] F Pfeiffer, M Bech, O Bunk, P Kraft, E F Eikenberry, Ch. Brönnimann, C Grünzweig, and C David. Hard-X-ray dark-field imaging using a grating interferometer. *Nature Materials*, 7:134, jan 2008. 71

[120] Michael S. Chapman, Christopher R. Ekstrom, Troy D. Hammond, Jörg Schmiedmayer, Bridget E. Tannian, Stefan Wehinger, and David E. Pritchard. Near-field imaging of atom diffraction gratings: The atomic talbot effect. *Phys. Rev. A*, 51:R14–R17, Jan 1995. 71

[121] L. Deng, E. W. Hagley, J. Denschlag, J. E. Simsarian, Mark Edwards, Charles W. Clark, K. Helmerson, S. L. Rolston, and W. D. Phillips. Temporal, matter-wave-dispersion talbot effect. *Phys. Rev. Lett.*, 83:5407–5411, Dec 1999. 71

[122] Saijun Wu, Edward Su, and Mara Prentiss. Demonstration of an area-enclosing guided-atom interferometer for rotation sensing. *Phys. Rev. Lett.*, 99:173201, Oct 2007. 71

[123] F. Pfeiffer, C. Grünzweig, O. Bunk, G. Frei, E. Lehmann, and C. David. Neutron phase imaging and tomography. *Phys. Rev. Lett.*, 96:215505, Jun 2006. 71

[124] D. A. Pushin, D. Sarenac, D. S. Hussey, H. Miao, M. Arif, D. G. Cory, M. G. Huber, D. L. Jacobson, J. M. LaManna, J. D. Parker, T. Shinohara, W. Ueno, and H. Wen. Far-field interference of a neutron white beam and the applications to noninvasive phase-contrast imaging. *Phys. Rev. A*, 95:043637, Apr 2017. 71

[125] D. Sarenac, D. A. Pushin, M. G. Huber, D. S. Hussey, H. Miao, M. Arif, D. G. Cory, A. D. Cronin, B. Heacock, D. L. Jacobson, J. M. LaManna, and H. Wen. Three phase-grating moiré neutron interferometer for large interferometer area applications. *Phys. Rev. Lett.*, 120:113201, Mar 2018. 71

[126] T. Gao, E. Estrecho, G. Li, O. A. Egorov, X. Ma, K. Winkler, M. Kamp, C. Schneider, S. Höfling, A. G. Truscott, and E. A. Ostrovskaya. Talbot effect for exciton polaritons. *Phys. Rev. Lett.*, 117:097403, Aug 2016. 71

[127] Vasiliy Makhalov and Andrey Turlapov. Order in the interference of a long chain of bose condensates with unrestricted phases. *Phys. Rev. Lett.*, 122:090403, Mar 2019. 71

[128] Edward T F Rogers, Jari Lindberg, Tapashree Roy, Salvatore Savo, John E Chad, Mark R Dennis, and Nikolay I Zheludev. A super-oscillatory lens optical microscope for subwavelength imaging. *Nature Materials*, 11:432, mar 2012. 71

[129] Albert Wang, Patrick Gill, and Alyosha Molnar. Light field image sensors based on the talbot effect. *Appl. Opt.*, 48(31):5897–5905, Nov 2009. 71

[130] A. Isoyan, F. Jiang, Y. C. Cheng, F. Cerrina, P. Wachulak, L. Urbanski, J. Rocca, C. Menoni, and M. Marconi. Talbot lithography: Self-imaging of complex structures. *Journal of Vacuum Science & Technology B: Microelectronics and Nanometer Structures Processing, Measurement, and Phenomena*, 27(6):2931–2937, 2009. 71

[131] Harun H. Solak, Christian Dais, and Francis Clube. Displacement talbot lithography: a new method for high-resolution patterning of large areas. *Opt. Express*, 19(11):10686–10691, May 2011. 71

[132] Yingying Liu, Xing Zhang, Youwen Huang, Jianwei Zhang, Werner Hofmann, Yongqiang Ning, and Lijun Wang. Polarization stabilized vcsels by displacement talbot lithography-defined surface gratings. *Optik*, 183:579 – 585, 2019. 71

[133] Jose Azana and Miguel A. Muriel. Temporal talbot effect in fiber gratings and its applications. *Appl. Opt.*, 38(32):6700–6704, Nov 1999. 71

[134] H. He, M. E. J. Friese, N. R. Heckenberg, and H. Rubinsztein-Dunlop. Direct observation of transfer of angular momentum to absorptive particles from a laser beam with a phase singularity. *Phys. Rev. Lett.*, 75:826–829, Jul 1995. 71, 88

[135] M. E. J. Friese, J. Enger, H. Rubinsztein-Dunlop, and N. R. Heckenberg. Optical angular-momentum transfer to trapped absorbing particles. *Phys. Rev. A*, 54:1593–1596, Aug 1996. 71

[136] Jian Wang, Jeng-Yuan Yang, Irfan M Fazal, Nisar Ahmed, Yan Yan, Hao Huang, Yongxiong Ren, Yang Yue, Samuel Dolinar, Moshe Tur, and Alan E Willner. Terabit free-space data transmission employing orbital angular momentum multiplexing. *Nature Photonics*, 6:488, jun 2012. 71

[137] Runzhou Zhang, Long Li, Zhe Zhao, Guodong Xie, Giovanni Milione, Hao Song, Peicheng Liao, Cong Liu, Haoqian Song, Kai Pang, Ari N. Willner, Brittany Lynn, Robert Bock, Moshe Tur, and Alan E. Willner. Coherent optical wireless communication link employing orbital angular momentum multiplexing in a ballistic and diffusive scattering medium. *Opt. Lett.*, 44(3):691–694, Feb 2019. 71

[138] M. F. Andersen, C. Ryu, Pierre Clade, Vasant Natarajan, A. Vaziri, K. Helmerson, and W. D. Phillips. Quantized rotation of atoms from photons with orbital angular momentum. *Phys. Rev. Lett.*, 97:170406, Oct 2006. 71, 88

[139] D. A. Pushin, D. G. Cory, C. Kapahi, M. Kulmaganbetov, M. Mungalsingh, A. E. Silva, T. Singh, B. Thompson, and D. Sarenac. Structured light enhanced entoptic stimuli for vision science applications. *Frontiers in neuroscience*, 17:1232532, 2023. 71

[140] Dusan Sarenac, Connor Kapahi, Andrew E. Silva, David G. Cory, Ivar Taminiau, Benjamin Thompson, and Dmitry A. Pushin. Direct discrimination of structured light by humans. *Proceedings of the National Academy of Sciences*, 117(26):14682–14687, 2020. 71, 88

[141] Dusan Sarenac, Andrew E Silva, Connor Kapahi, Ben Thompson, David G Cory, and Dmitry A Pushin. Human psychophysical discrimination of spatially dependant pancharatnam-berry phases in optical spin-orbit states. *arXiv preprint arXiv:2010.09619*, 2020. 71, 88

[142] Charles W Clark, Roman Barankov, Michael G Huber, Muhammad Arif, David G Cory, and Dmitry A Pushin. Controlling neutron orbital angular momentum. *Nature*, 525:504, sep 2015. 71

[143] Dusan Sarenac, Michael G. Huber, Benjamin Heacock, Muhammad Arif, Charles W. Clark, David G. Cory, Chandra B. Shahi, and Dmitry A. Pushin. Holography with a neutron interferometer. *Opt. Express*, 24(20):22528–22535, Oct 2016. 71

[144] Dusan Sarenac, Connor Kapahi, Wangchun Chen, Charles W. Clark, David G. Cory, Michael G. Huber, Ivar Taminiau, Kirill Zhernenkov, and Dmitry A. Pushin. Generation and detection of spin-orbit coupled neutron beams. *Proceedings of the National Academy of Sciences*, 2019. 71, 76

[145] Masaya Uchida and Akira Tonomura. Generation of electron beams carrying orbital angular momentum. *Nature*, 464:737, apr 2010. 71

[146] Benjamin J. McMorran, Amit Agrawal, Ian M. Anderson, Andrew A. Herzing, Henri J. Lezec, Jabez J. McClelland, and John Unguris. Electron vortex beams with high quanta of orbital angular momentum. *Science*, 331(6014):192–195, 2011. 71

[147] Johannes Courtial, Roberta Zambrini, Dennis Mark R, and Mikhail Vasnetsov. Angular momentum of optical vortex arrays. *Opt. Express*, 14(2):938–949, Jan 2006. 71

[148] Sunil Vyas and P Senthilkumaran. Interferometric optical vortex array generator. *Applied optics*, 46(15):2893–2898, 2007. 71

[149] Gong-Xiang Wei, Lei-Lei Lu, and Cheng-Shan Guo. Generation of optical vortex array based on the fractional talbot effect. *Optics Communications*, 282(14):2665 – 2669, 2009. 71

[150] Hui Gao, Yang Li, Lianwei Chen, Jinjin Jin, Mingbo Pu, Xiong Li, Ping Gao, Changtao Wang, Xiangang Luo, and Minghui Hong. Quasi-talbot effect of orbital angular momentum beams for generation of optical vortex arrays by multiplexing metasurface design. *Nanoscale*, 10:666–671, 2018. 71

[151] Jianqi Hu, Camille-Sophie Brès, and Chen-Bin Huang. Talbot effect on orbital angular momentum beams: azimuthal intensity repetition-rate multiplication. *Opt. Lett.*, 43(16):4033–4036, Aug 2018. 71

[152] Saifollah Rasouli and Davud Hebri. Theory of diffraction of vortex beams from 2d orthogonal periodicstructures and talbot self-healing under vortex beam illumination. *J. Opt. Soc. Am. A*, 36(5):800–808, May 2019. 71

[153] Julio T. Barreiro, Tzu-Chieh Wei, and Paul G. Kwiat. Remote preparation of single-photon "hybrid" entangled and vector-polarization states. *Phys. Rev. Lett.*, 105:030407, Jul 2010. 72, 89

[154] Osvaldo Jiménez Farías, Fernando de Melo, Pérola Milman, and Stephen P. Walborn. Quantum information processing by weaving quantum talbot carpets. *Phys. Rev. A*, 91:062328, Jun 2015. 72

[155] K Sawada and S P Walborn. Experimental quantum information processing with the talbot effect. *Journal of Optics*, 20(7):075201, jun 2018. 72

[156] Richard C. MacLaurin. Light. *Science*, 30(778):768–768, 1909. 73

[157] S. J. Orfanidis. *Electromagnetic Waves and Antennas*. [Online], 2016. 73

[158] Joachim Nsofini, Dusan Sarenac, Christopher J. Wood, David G. Cory, Muhammad Arif, Charles W. Clark, Michael G. Huber, and Dmitry A. Pushin. Spin-orbit states of neutron wave packets. *Phys. Rev. A*, 94:013605, Jul 2016. 75

[159] D. Sarenac, J. Nsofini, I. Hincks, M. Arif, C. W. Clark, D. G. Cory, M. G. Huber, and D. A. Pushin. Methods for preparation and detection of neutron spin-orbit states. *New Journal of Physics*, 20(10):103012, oct 2018. 77, 88

[160] Sandra W.L. Cheng. Single photon measurements: from spin-orbit lattices to ultrafast pulses. Master's thesis, University of Waterloo, Waterloo, Ontario, Canada, 2021. 81

[161] Martin J. Stevens, Scott Glancy, Sae Woo Nam, and Richard P. Mirin. Third-order antibunching from an imperfect single-photon source. *Opt. Express*, 22(3):3244–3260, Feb 2014. 82

[162] L. Vermeyden, X. Ma, J. Lavoie, M. Bonsma, U. Sinha, R. Laflamme, and K. J. Resch. Experimental test of environment-assisted invariance. *Phys. Rev. A*, 91:012120, Jan 2015. 82

[163] Joseph W Goodman. Introduction to fourier optics. *Roberts & Co. Publishers,*, 2005. 84

[164] Andrew R. Cameron, Sandra W. L. Cheng, Sacha Schwarz, Connor Kapahi, Dusan Sarenac, Michael Grabowecky, David G. Cory, Thomas Jennewein, Dmitry A. Pushin, and Kevin J. Resch. Remote state preparation of single-photon orbital-angular-momentum lattices. *Phys. Rev. A*, 104:L051701, Nov 2021. 87

[165] Dusan Sarenac, Connor Kapahi, Wangchun Chen, Charles W. Clark, David G. Cory, Michael G. Huber, Ivar Taminiau, Kirill Zhernenkov, and Dmitry A. Pushin. Generation and detection of spin-orbit coupled neutron beams. *Proceedings of the National Academy of Sciences*, 116(41):20328–20332, 2019. 88

[166] Ebrahim Karimi, Lorenzo Marrucci, Vincenzo Grillo, and Enrico Santamato. Spin-to-orbital angular momentum conversion and spin-polarization filtering in electron beams. *Phys. Rev. Lett.*, 108:044801, Jan 2012. 88

[167] Halina Rubinsztein-Dunlop, Andrew Forbes, M V Berry, M R Dennis, David L Andrews, Masud Mansuripur, Cornelia Denz, Christina Alpmann, Peter Banzer,

Thomas Bauer, Ebrahim Karimi, Lorenzo Marrucci, Miles Padgett, Monika Ritsch-Marte, Natalia M Litchinitser, Nicholas P Bigelow, C Rosales-Guzmán, A Belmonte, J P Torres, Tyler W Neely, Mark Baker, Reuven Gordon, Alexander B Stilgoe, Jacquiline Romero, Andrew G White, Robert Fickler, Alan E Willner, Guodong Xie, Benjamin McMorran, and Andrew M Weiner. Roadmap on structured light. *Journal of Optics*, 19(1):013001, nov 2016. 88

[168] Masaya Uchida and Akira Tonomura. Generation of electron beams carrying orbital angular momentum. *Nature*, 464(7289):737–739, April 2010. 88

[169] Denis A. Ikonnikov, Sergey A. Myslivets, Mikhail N. Volochaev, Vasily G. Arkhipkin, and Andrey M. Vyunishev. Two-dimensional Talbot effect of the optical vortices and their spatial evolution. *Scientific Reports*, 10(1):20315, November 2020. 88

[170] Xinzhong Li, Haixiang Ma, Hao Zhang, Yuping Tai, Hehe Li, Miaomiao Tang, Jingge Wang, Jie Tang, and Yangjian Cai. Close-packed optical vortex lattices with controllable structures. *Opt. Express*, 26(18):22965–22975, Sep 2018. 88

[171] Yu-Jing Han, Zhen-Yu Rong, Li Zhang, and Xiao-Yi Chen. Generation of propagation-invariant vector beams with square array by use of 2d binary phase mask and pentagonal prism. *Appl. Opt.*, 58(23):6325–6328, Aug 2019. 88

[172] C.T. Schmiegelow and F. Schmidt-Kaler. Light with orbital angular momentum interacting with trapped ions. *The European Physical Journal D*, 66(6):157, Jun 2012. 88

[173] Xi-Wang Luo, Xingxiang Zhou, Jin-Shi Xu, Chuan-Feng Li, Guang-Can Guo, Chuanwei Zhang, and Zheng-Wei Zhou. Synthetic-lattice enabled all-optical devices based on orbital angular momentum of light. *Nature Communications*, 8(1):16097, July 2017. 88

[174] N. V. Morrow, S. K. Dutta, and G. Raithel. Feedback control of atomic motion in an optical lattice. *Phys. Rev. Lett.*, 88:093003, Feb 2002. 88

[175] Andrew Forbes and Isaac Nape. Quantum mechanics with patterns of light: Progress in high dimensional and multidimensional entanglement with structured light. *AVS Quantum Science*, 1(1):011701, 2019. 88

[176] Julio T Barreiro, Tzu-Chieh Wei, and Paul G Kwiat. Beating the channel capacity limit for linear photonic superdense coding. *Nature Physics*, 4(4):282–286, 2008. 88

[177] Lorenzo Marrucci, Ebrahim Karimi, Sergei Slussarenko, Bruno Piccirillo, Enrico Santamato, Eleonora Nagali, and Fabio Sciarrino. Spin-to-orbital conversion of the angular momentum of light and its classical and quantum applications. *Journal of Optics*, 13(6):064001, jun 2011. 88

[178] Giovanni Milione, Martin P. J. Lavery, Hao Huang, Yongxiong Ren, Guodong Xie, Thien An Nguyen, Ebrahim Karimi, Lorenzo Marrucci, Daniel A. Nolan, Robert R. Alfano, and Alan E. Willner. 4 × 20 gbit/s mode division multiplexing over free space using vector modes and a q-plate mode (de)multiplexer. *Opt. Lett.*, 40(9):1980–1983, May 2015. 88

[179] Giuseppe Vallone, Vincenzo D'Ambrosio, Anna Sponselli, Sergei Slussarenko, Lorenzo Marrucci, Fabio Sciarrino, and Paolo Villoresi. Free-space quantum key distribution by rotation-invariant twisted photons. *Phys. Rev. Lett.*, 113:060503, Aug 2014. 88

[180] Christian T Schmiegelow, Jonas Schulz, Henning Kaufmann, Thomas Ruster, Ulrich G Poschinger, and Ferdinand Schmidt-Kaler. Transfer of optical orbital angular momentum to a bound electron. *Nature Communications*, 7(1):12998, 2016. 88

[181] Robert Fickler, Geoff Campbell, Ben Buchler, Ping Koy Lam, and Anton Zeilinger. Quantum entanglement of angular momentum states with quantum numbers up to 10,010. *Proceedings of the National Academy of Sciences*, 113(48):13642–13647, 2016. 88

[182] Alicia Sit, Frédéric Bouchard, Robert Fickler, Jérémie Gagnon-Bischoff, Hugo Larocque, Khabat Heshami, Dominique Elser, Christian Peuntinger, Kevin Günthner, Bettina Heim, Christoph Marquardt, Gerd Leuchs, Robert W. Boyd, and Ebrahim Karimi. High-dimensional intracity quantum cryptography with structured photons. *Optica*, 4(9):1006–1010, Sep 2017. 88

[183] Eleonora Nagali, Fabio Sciarrino, Francesco De Martini, Lorenzo Marrucci, Bruno Piccirillo, Ebrahim Karimi, and Enrico Santamato. Quantum information transfer from spin to orbital angular momentum of photons. *Phys. Rev. Lett.*, 103:013601, Jun 2009. 89

[184] Chuan Wang, Yong Zhang, and Ru Zhang. Entanglement purification based on hybrid entangled state using quantum-dot and microcavity coupled system. *Opt. Express*, 19(25):25685–25695, Dec 2011. 89

[185] Eleni Diamanti, Hoi-Kwong Lo, Bing Qi, and Zhiliang Yuan. Practical challenges in quantum key distribution. *npj Quantum Information*, 2(1):16025, November 2016. 89

[186] Mhlambululi Mafu, Angela Dudley, Sandeep Goyal, Daniel Giovannini, Melanie McLaren, Miles J. Padgett, Thomas Konrad, Francesco Petruccione, Norbert Lütkenhaus, and Andrew Forbes. Higher-dimensional orbital-angular-momentum-based quantum key distribution with mutually unbiased bases. *Phys. Rev. A*, 88:032305, Sep 2013. 89

[187] Jino Heo, Min-Sung Kang, Chang-Ho Hong, Hyung-Jin Yang, Seong-Gon Choi, and Jong-Phil Hong. Distribution of hybrid entanglement and hyperentanglement with time-bin for secure quantum channel under noise via weak cross-Kerr nonlinearity. *Scientific Reports*, 7(1):10208, 2017. 89

[188] Seyed Mohammad Hashemi Rafsanjani, Mohammad Mirhosseini, Omar S. Magaña Loaiza, and Robert W. Boyd. State transfer based on classical nonseparability. *Phys. Rev. A*, 92:023827, Aug 2015. 89

[189] Manuel Erhard, Hammam Qassim, Harjaspreet Mand, Ebrahim Karimi, and Robert W. Boyd. Real-time imaging of spin-to-orbital angular momentum hybrid remote state preparation. *Phys. Rev. A*, 92:022321, Aug 2015. 89

[190] Robert Fickler, Radek Lapkiewicz, Sven Ramelow, and Anton Zeilinger. Quantum entanglement of complex photon polarization patterns in vector beams. *Phys. Rev. A*, 89:060301(R), Jun 2014. 89

[191] Isaac Nape, Nikiwe Mashaba, Nokwazi Mphuthi, Sruthy Jayakumar, Shanti Bhattacharya, and Andrew Forbes. Vector-mode decay in atmospheric turbulence: An analysis inspired by quantum mechanics. *Phys. Rev. Applied*, 15:034030, Mar 2021. 89

[192] Yiyu Zhou, Jiapeng Zhao, Boris Braverman, Kai Pang, Runzhou Zhang, Alan E. Willner, Zhimin Shi, and Robert W. Boyd. Multiprobe time reversal for high-fidelity vortex-mode-division multiplexing over a turbulent free-space link. *Phys. Rev. Applied*, 15:034011, Mar 2021. 89

[193] Ilaria Gianani, Alessia Suprano, Taira Giordani, Nicolò Spagnolo, Fabio Sciarrino, Dimitris Gorpas, Vasilis Ntziachristos, Katja Pinker, Netanel Biton, Judy Kupferman, and Shlomi Arnon. Transmission of vector vortex beams in dispersive media. *Advanced Photonics*, 2(3):1 – 8, 2020. 89

[194] Arun K. Pati. Minimum classical bit for remote preparation and measurement of a qubit. *Phys. Rev. A*, 63:014302, Dec 2000. 89

[195] Charles H. Bennett, David P. DiVincenzo, Peter W. Shor, John A. Smolin, Barbara M. Terhal, and William K. Wootters. Remote state preparation. *Phys. Rev. Lett.*, 87:077902, Jul 2001. 89, 90

[196] Hoi-Kwong Lo. Classical-communication cost in distributed quantum-information processing: A generalization of quantum-communication complexity. *Phys. Rev. A*, 62:012313, Jun 2000. 89

[197] Debbie W. Leung and Peter W. Shor. Oblivious remote state preparation. *Phys. Rev. Lett.*, 90:127905, Mar 2003. 89

[198] Borivoje Dakić, Yannick Ole Lipp, Xiaosong Ma, Martin Ringbauer, Sebastian Kropatschek, Stefanie Barz, Tomasz Paterek, Vlatko Vedral, Anton Zeilinger, Časlav Brukner, and Philip Walther. Quantum discord as resource for remote state preparation. *Nature Physics*, 8(9):666–670, 2012. 89

[199] Nicholas A. Peters, Julio T. Barreiro, Michael E. Goggin, Tzu-Chieh Wei, and Paul G. Kwiat. Remote state preparation: Arbitrary remote control of photon polarization. *Phys. Rev. Lett.*, 94:150502, Apr 2005. 89

[200] Ryszard Horodecki, Paweł Horodecki, Michał Horodecki, and Karol Horodecki. Quantum entanglement. *Rev. Mod. Phys.*, 81:865–942, Jun 2009. 94

[201] Valerie Coffman, Joydip Kundu, and William K. Wootters. Distributed entanglement. *Phys. Rev. A*, 61:052306, Apr 2000. 95

[202] Andrew R. Cameron, Kate L. Fenwick, Sandra W. L. Cheng, Sacha Schwarz, Benjamin MacLellan, Philip J. Bustard, Duncan England, Benjamin Sussman, and Kevin J. Resch. Ultrafast measurement of energy-time entanglement with an optical kerr shutter, 2023. 97

[203] Raju Valivarthi, Samantha I. Davis, Cristián Peña, Si Xie, Nikolai Lauk, Lautaro Narváez, Jason P. Allmaras, Andrew D. Beyer, Yewon Gim, Meraj Hussein, George Iskander, Hyunseong Linus Kim, Boris Korzh, Andrew Mueller, Mandy Rominsky, Matthew Shaw, Dawn Tang, Emma E. Wollman, Christoph Simon, Panagiotis Spentzouris, Daniel Oblak, Neil Sinclair, and Maria Spiropulu. Teleportation systems toward a quantum internet. *PRX Quantum*, 1:020317, Dec 2020. 98

[204] Ramy Tannous, Wilson Wu, Stéphane Vinet, Chithrabhanu Perumangatt, Dogan Sinar, Alexander Ling, and Thomas Jennewein, 2023. 98

[205] Lars S. Madsen, Fabian Laudenbach, Mohsen Falamarzi Askarani, Fabien Rortais, Trevor Vincent, Jacob F. F. Bulmer, Filippo M. Miatto, Leonhard Neuhaus, Lukas G. Helt, Matthew J. Collins, Adriana E. Lita, Thomas Gerrits, Sae Woo Nam, Varun D. Vaidya, Matteo Menotti, Ish Dhand, Zachary Vernon, Nicolás Quesada, and Jonathan Lavoie. Quantum computational advantage with a programmable photonic processor. *Nature*, 606(7912):75–81, June 2022. 98

[206] Yingwen Zhang, Duncan England, Andrei Nomerotski, Peter Svihra, Steven Ferrante, Paul Hockett, and Benjamin Sussman. Multidimensional quantum-enhanced target detection via spectrotemporal-correlation measurements. *Phys. Rev. A*, 101:053808, May 2020. 98

[207] A. Cuevas, G. Carvacho, G. Saavedra, J. Cariñe, W.A.T. Nogueira, M. Figueroa, A. Cabello, P. Mataloni, G. Lima, and G.B. Xavier. Long-distance distribution of genuine energy-time entanglement. *Nat Commun*, 4:2871, 2013. 98

[208] Matthew R. Brown, Markus Allgaier, Valérian Thiel, John Monnier, Michael G. Raymer, and Brian J. Smith. Interferometric imaging using shared quantum entanglement, 2022. 98

[209] Fabian Steinlechner, Sebastian Ecker, Matthias Fink, Bo Liu, Jessica Bavaresco, Marcus Huber, Thomas Scheidl, and Rupert Ursin. Distribution of high-dimensional entanglement via an intra-city free-space link. *Nat Commun*, 8:15971, 2017. 98

[210] Boris Korzh, Qing-Yuan Zhao, Jason P. Allmaras, Simone Frasca, Travis M. Autry, Eric A. Bersin, Andrew D. Beyer, Ryan M. Briggs, Bruce Bumble, Marco Colangelo, Garrison M. Crouch, Andrew E. Dane, Thomas Gerrits, Adriana E. Lita, Francesco Marsili, Galan Moody, Cristián Peña, Edward Ramirez, Jake D. Rezac, Neil Sinclair, Martin J. Stevens, Angel E. Velasco, Varun B. Verma, Emma E. Wollman, Si Xie, Di Zhu, Paul D. Hale, Maria Spiropulu, Kevin L. Silverman, Richard P. Mirin, Sae Woo Nam, Alexander G. Kozorezov, Matthew D. Shaw, and Karl K. Berggren. Demonstration of sub-3 ps temporal resolution with a superconducting nanowire single-photon detector. *Nature Photonics*, 14(4):250–255, April 2020. 98

[211] Gregor G. Taylor, Ewan N. MacKenzie, Boris Korzh, Dmitry V. Morozov, Bruce Bumble, Andrew D. Beyer, Jason P. Allmaras, Matthew D. Shaw, and Robert H

Hadfield. Mid-infrared timing jitter of superconducting nanowire single-photon detectors. *Applied Physics Letters*, 121(21):214001, 2022. 98

[212] Kazuo Hogari and Takao Matsumoto. Electrostatically driven micromechanical 2 × 2 optical switch. *Appl. Opt.*, 30(10):1253–1257, Apr 1991. 98

[213] Caleb Knoernschild, Changsoon Kim, Felix P. Lu, and Jungsang Kim. Multiplexed broadband beam steering system utilizing high speed mems mirrors. *Opt. Express*, 17(9):7233–7244, Apr 2009. 98

[214] Pavel Kolchin, Chinmay Belthangady, Shengwang Du, G. Y. Yin, and S. E. Harris. Electro-optic modulation of single photons. *Phys. Rev. Lett.*, 101:103601, Sep 2008. 98

[215] Vilson R. Almeida, Carlos A. Barrios, Roberto R. Panepucci, Michal Lipson, Mark A. Foster, Dimitre G. Ouzounov, and Alexander L. Gaeta. All-optical switching on a silicon chip. *Opt. Lett.*, 29(24):2867–2869, Dec 2004. 98

[216] Markus Allgaier, Gesche Vigh, Vahid Ansari, Christof Eigner, Viktor Quiring, Raimund Ricken, Benjamin Brecht, and Christine Silberhorn. Fast time-domain measurements on telecom single photons. *Quantum Science and Technology*, 2(3):034012, July 2017. 98

[217] Onur Kuzucu, Franco N. C. Wong, Sunao Kurimura, and Sergey Tovstonog. Joint temporal density measurements for two-photon state characterization. *Phys. Rev. Lett.*, 101:153602, Oct 2008. 98

[218] NA Whitaker, Hercules Avramopoulos, PMW French, M Christina Gabriel, David J LaMarche, Di Giovanni, and Herman M Presby. All-optical arbitrary demultiplexing at 2.5 gbits/s with tolerance to timing jitter. *Optics letters*, 16(23):1838–1840, 1991. 99

[219] Eiichi Yamada, Kazunori Suzuki, and Masataka Nakazawa. Subpicosecond optical demultiplexing at 10 ghz with a zero-dispersion, dispersion-flattened, nonlinear fiber-loop mirror controlled by a 500-fs gain-switched ld. In *Optical Fiber Communication Conference*, page ThL5. Optica Publishing Group, 1995. 99

[220] L Moller, Yikai Su, Xiang Liu, Juerg Leuthold, and Chongjin Xie. Ultrahigh-speed optical phase correlated data signals. *IEEE Photonics Technology Letters*, 15(11):1597–1599, 2003. 99

[221] Connor Kupchak, Philip J Bustard, Khabat Heshami, Jennifer Erskine, Michael Spanner, Duncan G England, and Benjamin J Sussman. Time-bin-to-polarization conversion of ultrafast photonic qubits. *Physical Review A*, 96(5):053812, 2017. 99

[222] Connor Kupchak, Jennifer Erskine, Duncan England, and Benjamin Sussman. Terahertz-bandwidth switching of heralded single photons. *Opt. Lett.*, 44(6):1427–1430, Mar 2019. 99, 112

[223] Frédéric Bouchard, Duncan England, Philip J Bustard, Kate L Fenwick, Ebrahim Karimi, Khabat Heshami, and Benjamin Sussman. Achieving ultimate noise tolerance in quantum communication. *Physical Review Applied*, 15(2):024027, 2021. 99

[224] Frédéric Bouchard, Duncan England, Philip J Bustard, Khabat Heshami, and Benjamin Sussman. Quantum communication with ultrafast time-bin qubits. *PRX Quantum*, 3(1):010332, 2022. 99

[225] Frédéric Bouchard, Kent Bonsma-Fisher, Khabat Heshami, Philip J Bustard, Duncan England, and Benjamin Sussman. Measuring ultrafast time-bin qudits. *Physical Review A*, 107(2):022618, 2023. 99

[226] Kate L Fenwick, Duncan G England, Philip J Bustard, James M Fraser, and Benjamin J Sussman. Carving out configurable ultrafast pulses from a continuous wave source via the optical kerr effect. *Optics Express*, 28(17):24845–24853, 2020. 99

[227] Masahiro Yabuno, Takahiro Takumi, Fumihiro China, Shigehito Miki, Hirotaka Terai, Peter J. Mosley, Rui-Bo Jin, and Ryosuke Shimizu. Ultrafast measurement of a single-photon wave packet using an optical kerr gate. *Opt. Express*, 30(4):4999–5007, Feb 2022. 99, 126

[228] Bahaa E A Saleh and Malvin Carl Teich. *Fundamentals of photonics; 1st ed.* Wiley and Sons, New York, NY, 1991. 102, 118

[229] Lu-Ming Duan, G. Giedke, J. I. Cirac, and P. Zoller. Inseparability criterion for continuous variable systems. *Phys. Rev. Lett.*, 84:2722–2725, Mar 2000. 103, 107

[230] L. K. Shalm, D. R. Hamel, Z. Yan, C. Simon, K. J. Resch, and T. Jennewein. Three-photon energy–time entanglement. *Nature Physics*, 9(1):19–22, January 2013. 106, 107

[231] Nicolas Fabre, Arne Keller, and Pérola Milman. Time and frequency as quantum continuous variables. *Phys. Rev. A*, 105:052429, May 2022. 107

[232] Peter van Loock and Akira Furusawa. Detecting genuine multipartite continuous-variable entanglement. *Phys. Rev. A*, 67:052315, May 2003. 107

[233] J. D. Franson. Nonlocal cancellation of dispersion. *Phys. Rev. A*, 45:3126–3132, Mar 1992. 112, 120

[234] Youn Seok Lee, Mengyu Xie, Ramy Tannous, and Thomas Jennewein. Sagnac-type entangled photon source using only conventional polarization optics. *Quantum Science and Technology*, 6(2):025004, jan 2021. 121

[235] Amin Babaei-Ghazvini, Benjamin Cudmore, Matthew J. Dunlop, Bishnu Acharya, Rabin Bissessur, Marya Ahmed, and William M. Whelan. Effect of magnetic field alignment of cellulose nanocrystals in starch nanocomposites: Physicochemical and mechanical properties. *Carbohydrate Polymers*, 247:116688, 2020. 121

[236] J. M. Donohue, M. Mastrovich, and K. J. Resch. Spectrally engineering photonic entanglement with a time lens. *Phys. Rev. Lett.*, 117:243602, Dec 2016. 126

[237] Frédéric Bouchard, Alicia Sit, Felix Hufnagel, Aazad Abbas, Yingwen Zhang, Khabat Heshami, Robert Fickler, Christoph Marquardt, Gerd Leuchs, Robert w. Boyd, and Ebrahim Karimi. Quantum cryptography with twisted photons through an outdoor underwater channel. *Opt. Express*, 26(17):22563–22573, Aug 2018. 128

[238] Ling Ji, Jun Gao, Ai-Lin Yang, Zhen Feng, Xiao-Feng Lin, Zhong-Gen Li, and Xian-Min Jin. Towards quantum communications in free-space seawater. *Opt. Express*, 25(17):19795–19806, Aug 2017. 128

[239] Nehad Hirmiz, Anthony Tsikouras, Elizabeth J. Osterlund, Morgan Richards, David W. Andrews, and Qiyin Fang. Cross-talk reduction in a multiplexed synchroscan streak camera with simultaneous calibration. *Opt. Express*, 27(16):22602–22614, Aug 2019. 129

[240] Sören Wengerowsky, Siddarth Koduru Joshi, Fabian Steinlechner, Hannes Hübel, and Rupert Ursin. An entanglement-based wavelength-multiplexed quantum communication network. *Nature*, 564(7735):225–228, December 2018.

[241] Mercedes Gimeno-Segovia, Pete Shadbolt, Dan E. Browne, and Terry Rudolph. From three-photon greenberger-horne-zeilinger states to ballistic universal quantum computation. *Phys. Rev. Lett.*, 115:020502, Jul 2015.

[242] Yiqi Zhang, Milivoj R. Belić, Milan S. Petrović, Huaibin Zheng, Haixia Chen, Changbiao Li, Keqing Lu, and Yanpeng Zhang. Two-dimensional linear and nonlinear talbot effect from rogue waves. *Phys. Rev. E*, 91:032916, Mar 2015.

[243] Lord Rayleigh. Xxv. on copying diffraction-gratings, and on some phenomena connected therewith. *The London, Edinburgh, and Dublin Philosophical Magazine and Journal of Science*, 11(67):196–205, 1881.

[244] Mariana R. Barros, Andreas Ketterer, Osvaldo Jiménez Farías, and Stephen P. Walborn. Free-space entangled quantum carpets. *Phys. Rev. A*, 95:042311, Apr 2017.

[245] Mario Krenn, Johannes Handsteiner, Matthias Fink, Robert Fickler, Rupert Ursin, Mehul Malik, and Anton Zeilinger. Twisted light transmission over 143 km. *Proceedings of the National Academy of Sciences*, 113(48):13648–13653, 2016.

[246] S Tsesses, E Ostrovsky, K Cohen, B Gjonaj, NH Lindner, and G Bartal. Optical skyrmion lattice in evanescent electromagnetic fields. *Science*, 361(6406):993–996, 2018.

[247] Tomer Stav, Arkady Faerman, Elhanan Maguid, Dikla Oren, Vladimir Kleiner, Erez Hasman, and Mordechai Segev. Quantum entanglement of the spin and orbital angular momentum of photons using metamaterials. *Science*, 361(6407):1101–1104, 2018.

[248] VAJM Sleiffer, Yongmin Jung, Vladimir Veljanovski, RGH Van Uden, Maxim Kuschnerov, H Chen, B Inan, L Grüner Nielsen, Y Sun, David J Richardson, et al. 73.7 tb/s (96 x 3 x 256-gb/s) mode-division-multiplexed dp-16qam transmission with inline mm-edfa. *Optics Express*, 20(26):B428–B438, 2012.

[249] C Paterson. Atmospheric Turbulence and Orbital Angular Momentum of Single Photons for Optical Communication. *Phys. Rev. Lett.*, 2005.

[250] I. Afek, A. Natan, O. Ambar, and Y. Silberberg. Quantum state measurements using multipixel photon detectors. *Phys. Rev. A*, 79:043830, Apr 2009.

[251] David Dussault and Paul Hoess. Noise performance comparison of ICCD with CCD and EMCCD cameras. In C. Bruce Johnson, Eustace L. Dereniak, and Robert E. Sampson, editors, *Infrared Systems and Photoelectronic Technology*, volume 5563, pages 195 – 204. International Society for Optics and Photonics, SPIE, 2004.

[252] John M. Dudley, Goëry Genty, and Stéphane Coen. Supercontinuum generation in photonic crystal fiber. *Rev. Mod. Phys.*, 78:1135–1184, Oct 2006.

[253] Govind Agrawal. Chapter 2 - pulse propagation in fibers. In Govind Agrawal, editor, *Nonlinear Fiber Optics (Fifth Edition)*, Optics and Photonics, pages 27–56. Academic Press, Boston, fifth edition edition, 2013.

[254] Andreas Vetter, Simone Ferrari, Patrik Rath, Rasoul Alaee, Oliver Kahl, Vadim Kovalyuk, Silvia Diewald, Gregory N. Goltsman, Alexander Korneev, Carsten Rockstuhl, and Wolfram H. P. Pernice. Cavity-Enhanced and Ultrafast Superconducting Single-Photon Detectors. *Nano Letters*, 16(11):7085–7092, November 2016. Publisher: American Chemical Society.

[255] Michael J. Grabowecky, Christopher A. J. Pollack, Andrew R. Cameron, Robert W. Spekkens, and Kevin J. Resch. Experimentally bounding deviations from quantum theory for a photonic three-level system using theory-agnostic tomography. *Phys. Rev. A*, 105:032204, Mar 2022.